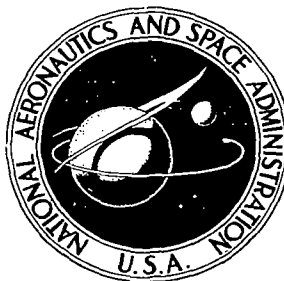


**NASA CONTRACTOR  
REPORT**

NASA CR-1963



NASA CR-19

2.1

0061311

TECH LIBRARY KAFB, NM

**LOAN COPY: RETURN TO  
AFWL (DO/L)  
KIRTLAND AFB, N. M.**

**A NUMERICAL METHOD FOR COMPUTING  
THREE-DIMENSIONAL VISCOUS  
SUPERSONIC FLOW FIELDS  
ABOUT SLENDER BODIES**

*by Leonard Walitt and John G. Trulio*

*Prepared by*  
**APPLIED THEORY, INC.**  
Los Angeles, Calif. 90024  
*for Ames Research Center*

**NATIONAL AERONAUTICS AND SPACE ADMINISTRATION • WASHINGTON, D. C. • NOVEMBER 1971**



0061311

1. Report No. NASA CR-1963		2. Government Accession No.		3. Recipient's Catalog No.	
4. Title and Subtitle  A Numerical Method for Computing Three-Dimensional Viscous Supersonic Flow Fields About Slender Bodies				5. Report Date November 1971	
				6. Performing Organization Code	
7. Author(s)  Leonard Walitt and John G. Trulio				8. Performing Organization Report No.	
9. Performing Organization Name and Address  Applied Theory, Inc. 1010 Westwood Blvd. Los Angeles, California 90024				10. Work Unit No.	
				11. Contract or Grant No.  NAS 2-4998	
12. Sponsoring Agency Name and Address  National Aeronautics & Space Administration Washington, D.C. 20546				13. Type of Report and Period Covered Contractor Report	
				14. Sponsoring Agency Code	
15. Supplementary Notes					
16. Abstract  A numerical method is presented for the calculation of steady, three-dimensional, viscous, compressible flow fields about slender bodies at angle of attack and at supersonic speeds. Approximations are introduced in modeling the flow in the longitudinal direction. Accordingly, the flow fields calculated with the program were computed with a model that permits viscous crossflow together with inviscid axial flow. An analysis of the errors introduced by such a treatment is presented. Numerical calculations were made and compared with experimental results for an ogive-cylinder and an airplane fuselage configuration. Generally, good agreement with experiment was obtained. However, boundary layer separation and body vortex positions differed from experimental locations on the ogive-cylinder, and the shock induced by the fuselage canopy was predicted at a slightly different location.					
17. Key Words (Suggested by Author(s))  Aircraft flow fields, Numerical method, Navier-stokes equations, Three-dimensional flow fields, Viscous flow fields				18. Distribution Statement  UNCLASSIFIED-UNLIMITED	
19. Security Classif. (of this report)  UNCLASSIFIED		20. Security Classif. (of this page)  UNCLASSIFIED		21. No. of Pages  103	
				22. Price*  \$3.00	

## SUMMARY

A numerical method has been used to calculate steady, three-dimensional, viscous compressible flow fields about slender bodies at angle of attack. The method is based on the equivalence principle, and on a procedure developed earlier for solving the equations of two-dimensional transient continuum motion (applied here to the Navier-Stokes equations). The numerical technique, and the basic features of the equivalence principle as applied to case of present concern, are both reviewed herein, and the results of calculations of two slender body flow fields are presented.

The equivalence principle relates the axial coordinate of a steady three-dimensional flow field to the time coordinate of two-dimensional transient flow; thus, a given three-dimensional problem becomes directly analogous to a two-dimensional problem of flow about a cylinder (not necessarily circular) that deforms with time. It is basic to the validity of the equivalence principle that axial velocities do not differ significantly at any point from the axial component of the free stream velocity, a requirement that precludes the use of a no-slip condition at the body surface in the axial direction. Accordingly, the flow fields considered in the program, including separation and body vortex development, were computed with a model that permits viscous crossflow together with inviscid axial flow. An analysis of the errors introduced by such a treatment is presented herein.

Numerical calculations were made and compared with experimental results for an ogive-cylinder and an airplane fuselage configuration. Flow conditions were  $M_\infty = 1.98$ ,  $R_\infty = 4.68 \times 10^6/\text{ft}$ , and  $\alpha = 10^\circ$  for the ogive-cylinder, and  $M_\infty = 2.50$ ,  $R_\infty = 9.1 \times 10^6/\text{ft}$ , and  $\alpha = 15^\circ$  for the fuselage configuration. Results are presented as static pressure distributions on the body surface, as velocity vector plots, and as contour maps of the flow field at selected axial locations. Good agreement between theory and experiment was obtained; maximum deviations of numerical

surface pressures from corresponding experimental values were no more than 6 percent of free stream dynamic pressure for both problems. However, some differences were noted. Boundary-layer separation and body vortex positions differed from experimental locations on the ogive-cylinder, and the shock induced by the fuselage canopy was predicted at a slightly different location. These differences are considered attributable to neglect of axial viscous effects, exclusion of turbulence phenomena, and the approximations introduced by the equivalence principle in describing inviscid axial flow.

## TABLE OF CONTENTS

Summary	ii
1.0 INTRODUCTION	1
2.0 SYMBOLS	2
3.0 THE NUMERICAL METHOD	6
3.1 FORMULATION OF EQUIVALENCE	6
3.2 DESCRIPTION OF THE NUMERICAL METHOD	9
3.3 ORDER OF ERROR OF THE NUMERICAL METHOD	16
3.3.1 Equivalence Principle Errors	17
3.3.2 Discretization Errors	21
4.0 CALCULATIONS MADE AND RESULTS OBTAINED	23
4.1 DESCRIPTION OF PROBLEMS SOLVED	23
4.2 MESHES USED	24
4.3 BOUNDARY CONDITIONS AND INITIAL CONDITIONS	26
4.4 RESULTS OF OGIVE-CYLINDER PROBLEM	27
4.4.1 Qualitative Behavior of Numerical Flow Field	27
4.4.2 Surface Pressure Comparisons	28
4.4.3 The Flow Field About the Ogive-Cylinder	28
4.4.4 Accuracy of the Ogive-Cylinder Calculations	29
4.4.5 Drag and Lift Coefficients	30
4.5 RESULTS OF FUSELAGE PROBLEM	31
4.5.1 Qualitative Behavior of Numerical Flow Field	32
4.5.2 Surface Pressure Comparison	32
4.5.3 Accuracy of the Fuselage Calculations	33
4.5.4 Contour Maps in the Flow Field of the Fuselage	34
4.5.5 Lift and Drag Coefficients	37
5.0 CONCLUSIONS AND RECOMMENDATIONS	38

## TABLE OF CONTENTS

APPENDIX A:	THE EQUIVALENCE PRINCIPLE	41
APPENDIX B:	CONSERVATION OF TOTAL ENERGY	46
APPENDIX C:	AFTON 2PE FINITE DIFFERENCE EQUATIONS AT INTERIOR MESH POINTS	49
APPENDIX D:	PARAMETRIC REPRESENTATION OF FUSELAGE CROSS SECTIONS	55
APPENDIX E:	DATA REDUCTION COMPUTER CODE	60
REFERENCES		63

Figures

### ACKNOWLEDGEMENTS

The authors are pleased to acknowledge the contributions of Dr. D. S. Srinivasa of Applied Theory, Inc. and Messrs. L. S. King and E. W. Perkins of the Aerodynamics Branch of the AMES Research Center's Aeronautics Division to the work reported herein. Dr. Srinivasa helped develop the finite difference meshes which were used in the numerical calculations; Messrs. King and Perkins provided many helpful suggestions and discussions in the course of this work.

## 1.0 INTRODUCTION

For highly maneuverable advanced aircraft (cf. figure 1), the prediction of flow-field characteristics for nonsimple geometries at high angles of attack and high flight Mach numbers transcends the capabilities of linear theories. For example, there is a need for an analytical or numerical method that provides an accurate, detailed description of the vehicle flow field in order to determine both fuselage configurations and inlet-airframe integration effects.

Prediction of the three-dimensional flow field about a slender body immersed in a supersonic airstream presents a formidable mathematical problem to which no exact solution has been obtained, either analytically or numerically. Successful numerical methods using the method of characteristics and the equivalence principle have been developed for three-dimensional, steady, inviscid flow fields. The work of Gallo and Rakich (ref. 1) is representative of the characteristics approach, while Van Dyke's extension (ref. 2) of the theory introduced by Hayes (ref. 3) is representative of an approach that uses the equivalence principle.

In this research program the equivalence principle was used to convert time-dependent viscous, compressible flow calculations in two space dimensions to steady motion of a viscous, compressible fluid in three space dimensions. The two-dimensional flow calculations were obtained by numerically solving the time-dependent compressible Navier-Stokes equations.



## 2.0 SYMBOLS

$a$	Lagrangian coordinate
$a$	Radius
$A$	Surface area
$A_1$	Abscissa of center of smaller circle of fuselage cross section
$A_5$	Abscissa of center of canopy circle
$B_1$	Ordinate of center of smaller circle of fuselage cross section
$B_2(z')$	Ordinate of axis of the body with respect to the horizontal reference line
$B'_2(z')$	Slope of axis of the body with respect to horizontal reference line
$B_5$	Ordinate of center of canopy circle
$B(x,y,z)$	Surface of the body
$C$	Local sound speed
$C_D$	Drag coefficient, $\frac{\text{drag force}}{q_\infty A_c}$
$C_L$	Lift coefficient, $\frac{\text{lift force}}{q_\infty A_c}$
$C_P$	Pressure coefficient, $\frac{P - P_\infty}{q_\infty}$
$c_p$	Specific heat at constant pressure
$c_v$	Specific heat at constant volume
$d$	Diameter
$\underline{d}$	Displacement vector

$E$	Specific internal energy
$f_2$	Bounded oscillating function used to determine discretization error
$H$	Stagnation enthalpy
$l_x, l_y, l_z$	Direction cosines of the normal to the body's surface in the x,y, and z directions, respectively
$m$	Mass
$M$	Mach number
$\underline{M}$	Momentum vector
$ \Delta M $	Absolute error in Mach number
$n_x, n_y, n_z$	Direction cosines of the normal to a shock surface in the x, y and z directions, respectively
$N$	Cycle number
$N$	Mesh point density
$P$	Pressure
$P_s$	Stagnation pressure
$ \Delta P $	Absolute error in pressure
$P_p$	Pitot pressure
$q$	Dynamic pressure, $q = (1/2)\rho U^2$
$R$	Reynolds number
$R_1$	Radius of smaller circle of fuselage cross section
$R_2$	Radius of larger arc of fuselage cross section
$R_3$	Radius of canopy circle
$\underline{R}(j,k)$	Position vector of the mesh point about a fuselage cross section
$\underline{R}'(j,k)$	Position vector of a mesh point about a circular cross section

S	Entropy
$S(x,y,t)$	Surface describing system of shock waves about a body
t	Time
$\Delta t$	Time step
T	Temperature
u	Velocity component in x direction
U	One-dimensional velocity, $U(a,t)$
$\underline{U}$	Velocity vector
v	Velocity component in the y direction
v	Specific volume
V	Volume
w	Velocity component in the z direction
W	Work rate
x	Coordinate normal to plane consisting of the $7\frac{1}{2}^\circ$ reference line and the perpendicular to that line
$x'$	Coordinate normal to the plane consisting of the horizontal reference line and the perpendicular to that line
X	Lagrangian coordinate, $X = X(a,t)$
y	Coordinate normal to $7\frac{1}{2}^\circ$ reference line
$y'$	Coordinate normal to the horizontal reference line
z	Coordinate along the $7\frac{1}{2}^\circ$ reference line
$z'$	Coordinate along the horizontal reference line
$\alpha$	Free-stream angle of attack with respect to body axis

$\alpha_e$	Local angle of attack with respect to a horizontal reference line, $\tan^{-1} \left( \frac{\text{velocity in } y' \text{ direction}}{\text{velocity in } z' \text{ direction}} \right)$
$\beta$	Sideslip angle, $\tan^{-1} \left( \frac{\text{velocity in } x' \text{ direction}}{\text{velocity in } z' \text{ direction}} \right)$
$\gamma$	Ratio of specific heats, $\frac{c_p}{c_v}$
$\epsilon$	Discretization error in a property (eq. (29))
$\rho$	Density
$\tau$	Maximum slope of surface of body with respect to the free-stream flow direction
$( )_s$	Stagnation condition
$( )_s$	Property downstream of a shock
$( )_\infty$	Free-stream condition
$( )_0$	Lagrangian coordinate at time zero
$(\bar{\phantom{x}})$	Reduced variable
$( )_a$	Actual variable
$( )_c$	Variable associated with body cross section

### 3.0 THE NUMERICAL METHOD

#### 3.1 FORMULATION OF EQUIVALENCE PRINCIPLE

The two-dimensional time-dependent equations of motion (independent variables  $x, y, t$ ) can be transformed directly to steady-state three-dimensional ( $x, y, z$ ) equations for slender bodies through the Hayes equivalence principle. The equivalence principle relates the steady-state flow field over a slender body to an equivalent time-dependent flow field in one less space dimension. In particular, steady three-dimensional flow about a body can be reduced under certain conditions to two-dimensional time-dependent flow in a plane normal to the free-stream flow direction.

A simple example of the application of the equivalence principle is illustrated in figure 2, namely that of steady flow over an axisymmetric body at zero angle of attack. The steady-state two-dimensional axially symmetric flow field is analogous to time-dependent one-dimensional axially symmetric flow in a plane caused by an expanding cylinder. The cross-section plane of unsteady analogy moves downstream with free-stream velocity and the outline of the moving boundary is given by the trace of the original shape in the cross-section plane. At the station  $z$  (see fig. 2), the steady-state flow field in the cross-section plane is analogous to the flow field about the expanding cylinder at the time,  $t = z/U_\infty$ . To make the equivalence analogy valid, the normal velocity of the expanding cross section  $U_n$ , is given by the product of the free-stream velocity and the tangent to the surface. Far from the body, free-stream conditions are imposed (i.e.,  $P = P_\infty$ ,  $\rho = \rho_\infty$ ,  $u = v = 0$ ).

According to convention, the free-stream flow direction is chosen as the principal axis along which the linearization approximations for equivalence are made. However, for bodies at angle of attack as illustrated in figure 3, it is more convenient to choose the body axis as the principal axis. In planes normal to the body axis, the cross sections can usually be defined in terms of a few simple analytic expressions,

which result in simple and accurate surface boundary conditions, and facilitate the development of finite difference meshes about these cross sections. Because of this choice, free-stream crossflow will exist as an upstream boundary condition, but the choice of axis in no way affects the accuracy of the results. This point is further discussed in Section 3.3.

It is convenient to discuss the equivalence principle in terms of flow about a slender body of revolution at angle of attack,  $\alpha$ . Let the  $z$  axis coincide with the axis of the body, and let the cross section of the body lie in the  $x,y$  plane (see fig. 3). It is also assumed that the  $z$  component of the local velocity vector is approximately equal to the  $z$  component of the free-stream velocity vector, that is,

$$w = U_{\infty} \cos \alpha \quad (1)$$

Under this hypothesis, it follows that time-dependent flow in the  $x,y$  plane transforms to time-independent motion in  $x,y,z$  space according to the equations

$$z = U_{\infty} \cos \alpha t \quad (2)$$

$$y = y \quad (3)$$

$$x = x \quad (4)$$

This result — the equivalence principle — is derived for an inviscid fluid in Appendix A.

In order for equations (2), (3), and (4) to represent a valid mapping between a flow field in  $x,y,t$  space and a flow field in  $x,y,z$  space, the time-dependent solution in the  $x,y$  plane must be augmented by a three-dimensional boundary condition at the body surface

$$\ell_z U_{\infty} \cos \alpha + \ell_y v + \ell_x u = 0 \quad (5)$$

where  $\ell_x$ ,  $\ell_y$ ,  $\ell_z$  are the direction cosines of the normal to the body surface in the x,y, and z directions, respectively. Equation (5) states that at the body, the component of the local velocity normal to the body surface is zero. The application of the boundary condition (equation (5)), in the x,y plane implies that the body cross section varies in time and that the velocity normal to the surface is equal to  $-\ell_z U_\infty \cos \alpha / \sqrt{\ell_y^2 + \ell_x^2}$  a normal velocity expression that reduces to the product of the axial velocity ( $U_\infty \cos \alpha$ ) and the local tangent to the surface.

A second boundary condition, a constraint on tangential flow at the body surface, must also be specified. Since the full time-dependent Navier-Stokes equations are solved in the x,y plane, a no-slip boundary condition is imposed at the cross section of the body. We require that

$$v \ell_x - u \ell_y = 0 \quad (6)$$

It is seen in Appendix A that the boundary equations (equations (5) and (6)) are compatible with the assumptions inherent in the equivalence principle and permit a time-dependent viscous calculation to be made in the x,y plane. Thus, with the inclusion of boundary equations (5) and (6), a solution of the two-dimensional time-dependent Navier-Stokes equations is also the solution to a problem of steady three-dimensional viscous flow.

The three-dimensional boundary layer on the body surface has been replaced by a two-dimensional boundary layer since the no-slip condition is imposed at the body surface only in the crossflow direction. This ad hoc description of the flow field is poor in the boundary layer. However, its justification lies in the fact that it provides a mechanism for effecting flow separation and the subsequent development of spiral vortex sheets on the lee side of a body at angle of attack. To be sure, solving the compressible Navier-Stokes equations in a crossflow plane is much more realistic than the conventional approach of solving the Laplace equation in this plane with experimentally (or otherwise) determined

circulation strengths. However, the accuracy of the viscous crossflow description must be carefully documented by comparing the numerical results with other calculations and with experimental data.

The computational procedure is then as follows. Initially we have a uniform flow field in the  $x,y$  plane with a velocity in the  $y$  direction equal in magnitude to  $U_{\infty} \sin \alpha$ . The slender-body cross section grows with time in the  $x,y$  plane. At discrete times solutions of the full time-dependent Navier-Stokes equations are obtained such that the cross-section surface boundary conditions (equations (5) and (6)) are satisfied; also, the flow far from the cross section is uniform with a crossflow velocity in the  $y$  direction equal to  $U_{\infty} \sin \alpha$ . The time-dependent solution in the  $x,y$  plane is then related to the steady three-dimensional flow field about the body through the transformation equations (2), (3), and (4).

### 3.2 DESCRIPTION OF THE NUMERICAL METHOD

The numerical method used to solve the time-dependent Navier-Stokes equations in two space dimensions is embodied in a computer code called "AFTON 2PE". The finite difference equations in the AFTON 2PE computer code are based on a physical model of the continuum. The need for such a model as a basis for numerical calculations of continuum motion has long been recognized (refs. 4,5 and 6), and was filled after considerable effort for continuum motion in all its generality, the model for two-dimensional flow actually preceded the general case, and is recalled in some detail below. The two-dimensional continuum model is not specific to the particular phenomenon under study here, nor even to the entire class of motions governed by the Navier-Stokes equations; once a physical model of the continuum is verified, its range of application extends to many flow situations.

In the conventional use of physical models, it is assumed that the partial differential form of the Navier-Stokes equations applies in general. A physical model is then postulated for the particular phenomenon to be studied and the Navier-Stokes equations are reduced to ordinary differential equations from which we obtain either an analytical or numerical



solution. The Lees-Reeves (ref. 7) near-wake model is a good example of a conventional physical model. This model is concerned with the base flow and near-wake subregions shown in figure 4. The model recognizes a constant pressure shear-layer near the body separation point and a viscous inviscid flow interaction near the wake-stagnation point. The boundary layer equations are assumed to govern the flow in both regions. The flow fields in both regions are solved separately and then joined together through the pressure gradient in the streamwise direction.

For illustrative purposes, the space-time continuum model employed in this research is presented in detail for the case of time-dependent one-dimensional flow of a compressible, inviscid fluid. This model was implied by a set of finite difference equations developed by von Neumann and Richtmyer (refs. 8 and 9). A careful analysis of the von Neumann-Richtmyer equations led to the continuum model employed here (refs. 4,5 and 10).

Finite difference analogs of the continuity equation, momentum equation, and the First Law of Thermodynamics will be derived in a Lagrangian coordinate system. Let  $a$  be the Lagrangian coordinate, and  $X(a,t)$  be the Eulerian coordinate. That is,  $X(a,t)$  gives the position at time  $t$ , of a fluid element that was originally at position  $a$ . Consider the Lagrangian coordinates,  $a_1$ ,  $a_2$ , and  $a_{\frac{1}{2}}$  [ $a_{\frac{1}{2}} = \frac{1}{2} (a_1 + a_2)$ ] shown in figure 5. Since the system is Lagrangian, the mass between the trajectories labeled  $a_1$  and  $a_2$  remains a constant. Let the one-dimensional space continuum be represented by a discrete set of zones, designated "thermodynamic" zones. At time zero, let the boundaries of these zones be spaced at a constant interval  $\Delta a$  along the  $X$  axis [see fig. 5] and denoted by  $a_\ell$  ( $\ell=0,1,2,3,\dots,L$ ). Let each of the thermodynamic zones be one unit high and one unit wide. Consider another set of zones designated "momentum" zones superimposed on the thermodynamic zones, such that each momentum zone surface always divides the mass of the thermodynamic zone which contains this surface in half. A schematic diagram showing a momentum zone and two thermodynamic zones at the time  $t$  is shown in figure 5. The

Eulerian coordinates which define the two thermodynamic zones are  $X(a_{\ell-1}, t)$ ,  $X(a_{\ell}, t)$ , and  $X(a_{\ell+1}, t)$ , while the Eulerian coordinates of the momentum zone are  $X(a_{\ell-\frac{1}{2}}, t)$  and  $X(a_{\ell+\frac{1}{2}}, t)$ .

The thermodynamic variables, such as internal energy, specific volume, and pressure, are assumed constant throughout a thermodynamic zone. The velocity is assumed constant throughout a momentum zone. Thus, thermodynamic variables are in effect centered at the momentum zone surfaces; that is,  $P_{\ell} = P(a_{\ell-\frac{1}{2}}, t)$  denotes the pressure in the thermodynamic zone  $X(a_{\ell-1}, t)$ ,  $X(a_{\ell}, t)$  which effectively acts at  $X(a_{\ell-\frac{1}{2}}, t)$  [see fig. 5]. Momentum zone variables are in effect centered at the thermodynamic zone surfaces; that is,  $U_{\ell} = U(a_{\ell}, t)$  denotes the particle velocity in the momentum zone  $X(a_{\ell-\frac{1}{2}}, t)$ ,  $X(a_{\ell+\frac{1}{2}}, t)$  which effectively acts at  $X(a_{\ell}, t)$ .

Since an explicit formulation is the goal, the variables of motion are not only displaced spatially (as discussed above), but they are displaced in time as well. Let  $\Delta t$  denote the uniform time interval and  $t^n (n=0, 1, 2, \dots, N)$  denote the time after  $n$  uniform time intervals. The variables associated with thermodynamic zones are defined at integer times; that is,  $P_{\ell-\frac{1}{2}}^n = P(a_{\ell-\frac{1}{2}}, t^n)$  denotes the pressure at the time  $t^n$ . The momentum zone variables are defined at half-integer times; that is,  $U_{\ell}^{n-\frac{1}{2}} = U(a_{\ell}, t^{n-\frac{1}{2}})$  denotes the particle velocity at a time  $t^{n-\frac{1}{2}}$ , and the Eulerian coordinate position  $X(a_{\ell}, t^{n-\frac{1}{2}})$ .

Finite difference analogs of the continuity, momentum, and first law equations follow directly from the physical model of the continuum presented in figure 5. Since a Lagrangian coordinate system is employed, the zones of figure 5 will be displaced continuously from their initial positions; that is,  $a_1, \dots, a_L$  to coordinate positions  $X(a_1, t), \dots, X(a_L, t)$ . Let us calculate the properties at the time,  $t^n$ , for the thermodynamic zone having Lagrangian coordinates  $a_{\ell-1}, a_{\ell}$  and the momentum zone having Lagrangian coordinates  $a_{\ell-\frac{1}{2}}, a_{\ell+\frac{1}{2}}$ . The initial values for this calculation are

$$P_{\ell-\frac{1}{2}}^{n-1}, E_{\ell-\frac{1}{2}}^{n-1}, v_{\ell-\frac{1}{2}}^{n-1}, P_{\ell+\frac{1}{2}}^{n-1}, E_{\ell+\frac{1}{2}}^{n-1}, v_{\ell+\frac{1}{2}}^{n-1}$$

for the thermodynamic zones and

$$X_{l-1}^n, X_l^n, X_{l+1}^n, U_{l-1}^{n-\frac{1}{2}}, U_l^{n-\frac{1}{2}}, U_{l+1}^{n-\frac{1}{2}}$$

for the momentum zones. The objective is to update these variables by one time step in an explicit manner.

The finite difference analog to the conservation of mass is derived from the expression for the volume change of thermodynamic zone  $a_{l-1}, a_l$ .

$$V_{l-\frac{1}{2}}^n - V_{l-\frac{1}{2}}^{n-1} = \left( U_l^{n-\frac{1}{2}} - U_{l-1}^{n-\frac{1}{2}} \right) \Delta t \quad (7)$$

where

$V_{l-\frac{1}{2}}^{n-1}$  volume of zone  $a_{l-1}, a_l$  at time  $t^{n-1}$

$V_{l-\frac{1}{2}}^n$  volume of zone  $a_{l-1}, a_l$  at time  $t^n$

Based on equation (7), and the fact that the mass of material in the thermodynamic zone  $a_{l-1}, a_l$  has the constant value  $\rho_0 \Delta a$ , we find that

$$\rho_0 \left( \frac{V_{l-\frac{1}{2}}^n - V_{l-\frac{1}{2}}^{n-1}}{\Delta t} \right) = \frac{U_l^{n-\frac{1}{2}} - U_{l-1}^{n-\frac{1}{2}}}{\Delta a} \quad (8)$$

where  $\rho_0$  is the density at time zero, and  $V_{l-\frac{1}{2}}^n$  is the specific volume of material in the zone at time  $t^n$  (note that  $(\rho_0 \Delta a) V_{l-\frac{1}{2}}^n = V_{l-\frac{1}{2}}^n$ ).

For an inviscid, adiabatic fluid, the first law equation for a system in equilibrium is applicable:

$$\frac{DE}{Dt} = -P \frac{Dv}{Dt} \quad (9a)$$

The First Law finite difference analog to equation (9a) is derived by first writing down a finite difference analog to the term  $-P(Dv/Dt)$  and then equating this to the rate of change of internal energy in the zone. Since the zone mass is constant and the pressure is homogeneous in a thermodynamic zone, the term  $-P(Dv/Dt)$  becomes

$$\left( - P \frac{\Delta v}{\Delta t} \right)_{l-\frac{1}{2}} = \frac{-\frac{1}{2}(P_{l-\frac{1}{2}}^n + P_{l-\frac{1}{2}}^{n-1})(U_{l-\frac{1}{2}}^{n-\frac{1}{2}} - U_{l-1}^{n-\frac{1}{2}})}{m_{l-\frac{1}{2}}} \quad (9b)$$

where

$$m_{l-\frac{1}{2}} = \rho_0 \Delta a$$

On the basis of equation (9b), the finite difference First Law equation becomes

$$\frac{\rho_0 (E_{l-\frac{1}{2}}^n - E_{l-\frac{1}{2}}^{n-1})}{\Delta t} = \frac{-\frac{1}{2}(P_{l-\frac{1}{2}}^n + P_{l-\frac{1}{2}}^{n-1})(U_{l-\frac{1}{2}}^{n-\frac{1}{2}} - U_{l-1}^{n-\frac{1}{2}})}{\Delta a} \quad (10)$$

where  $E_{l-\frac{1}{2}}^{n-1}$  is the specific internal energy of thermodynamic zone  $a_{l-1}, a_l$ .

The equation of state for a perfect gas is:

$$E = \frac{Pv}{\gamma-1} \quad (11)$$

Finally, the finite difference equation of motion for momentum zone  $a_{l-\frac{1}{2}}, a_{l+\frac{1}{2}}$  becomes:

$$\frac{M_{l-\frac{1}{2}}^n - M_{l-\frac{1}{2}}^{n-1}}{\Delta t} = \left( P_{l-\frac{1}{2}}^{n-\frac{1}{2}} - P_{l+\frac{1}{2}}^{n-\frac{1}{2}} \right) \quad (12)$$

where

$$P_{l-\frac{1}{2}}^{n-\frac{1}{2}} = \frac{1}{2}(P_{l-\frac{1}{2}}^n + P_{l-\frac{1}{2}}^{n-1})$$

$$P_{l+\frac{1}{2}}^{n-\frac{1}{2}} = \frac{1}{2}(P_{l+\frac{1}{2}}^n + P_{l+\frac{1}{2}}^{n-1})$$

and  $M_l^n$  defines the momentum in zone  $a_l$  at time  $t^n$ .

Equations (8), (10), and (12), derived from the physical model presented in figure 5 are solved in the following manner. First, the specific volume,  $v_{l-\frac{1}{2}}^n$ , is calculated from equation (8). Then, the

pressure  $P_{\ell-\frac{1}{2}}^n$ , and specific internal energy  $E_{\ell-\frac{1}{2}}^n$  are calculated from equations (10) and (11). The continuity and first law equations are then solved for specific volume and pressure in all thermodynamic zones. Based on the pressure field, equation (12) can be solved for the momentum  $M_{\ell}^n$ . The particle velocity  $U_{\ell}^{n+\frac{1}{2}}$  is found from the forward extrapolation formula

$$U_{\ell}^{n+\frac{1}{2}} = 2 \frac{M_{\ell}^n}{m_{\ell}} - U_{\ell}^{n-\frac{1}{2}} \quad (13)$$

where

$$m_{\ell} = \rho_0 \Delta a$$

Integration of the particle velocity  $U_{\ell}^{n+\frac{1}{2}}$  with time establishes the new Eulerian position,  $X_{\ell}^{n+1}$ . This can be done for all momentum zones. Thus, all the initial values cited above can be updated by one time step and the process repeated.

The success of this method coupled with the failure of other more recent numerical schemes to improve upon it, led Trulio and Trigger to a careful analysis of these finite difference equations in order to discover the reasons for their success. They found that the finite difference equations possessed the same self-consistency property of form as the original differential equations from which they were derived, that is, the finite difference equations for momentum conservation and the first law implied an exact conservation of total energy (internal and kinetic) finite difference equation (ref. 4). In other words, the continuity, momentum, first law, and conservation of total energy relations are redundant by one. In most other numerical schemes if one tries to derive a conservation of total energy relation from finite difference analog of momentum conservation and the first law, error terms, usually assumed to be "second order", are produced. These numerical error terms are believed to be a primary source of the difficulties encountered in many other

numerical schemes. Appendix B demonstrates the self-consistency property of the finite difference equations (8) to (13).

In addition to self-consistency of form, the numerical method has the following properties:

- (a) Since the method is explicit, stability criteria must be met in order to obtain physically meaningful numerical results. In general, the time step must be small enough so that a sound signal cannot cross a zone in a time step (refs. 8 and 9).
- (b) The numerical error has been correlated for this scheme. It has been found that the absolute error in a property is inversely proportional to the linear mesh point density to the three-halves power (ref. 10).

The physical model, from which equations (8) to (13) have been derived has been extended to two space dimensions (ref.11). In that work, specific finite difference equations were formulated and their self-consistency properties demonstrated. Because they provide a base for the present calculation, a brief description of the derivation of these equations will be presented.

Consider two-dimensional flow of a viscous, compressible fluid in the x,y plane. As in the one-dimensional case, let us divide the continuum into two types of zones; namely, quadrilateral zones and momentum zones (see figure 6). The assumptions governing this analysis are as follows:

- (a) All zones are polygons.
- (b) The density, specific internal energy, pressure, stress tensor, and velocity derivatives are homogeneous in a quadrilateral zone.
- (c) The velocity vector is homogeneous in a momentum zone.
- (d) The zones have unit thickness normal to the plane of motion.

As in the one-dimensional case the continuity and first law equations are solved for each quadrilateral zone to determine the density, specific internal energy, and stress. When the stress tensor depends only on strain, the first law equation corresponds to that of thermodynamics. However, for a stress-rate of strain dependence, the first law equation is a relationship involving internal energy<sup>\*</sup> which results from subtraction of the kinetic energy equation from the conservation of total energy equation. Based on the stress tensors in each of the four quadrilateral zones which comprise a momentum zone (see fig. 6), the momentum equation is solved for each momentum zone. To accommodate the equivalence principle boundary conditions, the finite difference equations in AFTON 2PE are written in a generalized coordinate system where the four mesh points comprising a quadrilateral zone can move with arbitrary velocity. The numerical method is described in detail for a generalized coordinate system and an Eulerian coordinate system in two places (refs. 11 and 12).

All of the salient properties of the numerical method described in the one-dimensional example are preserved in two-dimensions and will also be preserved in three spatial dimensions; in that respect the numerical theory is internally consistent. The momentum and first law finite difference equations in two dimensions imply an exact finite difference equation for total energy. The stability criteria are the same as in the one-dimensional case. The one-dimensional correlation of absolute numerical error in a property extends directly to two dimensions. In two dimensions the absolute numerical error is inversely proportional to the area mesh point density to the three-quarters power (ref. 12). The AFTON 2PE finite difference equations at interior mesh points are presented in Appendix C.

### 3.3 ORDER OF ERROR OF THE NUMERICAL METHOD

In this section the order of error of the numerical method is determined. The numerical error is defined as the absolute difference between the actual value of a quantity and the value computed numerically

---

\*The specific internal energy is the difference between total and kinetic energy.

The error in this method stems from three sources, the equivalence principle, discretization errors, and neglect of axial viscous effects and turbulence phenomena. The errors inherent in the equivalence principle lie in the neglect of the velocity perturbation along the free-stream flow direction and have been deduced by Van Dyke (ref. 2). The discretization error is defined as the difference between the exact solution to the continuum motion equivalence principle equations for a given system, and the values of the flow variables computed from a finite difference approximation to these equations of motion; discretization error results basically from the substitution of a discrete set of points for the space-time continuum. The errors introduced by neglecting axial viscous effects and turbulence phenomena manifest themselves in the accuracy with which separation point locations and vortex center trajectories can be predicted. Since the determination of the accuracy of the method is of primary importance, all three sources of error will be discussed at some length.

### 3.3.1 Equivalence Principle Errors

To deduce the order of error in the neglect of the velocity perturbation along the free stream flow direction, Van Dyke introduced what he termed "reduced" independent and dependent variables, and he redefined the functions describing the body and shock-wave surfaces. To obtain these reduced variables, consider a coordinate system where the  $z$  axis is aligned with free-stream flow direction. Let the surface of the body be described by  $B(x,y,z) = 0$ , and let the complete system of shock waves be described by  $S(x,y,z) = 0$ . In this coordinate system the reduced variables are as follows:

$$\left. \begin{aligned} \bar{x} &= x/\tau \\ \bar{y} &= y/\tau \\ \bar{z} &= z \end{aligned} \right\} \quad (14)$$



$$\left. \begin{aligned} u &= U_{\infty} \tau \bar{u}(\bar{x}, \bar{y}, \bar{z}) \\ v &= U_{\infty} \tau \bar{v}(\bar{x}, \bar{y}, \bar{z}) \\ w &= U_{\infty} [1 + \tau^2 \bar{w}(\bar{x}, \bar{y}, \bar{z})] \end{aligned} \right\} \quad (15)$$

$$P = P_{\infty} \gamma M_{\infty}^2 \tau^2 \bar{P}(\bar{x}, \bar{y}, \bar{z}) \quad (16)$$

$$\rho = \rho_{\infty} \bar{\rho}(\bar{x}, \bar{y}, \bar{z}) \quad (17)$$

$$\left. \begin{aligned} B &= \bar{B}(\bar{x}, \bar{y}, \bar{z}) \\ S &= \bar{S}(\bar{x}, \bar{y}, \bar{z}) \end{aligned} \right\} \quad (18)$$

where  $\tau$  is the maximum slope of the body surface with respect to the free-stream flow direction. This transformation of variables was introduced into the continuity, momentum, and first law equations for an inviscid fluid. Reduced parameters were considered of order one or less and terms that contained  $\tau^2$  explicitly were discarded. A set of reduced equations, linear in  $\bar{w}$  and derivatives with respect to  $\bar{z}$ , resulted.

If the reduced equations are rewritten in terms of the actual unbarred parameters, and the substitution  $z = U_{\infty} t$  is made, the time-dependent equations of motion in two space dimensions result.

The boundary conditions for the reduced equations are as follows:  
At the body surface

$$\bar{u} \frac{\partial \bar{B}}{\partial \bar{x}} + \bar{v} \frac{\partial \bar{B}}{\partial \bar{y}} + \frac{\partial \bar{B}}{\partial \bar{z}} = 0 \quad \text{at } \bar{B} = 0 \quad (19)$$

Far upstream of the body

$$\left. \begin{aligned} P &\rightarrow \frac{1}{\gamma M_{\infty}^2 \tau^2} \\ \bar{\rho} &\rightarrow 1 \end{aligned} \right\} \quad \text{as } \bar{z} \rightarrow -\infty \quad (20)$$

The parameters  $M_{\infty}$  and  $\tau$  of the full problem enter the reduced problem only in the combination  $M_{\infty} \tau$ , which appears only in the upstream

boundary condition on  $\bar{P}$  (eq. 20). Since  $\bar{P}$  must be of order one or less for these equations to be valid,  $M_\infty \tau$ , must be of order one or greater for this theory to be consistent far upstream of the body. If this consistency condition is satisfied, the maximum error in a reduced variable must be of the order  $\tau^2$ , because terms of order  $\tau^2$  have been omitted in the reduction. Since  $M_\infty \tau$  is of order unity, an error of order  $\tau^2$  implies an error of order  $1/(M_\infty^2)$ . Hence, the theory becomes more accurate as the free stream Mach number goes up. Since supersonic flow problems are solved in this paper, this source of error, although small, will not be negligible. Based on the  $\tau^2$  error law, the maximum errors in the static pressures and local Mach numbers are derived below.

The absolute difference between the actual reduced pressure,  $\bar{P}_a$ , and the reduced pressure calculated from this theory,  $\bar{P}$ , is

$$|\bar{P}_a - \bar{P}| \approx \tau^2 \quad (21)$$

Combining equations (16) and (21) yields

$$|\bar{P}_a - \bar{P}| \approx \frac{|P_a - P|}{2q_\infty \tau^2} \approx \tau^2$$

where  $q_\infty$  is the free-stream dynamic pressure  $[(\frac{1}{2})\rho_\infty U_\infty^2]$ . Therefore, the absolute error in the pressure is as follows:

$$|P_a - P| \approx 2q_\infty \tau^4 \quad (22)$$

Since experimental and numerical local Mach numbers are compared in this research effort, it is important to determine the order of error in the Mach number. The Mach number,  $M$ , is defined as

$$M = \frac{(u^2 + v^2 + w^2)^{\frac{1}{2}}}{c} \quad (23)$$

where  $C$  is the local sound speed. From Bernoulli's equation, the local sound speed can be expressed in terms of the components of local velocity

$$C^2 = C_\infty^2 - \frac{\gamma - 1}{2} [u^2 + v^2 + w^2 - U_\infty^2] \quad (24)$$

where  $C_\infty$  is the free-stream sound speed. Introducing the reduced velocities  $\bar{u}$ ,  $\bar{v}$ , and  $\bar{w}$  from equations (15) into equations (23) and (24) yields the relation for the Mach number in terms of reduced velocities.

$$M = \frac{(1 + \tau^4 \bar{w}^2 + 2\tau^2 \bar{w} + \tau^2 \bar{v}^2 + \tau^2 \bar{u}^2)^{\frac{1}{2}}}{\left[ M_\infty^{-2} - \left( \frac{\gamma - 1}{2} \right) \tau^2 (\bar{w}^2 \tau^2 + 2\bar{w} + \bar{v}^2 + \bar{u}^2) \right]^{\frac{1}{2}}} \quad (25)$$

Since  $\bar{u}$ ,  $\bar{v}$ , and  $\bar{w}$  are of order one, terms in  $\tau^4$  could be neglected in equation (25).

$$M \approx \left[ \frac{1 + \tau^2 (2\bar{w} + \bar{v}^2 + \bar{u}^2)}{M_\infty^{-2} - \left( \frac{\gamma - 1}{2} \right) \tau^2 (2\bar{w} + \bar{v}^2 + \bar{u}^2)} \right]^{\frac{1}{2}} \quad (26)$$

Equation (26) can be linearized in terms of changes in  $\bar{u}$ ,  $\bar{v}$ , and  $\bar{w}$  by employing a first-order Taylor's expansion. Let  $M_a$  represent the actual local Mach number and  $M$  represent the value computed by this numerical method. From a first-order Taylor's expansion

$$M_a \approx M + \left( \frac{\partial M}{\partial \bar{u}} \right)_{\bar{u}, \bar{v}, \bar{w}} \Delta \bar{u} + \left( \frac{\partial M}{\partial \bar{v}} \right)_{\bar{u}, \bar{v}, \bar{w}} \Delta \bar{v} + \left( \frac{\partial M}{\partial \bar{w}} \right)_{\bar{u}, \bar{v}, \bar{w}} \Delta \bar{w} \quad (27)$$

The coefficients of equation (27) can be determined by differentiation of equation (26) and evaluation of the derivatives at the values  $\bar{u} = \bar{v} = 1$ ,  $\bar{w} = 0$ , since barred planar quantities are assumed of order one, and the perturbation velocity  $\bar{w}$  is assumed to be near zero. The final equation is as follows:

$$\frac{|\Delta M|}{M_\infty} \approx \frac{3\tau^4 \left( 1 + \frac{\gamma - 1}{2} M_\infty^2 \right)}{\left[ 1 - (\gamma - 1) \tau^2 M_\infty^2 \right]^{\frac{3}{2}} (1 + 2\tau^2)^{\frac{1}{2}}} \quad (28)$$

where

$$|\Delta M| = |M_a - M|$$

### 3.3.2 Discretization Errors

The discretization error in the two-dimensional time-dependent equations of Section 3.3.1 is based on a general rule that relates the error to the density of mesh points employed in the numerical integration process. The derivation of this error rule can be found in references 10 and 12; the relation is as follows:

$$\epsilon = f_2 N^{-3/4} \quad (29)$$

where  $\epsilon$  is the absolute discretization error in a given property,  $N$  is the two-dimensional mesh point density (i.e., number of zones per unit area of the  $x,y$  plane), and  $f_2$  is a bounded oscillatory function. If the same problem is run with two different meshes, that is, a medium and fine mesh; the function  $f_2$  can be evaluated from the values of a property and mesh point densities of the medium and fine meshes at the same point in space and time. For the case where the static pressure error is required,

$$f_2 = \frac{|P_f - P_m|}{|N_f^{-3/4} - N_m^{-3/4}|} \quad (30)$$

where  $P_f$  is the fine mesh pressure,  $P_m$  is the medium mesh pressure,  $N_m$  is the mesh point density of the medium mesh, and  $N_f$  is the mesh point density for the fine mesh.

### 3.3.3 Errors Due to Neglect of Axial Viscous Effects and Turbulence

The error introduced by neglecting axial viscous effects and turbulence phenomena is the most difficult of the three sources of error to evaluate. Therefore, no formal attempt was made to evaluate this error

on analytical and/or numerical grounds. The numerical results for the problems solved in this paper were compared to experimental data. Deviations in separation point locations and vortex center trajectories were noted, and on the basis of physical arguments, the primary causes of the deviations were explained.

In this research effort the effects of mesh point density on the discretization error were not investigated; each problem of the program was run with only one mesh. Therefore, the order of error of the numerical method, which was established by comparing the numerical results with experimental ones, included all three sources of errors.

#### 4.0 CALCULATIONS MADE AND RESULTS OBTAINED

##### 4.1 DESCRIPTION OF PROBLEMS SOLVED

The AFTON-2PE computer code, modified to accommodate the equivalence principle boundary conditions, was applied first to the flow field about an ogive-cylinder configuration and second, to a fuselage geometry representative of an advanced tactical fighter plane. In both problems, air, represented as a gamma law gas ( $\gamma = 1.4$ ), was considered and adiabatic flow was assumed throughout the flow field. For the ogive-cylinder problem the free-stream Mach number was 1.98, the angle of attack was  $10^\circ$  with respect to the axis of the body, and the free-stream Reynolds number was  $4.68 \times 10^6/\text{ft}$ . For the fuselage problem the free-stream Mach number was 2.5, the angle of attack was  $15^\circ$  with respect to the horizontal, and the free-stream Reynolds number was  $9.1 \times 10^6/\text{ft}$ . In this section the cross-sectional shapes for both problems are defined and in the next section the finite difference meshes generated about these cross sections are described.

The axisymmetric ogive-cylinder configuration is composed of an ogive which is three maximum cylinder diameters long and a cylinder 7.3 diameters long. This configuration is schematically illustrated in figure 7, where the equations which describe the variation of the radius of the body with axial distance are also indicated. In this problem the axis of the body, which is straight in this case, was chosen as the principal axis for the equivalence analogy between the steady and unsteady flows.

The fuselage had a drooped nose which resulted in a curved central axis of the body. This geometry is schematically illustrated in figure 8. The central axis of the body is composed of a straight portion, inclined  $7\frac{1}{2}^\circ$  from the horizontal, and a curved portion which begins at a horizontal station of 15 inches (see figure 8.) To avoid introducing curvature effects into the equations of motion, the  $7\frac{1}{2}^\circ$

reference line was chosen as the principal axis for the equivalence analogy. In this coordinate system, the angle of attack of  $15^{\circ}$  with respect to the horizontal becomes  $7\frac{1}{2}^{\circ}$  with respect to the  $7\frac{1}{2}^{\circ}$  reference line; hence,  $\alpha = 7\frac{1}{2}^{\circ}$ . The canopy, included in this problem, is indicated in the cross sections normal to the  $7\frac{1}{2}^{\circ}$  reference line shown in figure 8.

The fuselage configuration has cross-sectional shapes normal to the  $7\frac{1}{2}^{\circ}$  reference axis whose peripheries can be approximated by circular arcs and straight lines. In fact, the fuselage cross section is circular to a horizontal station of 9.44 inches from its nose, is asymmetric between horizontal stations 9.44 and 10.88, and includes a circular canopy between horizontal stations 10.88 and 30.68. The fuselage cross section at a horizontal station at the canopy location is shown schematically in figure 9. The parameters describing this periphery are also indicated in the figure. These parameters have been curve-fitted as functions of distance along the central axis of the fuselage. The curve fits of the cross-sectional parameters are presented in Appendix D.

#### 4.2 MESHES USED

A subroutine of the AFTON 2PE computer code has been developed for generating finite-difference meshes around an asymmetric half-body of a general fuselage-shaped cross section. This subroutine is based on previous work on finite-difference mesh development for a circular cylinder (ref. 12). The general cross-sectional shape of the half-body is assumed to consist of two circular arcs, two straight-line segments tangent to the circular arcs, and a circular canopy (see figure 9). The procedure adopted in the calculation was as follows: The area of the half-body was computed and a half-circle of equivalent

area was located with its center at the coordinate origin. The finite-difference mesh for this half-circle was calculated from a modified stream function and potential function from potential flow theory about a cylinder. The problem was to transform the cylinder mesh into a new mesh around the asymmetric half-body according to some suitable rule of transformation. In the subroutine developed, each half-circle mesh point (designated hereafter as an "unprimed" mesh point) was transformed into a half-body mesh point (designated hereafter as a "primed" mesh point) in the following manner. First, the periphery of the half-body shape was divided into as many equal arcs as the half-circle periphery. Then, surface vector displacements were obtained between corresponding unprimed points on the half-circle and primed points on the asymmetric half-body. Based on these surface vector displacements, unprimed mesh points in the flow field were displaced to their primed locations. Consider an unprimed mesh point in the flow field having a position vector  $\underline{R}(j,k)$ , where the integer,  $k$ , is associated with a potential-like line, and the integer,  $j$ , is associated with a streamline-like line. Let the surface vector displacement corresponding to the same  $k$  line be denoted as  $\underline{d}(k)$ . The position vector of the primed point  $\underline{R}'(j,k)$  is determined from the following equation:

$$\underline{R}'(j,k) = \underline{R}(j,k) + \underline{d}(k) \left[ \frac{a}{R(j,k)} \right]^2 \quad (31)$$

where  $a$  is the radius of the half-circle and  $R(j,k)$  is the magnitude of the position vector  $\underline{R}(j,k)$ .



The finite-difference meshes for the ogive-cylinder were composed of 35 j lines and 90 k lines and continuously deformed with the radius of the body. The initial radius was 0.00046875 foot and the maximum radius was 0.046875 foot. Since the ogive-cylinder cross section is circular, only the equations of the mesh generating subroutine which pertained to the circular cylinder mesh points (unprimed mesh points) were used to continually calculate new meshes as the radius of the cross section changed. The finite-difference mesh in a cross-sectional plane normal to the body axis at a radius of 0.01 foot is shown in figure 10. The finite-difference mesh corresponding to the maximum radius (0.046875 ft) is indicated in figure 11.

The finite-difference meshes for the fuselage configuration were composed of 35 j lines and 99 k lines and continuously deformed as the body cross-sectional shape deformed. The mesh-generating subroutine of the AFTON 2PE computer code continually calculated new meshes as the fuselage shape deformed. The finite-difference mesh in the cross-sectional plane normal to the central axis at a horizontal station 7 inches from the nose of the fuselage is shown in figure 12. At this station the fuselage cross section is circular. The finite-difference mesh corresponding to a horizontal station 25 inches from the fuselage nose is shown in figure 13. The canopy is also indicated in this figure.

#### 4.3 BOUNDARY CONDITIONS AND INITIAL CONDITIONS

In the x,y planes, the finite-difference meshes are bounded by an upstream boundary, a lateral boundary, and a boundary composed of the symmetry line of the cross section and the body cross section itself. The density and specific internal energy are given their free-stream values at the upstream boundary while the velocity of material normal to this boundary,  $v_{\infty}$ , is evaluated from

$$v_{\infty} = U_{\infty} \sin \alpha \quad (32)$$

where  $\alpha$  is the angle of attack with respect to the principal axis. Equations (5) and (6) are satisfied at the body's surface, while the fluid is allowed to slide without friction at the system's lateral boundary and symmetry lines. The downstream boundary condition was based on the method of characteristics. It was used previously in low-speed wake-flow calculations and gave a good approximation to the flow in this region. References 12 and 13 describe this downstream boundary condition in some detail.

The initial conditions for both problems consisted of a uniform flow field in the (x,y) plane with zero x-component the velocity and the y-component the velocity given by equation (32). The density and specific internal energy were given their free stream values. In both problems the initial cross sectional radius was approximately one-hundredth of the maximum cross sectional radius.

#### 4.4 RESULTS OF OGIVE-CYLINDER PROBLEM

The ogive-cylinder problem was the first attempted in this study. This problem was a good test of the method in that vortices had been experimentally observed to occur on the leeward side of the body. The crossflow Mach number was 0.344 and the crossflow Reynolds number was  $0.7625 \times 10^5$  based on the maximum diameter of the body. The problem was run 3406 cycles (i.e., time steps) on the UNIVAC 1108 computer, requiring approximately 10 hours of computer time. Solutions were obtained from the body's nose to an axial station 8.35 maximum cylinder diameters downstream. At this cross-sectional plane a well-developed pair of vortices were calculated. The problem duplicated the body geometry and free-stream conditions of a wind-tunnel test (ref. 14). In general, agreement between numerical and experimental data was good, providing evidence that the numerical method is applicable to bodies for which separation and subsequent development of spiral vortex sheets occur.

##### 4.4.1 Qualitative Behavior of Numerical Flow Field

To investigate the qualitative behavior of the flow field, it was convenient to exhibit the data in the form of vector plots of the velocities of the fluid particules; the tail of each vector corresponds to a mesh point.

The sequence of events as one moves down the axis of the body is described by figures 14 to 17. In figure 14 the flow field is shown at a station 0.502 maximum cylinder diameters from the nose of the body. Although the finite-difference mesh is relatively coarse with respect to the radius of the body at this station, the bow shock is indicated as well as the expansion which occurs on the leeward side. In figure 15, at a station 2.99 maximum body diameters, where the ogive section ends, the bow shock is better defined. Figure 16 shows the flow field at a station of 4.92 maximum diameters, where separation first appears on the leeward side of the body. The spiral vortex sheets that develop on the leeward side of the body are indicated in figure 17. The formation of the bow shock, the leeward expansion, and subsequent development of the spiral vortex sheets are all in qualitative accord with experimental observations. The accuracy of these numerical results is considered below.

#### 4.4.2 Surface Pressure Comparisons

Numerical pressure distributions around the body are compared to experimental data at various axial stations in figure 18. As can be seen from the figure, quantitative agreement is achieved from the body nose to an axial station 4.92 diameters. At this station the numerical data indicate that separation had occurred on the leeward side of the body (see the velocity vector plot in fig. 16), whereas the experimental data showed leeward separation at a station approximately 6.00 diameters aft of the body's nose. As a result, the numerical pressure data on the leeward side of the body differed slightly from the experimental data between stations 4.92 and 6.00 diameters down the body axis. At stations greater than 6.00 diameters from the cylinder's nose, the experimental data also showed separated flow, and the numerical and experimental pressure coefficient data were in close agreement 7.63 diameters from the nose of the cylinder.

#### 4.4.3 The Flow Field About the Ogive-Cylinder

The circumferential positions of the separation points and vortex centers vary with axial location in a manner determined experimentally by measurements of pitot pressure at various body cross sections. Corres-

ponding separation point and vortex center positions were also found from velocity plots of the numerical flow field. The calculated separation points and vortex centers were found to lie about  $20^\circ$  closer to the windward side than the corresponding experimental values as seen in figure 19. For example, in a crossflow plane 8.3 diameters down the body axis, the numerical separation point and vortex location were  $109^\circ$  and  $137^\circ$ , respectively, while the corresponding experimental values were  $130^\circ$  and  $160^\circ$ . The discrepancy between measured and calculated separation point and vortex center positions, while not very large, is perhaps the least satisfactory feature of the calculation. The difference is due to viscous effects of axial motion being neglected as well as to the exclusion of turbulence phenomena.

The flow field predicted numerically is laminar. However, the actual flow field is turbulent as a result of both axial and crossflow viscous effects. In the numerical method axial motion is treated as if the flow were inviscid. For laminar flow, separation would begin on the leeward side of the body at an axial station upstream of the station at which turbulent separation begins. Also, the separation point would be closer to the windward side when the flow is laminar. From the pressure coefficient data for a circular cylinder (ref. 15), it was found that in turbulent flow at a Reynolds number of  $6.7 \times 10^5$ , separation occurred at  $120^\circ$ ; in laminar flow at a Reynolds number of  $1.85 \times 10^5$ , separation occurred at  $90^\circ$ . Thus, the difference between the numerical and experimental separation positions is in qualitative agreement with the difference between laminar and turbulent separation positions. To obtain more realistic theoretical predictions, it will, therefore, be necessary to generalize the equivalence principle to account for turbulent effects due to axial flow; it is felt that the principle, which was generalized for this program by including Newtonian viscosity in the crossflow equations, could be extended satisfactorily by the addition of eddy viscosity terms.

#### 4.4.4 Accuracy of the Ogive-Cylinder Calculations

Based on the equivalence principle theory, an error analysis of the surface pressure results of figure 18 was made. The maximum slope of the ogive-cylinder body with respect to the free-stream flow direction was

28.92° which corresponds to a  $\tau = 0.552$ , and occurs on the windward side of the body at the nose. For this value of  $\tau$ , the hypersonic similarity parameter  $M_\infty \tau$  is 1.09, which satisfies the consistency condition of the theory. Since consistency is satisfied, the maximum absolute error in the surface static pressures,  $|\Delta P|$ , that one should expect from this theory is about 19 percent of the free-stream dynamic pressure [see eq. (21)]. The maximum absolute error in surface static pressure, or maximum difference between numerical and experimental pressures, for each of the cross sections of figure 18 is presented in table 1. Table 1 shows that the errors are very much less than the maximum error calculated from the equivalence principle theory of Van Dyke. It is believed that the static pressure errors in the vicinity of the body's nose would be of the order of 19 percent and would decay rapidly as  $\tau$  decreased. For example, at the station 0.502 diameters, the parameter  $\tau$  is 0.481, which results in a predicted absolute maximum error of 11 percent of free-stream dynamic pressure. Therefore, the numerical results are consistent with the equivalence principle theory of Van Dyke.

TABLE 1. MAXIMUM SURFACE PRESSURE ERROR IN VARIOUS CROSS-SECTIONAL PLANES

Axial station, maximum cylinder diameter	$ \Delta P /q \times 100$ , percent
0.502	5
2.990	1
1.289	3
3.970	5
4.920	4
5.830	4
7.630	3

#### 4.4.5 Drag and Lift Coefficients

Drag and lift coefficients were determined on the basis of numerical pressure data only; shear stress effects were not included. To compute these coefficients, the pressure coefficients on the ogive-cylinder surface were numerically integrated to determine the lift and drag.

Comparison of the numerical and experimental coefficients, as shown in figure 20, was found to be very satisfactory. The coefficients of total drag from the two sources proved to be almost identical functions of distance from the nose of the ogive. Differences in the lift coefficient curves began to be significant at a distance of about 2.75 diameters from the nose of the ogive, increased to a maximum at about 4.5 diameters, and then decreased; the numerical lift coefficient was approximately 5.8 percent higher than that measured at about 4.5 diameters from the ogive nose, and about 2 percent higher at 8.35 diameters from the nose.

An overestimated lift coefficient is consistent with the fact that separation occurred earlier in the numerical flow field than in the experimental field. Lift coefficients are calculated from pressure forces on the surface of the body, as projected in a plane parallel to that of free-stream flow. Since the area of the appropriate projection is almost entirely derived from the body's long cylindrical surface, and separation takes place on that surface, separation that occurs too early increases the lift.

On the other hand, the drag coefficient should be relatively independent of the location of separation. Since the ogive becomes cylindrical at a station 3.0 diameters from its nose, the projected surface area normal to the direction of free-stream flow is very small for the long cylindrical surface aft of this station, and the corresponding pressure forces contribute very little to the total drag. Quantitative agreement in the pressure drag coefficients is, therefore, physically reasonable.

#### 4.5 RESULTS OF FUSELAGE PROBLEM

For the fuselage problem the crossflow Mach number was 0.288 and the crossflow Reynolds number was  $1.15 \times 10^6/\text{ft}$ . Cross-section flows have been calculated in this problem in planes normal to the  $7\frac{1}{2}^\circ$  reference line to a horizontal station 19.5 inches aft of the nose. At this station the curve bounding the body's surface represents an asymmetric fuselage configuration with a canopy. To reach this station the problem was run 2079 cycles (time steps) on the UNIVAC 1108 computer. This calculation required approximately 6 hours of computer time.

#### 4.5.1 Qualitative Behavior of Numerical Flow Field

From velocity vector plots of the cross-sectional flow field, the qualitative behavior of the fuselage flow can be examined. The sequence of events as one moves downstream along the  $7\frac{1}{2}^\circ$  reference line of the fuselage is indicated in figures 21 to 25. The vectors in these figures correspond to the particle velocities of the flow at each mesh point of the finite difference mesh; the tail of each vector corresponds to the mesh point. Initially, a bow shock forms at the nose and an expansion fan, caused by the interaction between the expanding body and the crossflow, appears on the leeward side. This is indicated in figure 21 at a station 1.135 inches from the fuselage nose. This flow pattern continues as the fuselage cross section grows until it reaches the canopy which induces a shock wave in the flow field (see fig. 23). As the canopy radius reaches maximum (fig. 24) and starts to decrease, a rarefaction develops in the flow field above the canopy, leading to the formation of vortices (fig. 25).

#### 4.5.2 Surface Pressure Comparison

The quantitative behavior of the predicted flow about the fuselage was ascertained by comparing the numerical results to experimental measurements. The fuselage configuration of figure 6 was tested in the Ames 8- by 7-Foot Wind Tunnel. Static pressures were measured along the surface of the fuselage, and flow-field measurements with conical probes were made in cross-sectional planes normal to the horizontal reference line at a station 19.5 inches aft of the fuselage nose. The static-pressure instrumentation of the fuselage forebody surface is sketched in figure 26. The pressure taps were located in cross-sectional planes normal to the horizontal reference line. The point of intersection of the  $7\frac{1}{2}^\circ$  reference line with this cross-sectional plane defined the axis from which pressure tap locations were measured along the periphery of the cross section. Pressure taps were located  $-90^\circ$ ,  $-60^\circ$ ,  $-30^\circ$ ,  $0^\circ$ , and  $+24^\circ$  from this axis (see fig. 26). Thus, with respect to stations along the horizontal reference line, the instrumentation was located along the five planes indicated in figure 26.

Numerical and experimental distributions of surface pressure coefficients are compared in figure 27 along the five planes of figure 26. It is seen that excellent agreement has been achieved along the  $-90^\circ$ ,  $-60^\circ$ , and  $-30^\circ$  planes. The numerical and experimental pressure coefficients agree along the  $0^\circ$  plane until station 18. Along the  $24^\circ$  plane there is a discrepancy at station 15. These discrepancies can be attributed to two sources: (a) a canopy shock wave-axial boundary-layer interaction, which occurs experimentally but not numerically, and (b) a slightly different calculated canopy shock location which will be described in more detail in the discussion of the flow-field results. The canopy shock-axial boundary-layer interaction spreads the shock pressure rise over a greater distance than calculated.

#### 4.5.3 Accuracy of the Fuselage Calculations

As in the case of the ogive-cylinder problem, an error analysis was made of the surface static pressures. The maximum slope of the fuselage geometry with respect to the free-stream flow occurred on the windward side of the body at its nose (see fig. 8). Its value was  $22^\circ$ , which corresponds to  $\tau = 0.400$  and  $M_\infty \tau = 0.998$ . Therefore, the consistency condition of the theory is satisfied. According to equation (22), the maximum absolute error then becomes 5 percent of the free-stream dynamic pressure. On the basis of the results of figure 27, the maximum error,  $|\Delta P|/q_\infty$ , in each of the planes was determined and the values are tabulated in table 2. It is seen from the table that the errors recorded are consistent with the maximum error calculated from the equivalence principle theory.

TABLE 2. MAXIMUM SURFACE PRESSURE ERROR ALONG THE FIVE PLANES OF FIGURE 33

Plane, deg	$ \Delta P /q_\infty \times 100$ , percent
- 90	2.0
- 60	2.3
- 30	3.4
0	5.6
24	5.8



At first glance the relatively small errors of table 2 are surprising in lieu of the fact that hypersonic small disturbance theory is applied at supersonic speed. One would expect linearized supersonic theory to apply in this Mach number range. However, an analysis of the errors shows that linearized supersonic theory is only slightly more accurate than hypersonic small disturbance theory for the fuselage problem. The error in linearized supersonic theory is of the order  $\tau$  (ref. 2), which results in a maximum absolute error in the static pressure of 4% of free stream dynamic pressure. Therefore, for a relatively thick class of bodies (which includes most fuselage geometries), where the hypersonic similarity parameter is of order unity, both hypersonic small disturbance theory and linearized supersonic theory give satisfactory results.

#### 4.5.4 Contour Maps in the Flow Field of the Fuselage

Contour plots of the local pitot pressure ratio ( $P_p/P_{s\infty}$ ), local sideslip angle ( $\beta$ ), local Mach number ( $M$ ), local angle of attack ( $\alpha_e$ ), and local total pressure ratio ( $P_s/P_{s\infty}$ ) were generated from the numerical results and compared to corresponding contour plots from experimental data. The comparisons were made in a cross-sectional plane normal to the horizontal reference line at a station 19.5 inches from the fuselage apex. See figures 28 through 32. The above parameters are defined in Appendix E.

The local pitot pressure,  $P_p$ , is effectively the stagnation pressure measured by a probe whose axis is parallel to the local flow direction. As in the case of the surface pressures the pitot pressure is measured directly; therefore, it provides a reliable measurement for comparison. The numerical pitot pressure was calculated from the Rankine-Hugoniot equations for a normal shock, where upstream of the shock, the local Mach number, and stagnation pressure were assumed to exist. The numerical and experimental pitot pressure ratios ( $P_p/P_{s\infty}$ ) of figure 28 indicate good agreement in the lower quadrant of the flow field, where the two sets of  $P_p/P_{s\infty}$  contours are nearly coincident in the vicinity of the body. This

quantitative agreement is in accord with the agreement obtained between surface static pressures on the  $-30^\circ$  plane, which intersects the body in this region. In the upper quadrant of the flow field there is a discrepancy between the experimental and numerical contours. The numerical results indicate that the canopy shock intersects the fuselage surface above that point indicated by the experimental data. The increased downward distance of travel by the canopy shock in the experimental case accounts for the discrepancy in contours in the upper quadrant of the flow field. Although axial-boundary layer effects and discretization errors influence the canopy shock location, it is believed that the equivalence principle approximation of neglecting the velocity perturbation along the  $7\frac{1}{2}^\circ$  reference line is the primary cause of this discrepancy. The velocity perturbation is effectively zero upstream of the body apex, hence, the windward oblique shock emanating from the apex was calculated correctly. However, the velocity perturbation is positive upstream of the canopy, and since this quantity is neglected in the method, the calculated canopy shock must be, and is, weaker than experimentally measured.

The local sideslip angle,  $\beta$ , is measured in the cross-sectional plane normal to the horizontal reference line and is the flow inclination in the  $x', z'$  plane (see fig. 9). As in the case of the pitot pressures, the comparison of the experimental and numerical sideslip angle contours shown in figure 29 indicates that the predicted flow field in the lower quadrant is nearly correct. Furthermore, the predicted location of the canopy shock and the predicted flow-field contours in the upper quadrant deviate from experiment as in the pitot pressure comparisons.

Contours of constant Mach number and constant local angle of attack with respect to the horizontal reference line (see fig. 8) are presented in figures 30 and 31, respectively. It is seen from these figures that the numerical Mach number and angle-of-attack contours do not match the experimental contours even in the lower quadrant of the flow field. This discrepancy is not in accord with the surface static pressure comparison, pitot pressure comparison, and sideslip angle comparison discussed previously.

The reasons for this disagreement can be found in discretization errors in the numerical method, errors introduced by the equivalence principle assumption, and errors inherent in the experiment and data reduction process. The error in Mach number due to the equivalence principle has been determined previously [see eq. (28)]. Equation (28), evaluated with  $\tau = 0.40$  and  $M_\infty = 2.5$ , results in a maximum absolute error of about 30 percent of the free-stream Mach number. This corresponds to an absolute Mach number error of about 0.75. Consider the experimental contour of figure 30 for a constant Mach number of 2.50. It is seen from figure 30 that this contour coincides with the numerical contour for a constant Mach number of 2.40, which results in an absolute Mach number difference of 0.10. Thus, the observed absolute difference in Mach number between the numerical and experimental results is within the maximum error one would expect from the equivalence principle alone. Therefore, one must conclude that errors introduced by the equivalence principle assumption account for the major part of these discrepancies.

The calculated local total pressure recovery contours ( $P_s/P_{s\infty}$ ) are shown in figure 32. The predicted total pressure recovery varies from 1.0 to 0.88 in the flow field, with recoveries near 1.0 throughout most of the flow region. This parameter is the most difficult to calculate accurately and to determine experimentally. Although the experimental data for this fuselage configuration are still preliminary, an error analysis indicates that the values of  $P_s/P_{s\infty}$  can be determined only with  $\pm 0.03$ . For a total pressure ratio bandwidth from 0.88 to 1.0, this error is too large to yield any significant contour data. Consequently, no experimental data are shown. Future refinement of the set of conical probe calibration data will hopefully reduce this error to a more meaningful level.

#### 4.5.5 Lift and Drag Coefficients

Numerical lift and drag coefficients for the fuselage problem are compared to corresponding lift and drag coefficients determined from inviscid, linearized supersonic theory for flow about an axisymmetric body at angle of attack (ref. 16). Linearized supersonic theory was used because there were not enough pressure data to determine the lift and drag experimentally. The lift and drag coefficients from the numerical method were determined by numerical integration of the surface pressure coefficients over the surface and are based on a cross-sectional area corresponding to the maximum equivalent radius of the fuselage,  $a_{\max} = 3$  inches. As in the case of the ogive-cylinder problem, shear stress effects were not included. It is seen from figure 33 that the numerical lift coefficient distribution nearly corresponds to that from linearized supersonic theory. In view of the fact that the maximum absolute static pressure errors are about the same for both linearized supersonic theory and hypersonic small disturbance theory, agreement in the lift coefficient is expected. On the other hand, the numerical drag coefficient distribution shows greater drag than the distribution from linearized supersonic theory. This discrepancy may be attributed to the fact that the coefficients determined from linearized supersonic theory have been further specialized to the case of very slender bodies (ref. 16), which is not true for this geometry. However, this comparison does indicate that the lift and drag coefficients calculated by the numerical method of this paper, if not correct, are at least of the right order.

## 5.0 CONCLUSIONS AND RECOMMENDATIONS

The principal conclusion emerging from the work reported here is that a promising new method has been developed for calculating flow fields about slender bodies of arbitrary geometry in the supersonic and hypersonic flight regimes. The present version of the numerical method can adequately predict the surface pressures and flow field characteristics outside the boundary layer for bodies where the hypersonic similarity parameter  $M_\infty \gamma$  is unity or greater and for free stream Mach numbers 2 and above. For cases where boundary layer separation and the subsequent formation of spiral vortex sheets occur, the numerical method predicts too early a separation which results in small inaccuracies in predicted flow field quantities downstream of the region of separation.

The basis for the above conclusion lies mainly in the specific results obtained for the ogive-cylinder and the fuselage configurations. For the ogive-cylinder problem a spiral vortex pair was computed on the leeward side of this body. Although axial effects caused some differences between numerical and experimental separation regions and vortex center positions, in general, the static pressure distributions on the body's surface, the lift, and pressure drag of the body agreed with the corresponding experimental values; the surface pressures differed by no more than 5 percent of free-stream dynamic pressure; the lift coefficients differed by no more than 6 percent; and the drag coefficients by no more than 2 percent. From velocity vector plots of the cross-sectional flow field of the fuselage configuration, the structure of the flow field seemed correct, at least qualitatively. Furthermore, comparisons of the numerical static pressure distributions on the fuselage surface were in quantitative agreement with experimentally determined distributions; the maximum error in the static pressure was no more than 6 percent of free stream dynamic pressure. Contour plots of pitot pressures were of the same general shape as the experimental contours and some of these curves

coincided. Finally, the pressure drag and lift distributions seemed correct when compared to corresponding drag and lift coefficients derived from inviscid, linearized supersonic flow theory.

The justification for the part of the above conclusion which pertains to the range of applicability of the method, i.e.,  $M_{\infty T} \geq 1$  and  $M_{\infty} \geq 2$ , lies mainly in the fact that for both problems ( $M_{\infty T} \approx 1$ ,  $M_{\infty} = 1.98$ , and  $M_{\infty} = 2.5$ ) the deviations predicted from experimental results were contained well within the predicted error bounds of the equivalence principle. Hence, as the Mach number  $M_{\infty}$  increases, the Van Dyke theory tells us that the predicted results will become more accurate. However, to strengthen this conclusion, additional comparisons should be made between numerical and experimental data at other flight conditions and for different geometries within the above range of applicability.

To realize the full potential of this numerical method, we believe that further research is justified. Three areas of additional research seem promising. First, the method should be revised and include the velocity perturbation on the principal axis along which the equivalence analog is made. The inclusion of the axial velocity perturbation in the finite difference equations of motion will improve the accuracy of the method in its present range of applicability and will extend the method to cases where  $M_{\infty T} \ll 1$  and for Mach numbers above transonic. Hence, a unified method, which applies throughout the supersonic and hypersonic flight regimes, will be achieved.

The second area where additional research seems justified concerns the relationship between viscous axial and crossflow effects. In the ogive cylinder problem, too early a separation was calculated considering only viscous crossflow terms which were assumed laminar. The discrepancy in the separation point location is attributed to both axial viscous effects and turbulence. However, from the results of this problem it was not possible to determine which was the more important effect. Therefore, to determine the relationship between viscous axial and crossflow effects it is necessary to solve an additional problem (both numerically and experimentally) at hypersonic flight conditions and in the laminar

flow regime. At hypersonic flight conditions, errors in the equivalence principle are minimized; thus, deviations between numerical and experimental results can be attributed entirely to the neglect of axial viscous effects. If these deviations are large, some of the more important axial viscous terms can be retained in the finite difference equations of motion.

Finally, turbulence effects can be included in the finite difference equations of motion by the addition of eddy terms, i.e., eddy viscosity and thermal conductivity. These eddy terms would be based on empirical constants which would be determined from comparisons of numerical and experimental results.

Along the lines just sketched, we believe that an efficient, reliable capability can be developed for predicting viscous flow field characteristics for nonsimple geometries throughout the supersonic and hypersonic flight regimes.

## APPENDIX A

### THE EQUIVALENCE PRINCIPLE

In this section the equivalence principle for steady, inviscid three-dimensional flow is derived. An Eulerian coordinate system fixed with respect to the body and having its z-axis along the axis of the body is used throughout this section (see figure 2).

The equations of motion for steady, inviscid three-dimensional flow about a body are:

#### Continuity

$$\frac{\partial}{\partial x} (\rho u) + \frac{\partial}{\partial y} (\rho v) + \frac{\partial}{\partial z} [\rho (U_{\infty} \cos \alpha + w)] = 0 \quad (A1)$$

#### Momentum

$$u \frac{\partial u}{\partial x} + v \frac{\partial u}{\partial y} + (w + U_{\infty} \cos \alpha) \frac{\partial u}{\partial z} = - \frac{1}{\rho} \frac{\partial P}{\partial x} \quad (A2a)$$

$$u \frac{\partial v}{\partial x} + v \frac{\partial v}{\partial y} + (w + U_{\infty} \cos \alpha) \frac{\partial v}{\partial z} = - \frac{1}{\rho} \frac{\partial P}{\partial y} \quad (A2b)$$

$$u \frac{\partial w}{\partial x} + v \frac{\partial w}{\partial y} + (w + U_{\infty} \cos \alpha) \frac{\partial w}{\partial z} = - \frac{1}{\rho} \frac{\partial P}{\partial z} \quad (A2c)$$

#### First Law

$$\begin{aligned} u \frac{\partial E}{\partial x} + v \frac{\partial E}{\partial y} + (w + U_{\infty} \cos \alpha) \frac{\partial E}{\partial z} = \\ - P \left[ u \frac{\partial}{\partial x} \left( \frac{1}{\rho} \right) + v \frac{\partial}{\partial y} \left( \frac{1}{\rho} \right) + (w + U_{\infty} \cos \alpha) \frac{\partial}{\partial z} \left( \frac{1}{\rho} \right) \right] \end{aligned} \quad (A3)$$



### Boundary Conditions at Body

$$(U_{\infty} \cos \alpha + w) \ell_z + v \ell_y + u \ell_x = 0 \quad (\text{A4a})$$

### Boundary Conditions at Shock

$$\rho_{\infty} U_{\infty} (\cos \alpha n_z + \sin \alpha n_y) = \rho_s [(U_{\infty} \cos \alpha + w_s) n_z + v_s n_y + u_s n_x] \quad (\text{A4b})$$

$$\begin{aligned} \rho_{\infty} + \rho_{\infty} U_{\infty}^2 (\cos \alpha n_z + \sin \alpha n_y)^2 &= P_s \\ + \rho_s [(U_{\infty} \cos \alpha + w_s) n_z + v_s n_y + u_s n_x]^2 & \end{aligned} \quad (\text{A4c})$$

$$\begin{aligned} \frac{\gamma}{\gamma - 1} \frac{P_{\infty}}{\rho_{\infty}} + \frac{1}{2} U_{\infty}^2 (\cos \alpha n_z + \sin \alpha n_y)^2 &= \frac{\gamma}{\gamma - 1} \frac{P_s}{\rho_s} \\ + \frac{1}{2} [(U_{\infty} \cos \alpha + w_s) n_z + v_s n_y + u_s n_x]^2 & \end{aligned} \quad (\text{A4d})$$

where  $E$  is the internal energy per unit mass,  $P$  is the pressure,  $\rho$  is the density,  $U_{\infty}$  is the free stream speed,  $w$  is perturbation velocity in the  $z$ -direction,  $v$  is the velocity in the  $y$ -direction,  $u$  is the velocity in the  $x$ -direction, and  $\ell_x$ ,  $\ell_y$ , and  $\ell_z$  are the direction cosines of the body normal in the  $x$ ,  $y$ , and  $z$  directions respectively. The subscript  $s$  refers to properties downstream of the shock, and  $n_x$ ,  $n_y$ ,  $n_z$  are the direction cosines of the shock normal in the  $x$ ,  $y$ , and  $z$  directions respectively.

### Boundary Conditions Far From Body

$$z = -\infty : \quad w = U_{\infty} \cos \alpha, \quad v = U_{\infty} \sin \alpha, \quad u = 0 \quad (\text{A5})$$

Introducing the transformation equations

$$\left. \begin{aligned} z &= U_{\infty} \cos \alpha t \\ y &= y \\ x &= x \end{aligned} \right\} \quad (\text{A6})$$

and the slender body assumption

$$U_{\infty} \gg w$$

into equations (A1) through (A6) yields

#### Continuity

$$\frac{\partial \rho}{\partial t} + \frac{\partial}{\partial x} (\rho u) + \frac{\partial}{\partial y} (\rho v) = 0 \quad (A7)$$

#### Momentum

$$\frac{\partial w}{\partial t} + u \frac{\partial w}{\partial x} + v \frac{\partial w}{\partial y} = - \frac{1}{\rho} \frac{\partial P}{\partial t} \left( \frac{1}{U_{\infty} \cos \alpha} \right) \quad (A8a)$$

$$\frac{\partial v}{\partial t} + u \frac{\partial v}{\partial x} + v \frac{\partial v}{\partial y} = - \frac{1}{\rho} \frac{\partial P}{\partial y} \quad (A8b)$$

$$\frac{\partial u}{\partial t} + u \frac{\partial u}{\partial x} + v \frac{\partial u}{\partial y} = - \frac{1}{\rho} \frac{\partial P}{\partial x} \quad (A8c)$$

#### First Law

$$\frac{\partial E}{\partial t} + u \frac{\partial E}{\partial x} + v \frac{\partial E}{\partial y} = - P \left[ \frac{\partial}{\partial t} \left( \frac{1}{\rho} \right) + u \frac{\partial}{\partial x} \left( \frac{1}{\rho} \right) + v \frac{\partial}{\partial y} \left( \frac{1}{\rho} \right) \right] \quad (A9)$$

#### Boundary Conditions at Body

$$\cos \alpha U_{\infty} \ell_z + u \ell_x + v \ell_y = 0 \quad (A10)$$

#### Shock Conditions

$$\rho_{\infty} U_{\infty} (-\cos \alpha \sin \beta + \sin \alpha \cos \beta) = \rho_s (v_s n_y + u_s n_x - U_{\infty} \cos \alpha \sin \beta) \quad (A11a)$$

$$P_{\infty} + \rho_{\infty} U_{\infty} (-\cos \alpha \sin \beta + \sin \alpha \cos \beta)^2 = P_s$$

$$+ \rho_s (v_s n_y + u_s n_x - U_{\infty} \cos \alpha \sin \beta)^2 \quad (A11b)$$

$$\frac{\gamma}{\gamma - 1} \frac{P_{\infty}}{\rho_{\infty}} + \frac{U_{\infty} (-\cos \alpha \sin \beta + \sin \alpha \cos \beta)^2}{2} = \frac{\gamma}{\gamma - 1} \frac{P_s}{\rho_s}$$

$$+ (v_s n_y + u_s n_x - U_{\infty} \cos \alpha \sin \beta)^2 \quad (A11c)$$

where:  $\beta$  is the angle made by the shock surface with respect to the z-axis in the (y,z) plane. Equations (A7), (A8b), (A8c), and (A9) are independent of w and, thus, represent the equations for time-dependent motion in the (x,y) plane. Therefore, the steady 3-D equations of motion have been transformed to a time-dependent 2-D set of equations. The 3-D shock boundary conditions also reduce to a nonsteady shock in the (x,y) plane moving with velocity proportional  $U_{\infty} \cos \alpha \sin \beta$ . In summary, the necessary and sufficient conditions for the equivalence principle to be valid are:

- a. The z-component of the local velocity vector must be approximately equal to the z-component of the free stream velocity vector, and
- b. the time-dependent solution in the (x,y) plane must satisfy the three-dimensional boundary condition equation (A10) at the body surface.

The calculational procedure for inviscid flow is then as follows: First, equations (A7), (A8b), (A8c), (A9), and (A10) are solved for v,u,P, and  $\rho$ . The perturbation velocity w may be subsequently obtained from the Bernoulli equation, which is

$$\frac{\gamma}{\gamma - 1} \frac{P}{\rho} + \frac{(w + U_{\infty} \cos \alpha)^2 + v^2 + u^2}{2} = \text{constant} \quad (A12)$$

Therefore, the equivalence between a steady-three-dimensional flow and a time-dependent two-dimensional flow is proven.

If the conditions (a), (b) are satisfied, viscous effects can be included in the time-dependent calculations in the (x,y) plane without violating the equivalence principle assumptions. A no-slip boundary condition can be applied at the surface of the cross section in the (x,y) plane in conjunction with the equivalence principle boundary condition equation (A10).

## APPENDIX B

### CONSERVATION OF TOTAL ENERGY

In this section the self-consistency property of form that the finite difference equations (8) to (13) possess is demonstrated. This demonstration proceeds in three steps. First, the finite difference kinetic energy equation is derived for the momentum zone  $a_{l-1/2}$ ,  $a_{l+1/2}$ . Then the finite difference First Law equation is derived for this momentum zone. Finally, these relations are added to determine the finite difference equation of total energy for the momentum zone  $a_{l-1}$ ,  $a_{l+1/2}$ .

The kinetic energy equation for momentum zone  $a_{l-1/2}$ ,  $a_{l+1/2}$  can be derived from momentum equation (12) which is centered at the time  $t^{n-1/2}$ . Equation (12) can be written in terms of velocities by employing the forward extrapolation relation, equation (13), i.e.,

$$\frac{1}{2} m_l \frac{(U_l^{n+1/2} - U_l^{n-3/2})}{\Delta t} = \left( P_{l-1/2}^{n-1/2} - P_{l+1/2}^{n-1/2} \right) \quad (B1)$$

Multiplication of equation (B1) by  $U_l^{n-1/2}$  yields the kinetic energy equation for momentum zone  $a_{l-1/2}$ ,  $a_{l+1/2}$ .

$$\begin{aligned} \frac{m_l}{\Delta t} \left[ \frac{U_l^{n+1/2} U_l^{n-1/2}}{2} - \frac{U_l^{n-1/2} U_l^{n-3/2}}{2} \right] \\ = U_l^{n-1/2} \left( P_{l-1/2}^{n-1/2} - P_{l+1/2}^{n-1/2} \right) \end{aligned} \quad (B2)$$

The First Law equation for momentum zone  $a_{l-1/2}$ ,  $a_{l+1/2}$  is derived as follows: the internal energy for this zone equals half the sum of the internal energies of thermodynamic zones  $a_{l-1}$ ,  $a_l$  and  $a_l$ ,  $a_{l+1}$  (see equations (9) and (10)). This division of internal energy comes directly from the relationship between thermodynamic and momentum zones specified when the physical model of figure 6 was postulated. The

$-P \frac{\Delta v}{\Delta t}$  term for momentum zone  $a_{l-1/2}$ ,  $a_{l+1/2}$  comes from half the  $-P \frac{\Delta v}{\Delta t}$  for thermodynamic zones  $a_{l-1}$ ,  $a_l$  and  $a_l$ ,  $a_{l+1}$ . The First Law equation for momentum zone  $a_{l-1/2}$ ,  $a_{l+1/2}$  becomes:

$$m_l \left[ \frac{\frac{1}{2} (E_{l-1/2}^n + E_{l+1/2}^n) - \frac{1}{2} (E_{l-1/2}^{n-1} + E_{l+1/2}^{n-1})}{\Delta t} \right] =$$

$$- \frac{1}{2} \left[ \frac{(P_{l-1/2}^{n-1} + P_{l-1/2}^n)}{2} (U_l^{n-1/2} - U_{l-1}^{n-1/2}) \right.$$

$$\left. + \frac{(P_{l+1/2}^{n-1} + P_{l+1/2}^n)}{2} (U_{l+1}^{n-1/2} - U_l^{n-1/2}) \right] \quad (B3)$$

The finite difference equation for conservation of total energy for momentum zone  $a_{l-1/2}$ ,  $a_{l+1/2}$  results from the addition of equations (B2) and (B3).

$$m_l \frac{(H_l^n - H_l^{n-1})}{\Delta t} = (W_{l-1/2}^{n-1/2} - W_{l-1/2}^{n-1/2}) \quad (B4)$$

where:

$$H_l^n = (E_{l-1/2}^n + E_{l+1/2}^n) \frac{1}{2} + \frac{U_{l-1/2}^{n-1/2} U_{l+1/2}^{n-1/2}}{2}$$

$$W_{l-1/2}^{n-1/2} = \frac{(P_{l-1/2}^n + P_{l-1/2}^{n-1})}{2} \frac{(U_l^{n-1/2} + U_{l-1}^{n-1/2})}{2}$$

$$W_{l+1/2}^{n-1/2} = \frac{(P_{l+1/2}^n + P_{l+1/2}^{n-1})}{2} \frac{(U_{l+1}^{n-1/2} + U_l^{n-1/2})}{2}$$

Equation (B4), derived from finite difference analogs of the First Law and momentum equations, is a reasonable finite difference expression for total energy conservation. The rate of work done on the surface, having the Lagrangian coordinate  $a_{l-1/2}$  at time  $t^{n-1/2}$ , is the product of the time-averaged pressure in the thermodynamic zone  $a_{l-1}$ ,  $a_l$  and the space-average velocity between surfaces  $a_{l-1}$

and  $a_\ell$ . The internal energy of the momentum zone  $a_{\ell-1/2}, a_{\ell+1/2}$  at time  $t^n$ , is half the internal energy of the two thermodynamic zones which contain it. Finally, the kinetic energy of momentum zone  $a_{\ell-1/2}, a_{\ell+1/2}$  at time  $t^n$ , is the product of the velocities at the surface  $a_\ell$ , at times  $t^{n-1/2}$  and  $t^{n+1/2}$ . It is believed that this self-consistency of form property, which the differential equations possess, and which the finite equations preserve, is the primary reason for their success in numerical calculation of one-dimensional time-dependent flow fields.

## APPENDIX C

### AFTON 2PE FINITE DIFFERENCE EQUATIONS AT INTERIOR MESH POINTS

The AFTON 2PE finite difference equations are presented for a generalized coordinate system. The field of motion in AFTON 2P is actually covered with two closely related finite difference meshes -- one for the calculation of thermodynamic variables such as stress, i.e., quadrilateral zones, and the other for the calculation of kinematic variables like momentum, i.e., momentum zones (refs. 11 and 12). Figure 4 illustrates the two types of meshes in two space dimensions. The continuity and first law equations are applied to calculate properties on a quadrilateral zone while the equations of momentum and total energy conservation are used to calculate properties on a momentum zone. In the forthcoming analysis quadrilateral 1, 2, 3, 4 and momentum zone a, b, c, d are considered (see figure 4). The finite difference equations in the generalized coordinate system are as follows:

#### Definitions:

$\underline{R} = \underline{R}(x,y)$	Cartesian coordinate position relative to the moving frame
$\underline{U} = \underline{U}(u,v)$	material velocity relative to the laboratory frame
$E$	internal energy
$\underline{\hat{i}}$	unit vector in the x-direction (i.e., the plane of flow, and normal to the free stream flow relative to the laboratory frame)
$H$	total energy
$W$	rate of work
$\underline{S} = \underline{S}(x,y)$	mesh point velocity relative to the laboratory frame
$\rho$	material density



$\hat{k}$	unit vector normal to (x,y) plane
m	mass
V	volume
$\underline{M}$	momentum
$\mu$	viscosity
t	time
$\Delta t$	timestep, $t = t' - t^0$
$\gamma$	ratio of specific heats
P	fluid pressure
$\sigma'_x, \sigma'_y, \sigma'_{xy}$	viscous stresses
P	$\begin{pmatrix} P & 0 \\ 0 & P \end{pmatrix}$
$\sigma''$	$\begin{pmatrix} \sigma'_x & \sigma'_{xy} \\ \sigma'_{xy} & \sigma'_y \end{pmatrix}$
$\sigma$	$P - \sigma''$
$( )^0$	denotes property at initial time, $t^0$
$( )'$	denotes property at final time, $t'$
$( )^{-t}$	denotes property a half timestep before initial time $t^0$
$( )$	denotes property a half timestep before final time $t'$
$( )$	denotes timestep, a half timestep after final time $t'$

### Equations

$$\underline{R}' = \underline{R}'(\underline{t}', \text{cross sectional geometry}) \quad (C1)$$

$$\underline{R} = \frac{1}{2}(\underline{R}' + \underline{R}^0) \quad (C2)$$

$$\underline{S} = (\underline{R}' - \underline{R}^0)/\Delta t \quad (C3)$$

$$\underline{U} = \underline{U}(u, v) \quad (C4)$$

$$\underline{A}_{12} = (\underline{R}_1 - \underline{R}_2) \times \underline{k} \quad (C5)$$

$$\underline{A}_{32} = (\underline{R}_3 - \underline{R}_2) \times \underline{k} \quad (C6)$$

$$\underline{W}_{12} = \frac{1}{2}(\underline{U}_1 + \underline{U}_2) \quad (C7)$$

$$\underline{S}_{12} = \frac{1}{2}(\underline{S}_1 + \underline{S}_2) \quad (C8)$$

$$\underline{W}_{32} = \frac{1}{2}(\underline{U}_3 + \underline{U}_2) \quad (C9)$$

$$\underline{S}_{32} = \frac{1}{2}(\underline{S}_3 + \underline{S}_2) \quad (C10)$$

$$(\rho WA)_{12} = \rho_{12}(\underline{W}_{12} - \underline{S}_{12}) \cdot \underline{A}_{12} \quad (C11)$$

$$(\rho WA)_{32} = \rho_{32}(\underline{W}_{32} - \underline{S}_{32}) \cdot \underline{A}_{32} \quad (C12)$$

$$V' = V'(t', \text{cross-sectional geometry}) \quad (C13)$$

$$V = (V' + V^0)_{\frac{1}{2}} \quad (C14)$$

$$m^1 = m^0 + \Delta t \left[ -(\rho WA)_{12} + (\rho WA)_{32} + (\rho WA)_{43} - (\rho WA)_{41} \right] \quad (C15)$$

$$\rho^1 = m^1 / V^1 \quad (C16)$$

$$d_{ix} = x_i(y_{i-1} - y_{i+2}) + x_{i-1}(y_{i+2} - y_i) + x_{i+2}(y_i - y_{i-1}) \quad (C17)$$

where:  $i=1,2,3,4$  and, for example, when  $i=1$ ,  $i-1=4$

$$d_{iy} = -d_{ix} \quad (C18)$$

$$A_{ix} = \frac{1}{4} \left[ (y_{i-1} - y_{i+2})/d_{ix} + (y_{i-1} - y_{i+1})/d_{i+1} x \right. \quad (C19)$$

$$\left. + (y_{i+2} - y_{i-1})/d_{i+2} x \right]$$

$$A_{it} = \frac{1}{4} \left[ (x_{i-1} - x_{i+2})/d_{iy} + (x_{i-1} - x_{i-1})/d_{i+1} x \right. \quad (C20)$$

$$\left. + (x_{i+2} - x_{i-1})/d_{i+2} y \right]$$

$$\frac{\partial u}{\partial x} = A_{1x}u_1 + A_{2x}u_2 + A_{3x}u_3 + A_{4x}u_4 \quad (C21)$$

$$\frac{\partial u}{\partial y} = A_{1y}u_1 + A_{2y}u_2 + A_{3y}u_3 + A_{4y}u_4 \quad (C22)$$

$$\frac{\partial v}{\partial x} = A_{1x}v_1 + A_{2x}v_2 + A_{3x}v_3 + A_{4x}v_4 \quad (C23)$$

$$\frac{\partial v}{\partial y} = A_{1y}v_1 + A_{2y}v_2 + A_{3y}v_3 + A_{4y}v_4 \quad (C24)$$

$$\sigma'_x = \mu \left[ \frac{2}{3} \frac{\partial v}{\partial y} - \frac{4}{3} \frac{\partial u}{\partial x} \right] \quad (C25)$$

$$\sigma'_y = \mu \left[ \frac{2}{3} \frac{\partial u}{\partial x} - \frac{4}{3} \frac{\partial v}{\partial y} \right] \quad (C26)$$

$$\tau'_{xy} = -\mu \left[ \frac{\partial u}{\partial y} + \frac{\partial v}{\partial x} \right] \quad (C27)$$

$$\tilde{P} = (\gamma - 1) \rho^1 E^0 \quad (C28)$$

$$\underline{A}_{42} = \frac{1}{2}(\underline{R}_4 - \underline{R}_2) \times \hat{k} \quad (C29)$$

$$\tilde{\underline{F}}_{42} = \sigma^0 + \tilde{P} - (\sigma'')^1 \cdot \underline{A}_{42} \quad (C30)$$

$$(\rho WAE)_{12} = (\rho WA)_{12} E_{12} \quad (C31)$$

$$E_t = -(\rho WAE)_{12} + (\rho WAE)_{32} + (\rho WAE)_{43} - (\rho WAE)_{41} \quad (C32)$$

$$\tilde{E} = \left[ m^0 E^0 - (\tilde{\underline{F}}_{42} \cdot \underline{U}_1 + \tilde{\underline{F}}_{13} \cdot \underline{U}_2 + \tilde{\underline{F}}_{24} \cdot \underline{U}_3 + \tilde{\underline{F}}_{31} \cdot \underline{U}_4 - E_t) \Delta t \right] / m^1 \quad (C33)$$

$$\tilde{P} = (\gamma - 1) \rho^1 \tilde{E} \quad (C34)$$

$$\tilde{\underline{F}}_{42} = \frac{1}{2}(P^0 - \tilde{P}) \cdot \underline{A}_{42} \quad (C35)$$

$$\tilde{\tilde{E}} = \tilde{E} - \left[ \Delta t (\tilde{\underline{F}}_{42} \cdot \underline{U}_1 + \tilde{\underline{F}}_{13} \cdot \underline{U}_2 + \tilde{\underline{F}}_{24} \cdot \underline{U}_3 + \tilde{\underline{F}}_{31} \cdot \underline{U}_4) \right] / m^1 \quad (C36)$$

$$P = (\gamma - 1) \rho^1 \tilde{\tilde{E}} \quad (C37)$$

$$\underline{F}_{42} = \frac{1}{2}(\sigma^0 + \sigma^1) \cdot \underline{A}_{42} \quad (C38)$$

$$E^1 = \left[ m^0 E^0 - (\underline{F}_{42} \cdot \underline{U}_1 + \underline{F}_{13} \cdot \underline{U}_2 + \underline{F}_{24} \cdot \underline{U}_3 + \underline{F}_{31} \cdot \underline{U}_4) \Delta t \right] / m^1 \quad (C39)$$

$$m_p^1 = \frac{1}{4}(m_a^1 + m_b^1 + m_c^1 + m_d^1) \quad (C40)$$

$$\begin{aligned}
\underline{M}_t = & \frac{1}{4} \left[ (\rho WA)_{42} + (\rho WA)_{12} + (\rho WA)_{54} + (\rho WA)_{61} \right] \cdot \frac{1}{2} (\underline{U}_4 + \underline{U}_1) \quad (C41) \\
& + \frac{1}{4} \left[ (\rho WA)_{12} + (\rho WA)_{89} + (\rho WA)_{61} + (\rho WA)_{78} \right] \cdot \frac{1}{2} (\underline{U}_1 + \underline{U}_8) \\
& + \frac{1}{4} \left[ (\rho WA)_{56} + (\rho WA)_{41} + (\rho WA)_{67} + (\rho WA)_{18} \right] \cdot \frac{1}{2} (\underline{U}_6 + \underline{U}_1) \\
& + \frac{1}{4} \left[ (\rho WA)_{41} + (\rho WA)_{32} + (\rho WA)_{18} + (\rho WA)_{29} \right] \cdot \frac{1}{2} (\underline{U}_1 + \underline{U}_2)
\end{aligned}$$

$$\underline{M}^1 = \underline{M}^0 + (\underline{F}_{42} + \underline{F}_{64} + \underline{F}_{86} + \underline{F}_{28} + \underline{M}_t) \Delta t \quad (C42)$$

$$\underline{U}^{\frac{1}{2}} = (2\underline{M}^1 / m_p^1) - \underline{U} \quad (C43)$$

$$H^1 = \frac{1}{2} m_p^1 (\underline{U}_1 \cdot \underline{U}_1) + \frac{1}{2} (m_a^1 E_a^1 + m_b^1 E_b^1 + m_c^1 E_c^1 + m_d^1 E_d^1) \quad (C44)$$

$$\underline{F}_{ad} = \sigma \cdot (\underline{R}_a - \underline{R}_d) \times \hat{k} \quad (C45)$$

$$\begin{aligned}
\dot{W} = & - \left[ \frac{1}{2} (\underline{U}_1 + \underline{U}_6) \cdot (\underline{F}_{bb} + \underline{F}_{bc}) + \frac{1}{2} (\underline{U}_1 + \underline{U}_8) \cdot (\underline{F}_{cc} + \underline{F}_{cd}) \right. \\
& \left. + \frac{1}{2} (\underline{U}_1 + \underline{U}_2) \cdot (\underline{F}_{dd} + \underline{F}_{da}) + \frac{1}{2} (\underline{U}_1 + \underline{U}_4) \cdot (\underline{F}_{aa} + \underline{F}_{ab}) \right] \quad (C46)
\end{aligned}$$

$$\begin{aligned}
H_E = & \frac{1}{4} \left[ (\rho WAE)_{43} + (\rho WAE)_{12} + (\rho WAE)_{59} + (\rho WAE)_{61} \right] \quad (C47) \\
& + \frac{1}{4} \left[ (\rho WAE)_{12} + (\rho WAE)_{89} + (\rho WAE)_{61} + (\rho WAE)_{78} \right] \\
& + \frac{1}{4} \left[ (\rho WAE)_{56} + (\rho WAE)_{41} + (\rho WAE)_{67} + (\rho WAE)_{18} \right] \\
& + \frac{1}{4} \left[ (\rho WAE)_{41} + (\rho WAE)_{32} + (\rho WAE)_{18} + (\rho WAE)_{29} \right]
\end{aligned}$$

$$\begin{aligned}
H_{KE} = & \frac{1}{16} \left[ (\rho WA)_{43} + (\rho WA)_{12} + (\rho WA)_{54} + (\rho WA)_{61} \right] (\underline{U}_4 + \underline{U}_1)^2 \quad (C48) \\
& + \frac{1}{16} \left[ (\rho WA)_{12} + (\rho WA)_{89} + (\rho WA)_{61} + (\rho WA)_{78} \right] (\underline{U}_1 + \underline{U}_8)^2 \\
& + \frac{1}{16} \left[ (\rho WA)_{56} + (\rho WA)_{41} + (\rho WA)_{67} + (\rho WA)_{18} \right] (\underline{U}_6 + \underline{U}_1)^2 \\
& + \frac{1}{16} \left[ (\rho WA)_{41} + (\rho WA)_{32} + (\rho WA)_{18} + (\rho WA)_{29} \right] (\underline{U}_1 + \underline{U}_2)^2
\end{aligned}$$



$$\dot{W} = - \left[ \frac{1}{2}(\underline{U}_1 + \underline{U}_6) \cdot (\underline{F}_{\underline{b}\underline{b}} + \underline{F}_{\underline{b}\underline{c}}) + \frac{1}{2}(\underline{U}_1 + \underline{U}_8) \cdot (\underline{F}_{\underline{c}\underline{c}} + \underline{F}_{\underline{c}\underline{d}}) \right. \\ \left. + \frac{1}{2}(\underline{U}_1 + \underline{U}_2) \cdot (\underline{F}_{\underline{d}\underline{d}} + \underline{F}_{\underline{d}\underline{a}}) + \frac{1}{2}(\underline{U}_1 + \underline{U}_4) \cdot (\underline{F}_{\underline{a}\underline{a}} + \underline{F}_{\underline{a}\underline{b}}) \right] \quad (C49)$$

$$H^1 = H^0 - \dot{W}\Delta t - (H_E + H_{KE}) \Delta t \quad (C50)$$

## APPENDIX D

### PARAMETRIC REPRESENTATION OF FUSELAGE CROSS SECTIONS

In this section the parameters which describe the fuselage cross sections are specified as functions of distance along the  $7\frac{1}{2}^\circ$  reference line (see figure 8) and the  $7\frac{1}{2}^\circ$  reference line is prescribed as a function of horizontal station. The cross sections taken were perpendicular to the  $7\frac{1}{2}^\circ$  reference line (i.e. z-axis, figure 8). The parameters of each cross section was determined from geometrical data which were taken from the design blueprint of the fuselage geometry.

A schematic representation of the fuselage cross section normal and the  $7\frac{1}{2}^\circ$  reference line is presented in figure 9. In figure 9 the parameters which describe the cross section are indicated. These parameters are defined as follows:

- $(A_1(z), B_1(z))$ , coordinates of the center of the smaller circular arc in the fuselage periphery
- $R_1(z)$ , radius of the smaller circle of the fuselage periphery
- $(A_2(z), B_2(z))$ , coordinates of the center of the larger circular arc in the fuselage periphery
- $R_2(z)$ , radius of the larger arc
- $(A_5(z), B_5(z))$ , coordinates of the center of the arc of the canopy
- $R_3(z)$ , canopy radius

In the case being considered,  $B_2(z) = A_2(2) = A_5(2) = 0$ ,  $R_2(z) - R_1(z) = A_1(z)$  (Since the shape supplied has flat sides and bottom), and  $R_2(z) - B_5(z) \leq R_3(z)$ . Furthermore,  $B_5(z) = R_2(z)$  and  $R_3(z)$  equal zero for  $z$  less than  $z_2$ , where  $z_2 (=10.88")$  defines the distance along the  $7\frac{1}{2}^\circ$  reference line at which the canopy first appears. The fuselage cross-section is circular to  $z_1 = 9.44$  inches and asymmetric between  $z_1$  and  $z_2$ . It proved convenient to define these parameters by another set of functions from a distance of  $z_3 = 15.05$  inches onward. The equations for the above parameters considered units of inches and are as follows:

(i) Radius of smaller circle of fuselage periphery

$$\text{For } 0 \leq z \leq 30.68, \quad R_1(z) = \sum_{J=1}^{12} a_J^{R_1} z^J$$

$$\begin{array}{ll} \text{where } a_1^{R_1} = (1.7873231 \times 10^{-1}) & a_7^{R_1} = (-2.1016895 \times 10^{-6}) \\ a_2^{R_1} = (7.0559487 \times 10^{-2}) & a_8^{R_1} = (5.1489881 \times 10^{-8}) \\ a_3^{R_1} = (-3.2209788 \times 10^{-2}) & a_9^{R_1} = (-6.6633139 \times 10^{-10}) \\ a_4^{R_1} = (6.6039801 \times 10^{-2}) & a_{10}^{R_1} = (2.0697609 \times 10^{-12}) \\ a_5^{R_1} = (-7.5565592 \times 10^{-4}) & a_{11}^{R_1} = (4.7027051 \times 10^{-14}) \\ a_6^{R_1} = (5.1130544 \times 10^{-5}) & a_{12}^{R_1} = (-4.0954467 \times 10^{-16}) \end{array}$$

(ii) Radius of larger arc

$$\text{For } 0 \leq z \leq z_3, \quad R_2(z) = \sum_{J=1}^{12} a_J^{R_2} z^J$$

$$\begin{array}{ll} \text{where } a_1^{R_2} = (3.4725590 \times 10^{-1}) & a_7^{R_2} = (3.7708718 \times 10^{-6}) \\ a_2^{R_2} = (-1.0362533 \times 10^{-1}) & a_8^{R_2} = (-1.3236585 \times 10^{-7}) \\ a_3^{R_2} = (3.6798959 \times 10^{-2}) & a_9^{R_2} = (3.0861620 \times 10^{-9}) \\ a_4^{R_2} = (-7.4940700 \times 10^{-3}) & a_{10}^{R_2} = (-4.5831105 \times 10^{-11}) \\ a_5^{R_2} = (9.1822566 \times 10^{-4}) & a_{11}^{R_2} = (3.9237683 \times 10^{-13}) \\ a_6^{R_2} = (-7.2186739 \times 10^{-5}) & a_{12}^{R_2} = (-1.4741591 \times 10^{-15}) \end{array}$$

$$\text{For } z_3 \leq z \leq 21, \quad R_2(z) = \sum_{J=1}^3 a_J^{R_2} z^J$$

$$\text{where } a_1^{R_2} = (.1686363)$$

$$a_2^{R_2} = (1.722509 \times 10^{-3})$$

$$a_3^{R_2} = (-2.142585 \times 10^{-4})$$

(iii) Ordinate of center of smaller circle

$$\text{For } 0 \leq z \leq z_3, \quad B_1(z) = \sum_{J=1}^{11} a_J^{B_1} z^J$$

$$\text{where } a_1^{B_1} = (-1.5159906 \times 10^{-1}) \quad a_7^{B_1} = (-4.1445421 \times 10^{-6})$$

$$a_2^{B_1} = (1.5449971 \times 10^{-1}) \quad a_8^{B_1} = (1.1565654 \times 10^{-7})$$

$$a_3^{B_1} = (-5.9976730 \times 10^{-2}) \quad a_9^{B_1} = (-1.9920283 \times 10^{-9})$$

$$a_4^{B_1} = (1.1907145 \times 10^{-2}) \quad a_{10}^{B_1} = (1.9332318 \times 10^{-11})$$

$$a_5^{B_1} = (-1.3574646 \times 10^{-3}) \quad a_{11}^{B_1} = (-8.0938014 \times 10^{-14})$$

$$a_6^{B_1} = (9.4391044 \times 10^{-5})$$

$$\text{For } z_3 < z \leq 21, \quad B_1(z) = \sum_{J=1}^3 a_J^{B_1} z^J$$

$$\text{where } a_1^{B_1} = (.2135555)$$

$$a_2^{B_1} = (-2.376651 \times 10^{-2})$$

$$a_3^{B_1} = (4.465725 \times 10^{-3})$$



## APPENDIX E

### DATA REDUCTION COMPUTER CODE

A data reduction computer code has been developed to reduce the flow field data of Problems 211.0 and 212.0 to meaningful parameters. The function of the code is to compute the Mach number, flow angularity, total pressure recovery, and pressure coefficient in cross section planes normal to the body axis. These parameters are to be calculated from the more fundamental AFTON 2PE numerical solution data (i.e., pressure, density, velocity, etc.).

The data reduction code, called "AMSD", performs three functions. First, it selects and reads a dump (i.e., the flow field properties at a particular axial station) from the AFTON 2PE dump tape. Then it calculates the specific internal energy (E), density ( $\rho$ ), pressure (p), and the velocity component (w) in the axial direction at each of the mesh points. The specific internal energy, density, and pressure are zone centered in AFTON 2PE, so the mass and internal energy of the momentum zones must first be evaluated in order to determine the specific internal energy and density at a mesh point (ref.10). The pressure is then determined from the perfect gas law. Based on these parameters and the velocity components u and v in the plane of calculation, the velocity component w in the axial direction can be evaluated from the Bernoulli equation as follows:

$$w = U_{\infty} \cos \alpha + \left[ \frac{K - \left( \frac{\gamma}{\gamma - 1} \frac{P}{\rho} + \frac{v^2 + u^2}{2} \right)}{U_{\infty} \cos \alpha} \right] \quad (E1)$$

where

- $U_{\infty}$  , free stream velocity
- $\alpha$  , angle of attack of free stream flow with respect to body axis
- $\gamma$  , ratio of specific heats [ $\gamma = (C_p/C_v)$ ]
- P , pressure
- $\rho$  , density

$$K = \frac{a_\infty^2}{\gamma-1} \left[ 1 + \frac{\gamma-1}{2} \sin^2 \alpha M_\infty^2 \right] \quad (E2)$$

where:

$a_\infty$ , free stream sound speed

$M_\infty$ , free stream Mach number

Equation (E1) is valid for a weak shock and where viscous effects are small. In the ogive-cylinder problem at an axial station of .502 cylinder diameters and at a point on the dividing streamline 1.36 cylinder radii upstream of the cylinder's center, the ratio of the local stagnation pressure (P) to the free stream stagnation pressure ( $P_{s\infty}$ ) is .92. For the fuselage problem total pressure recovery  $P_s/P_{s\infty}$  varies from .90 to 1.00. It is shown below that the entropy change is directly related to the total pressure recovery; hence, the entropy change is small in both problems and the weak shock approximation is valid.

Based on the properties just cited, the required parameters are determined by the AMSD computer code at each of the mesh points, from the following relations:

$$M = \frac{[w^2 + u^2 + v^2]^{\frac{1}{2}}}{c} \quad (E3)$$

$$c = [\gamma(\gamma-1) E]^{\frac{1}{2}} \quad (E4)$$

$$\frac{P_s}{P_{s\infty}} = \exp \left\{ -\frac{(S-S_\infty)}{C_p} \left( \frac{\gamma}{\gamma-1} \right) \right\} \quad (E5)$$

where:

$$\frac{S-S_\infty}{C_p} = \log_e \left\{ \left( \frac{h}{h_\infty} \right) / \left( \frac{P}{P_\infty} \right)^{\frac{\gamma-1}{\gamma}} \right\} \quad (E6)$$

$$h = E + \frac{P}{\rho} \quad (E7)$$

$$h_\infty = E_\infty + \frac{P_\infty}{\rho_\infty} \quad (E8)$$

and finally the pressure coefficient is evaluated from

$$C_p = \frac{P - P_\infty}{\frac{1}{2} \rho_\infty U_\infty^2} \quad (E9)$$

where:

- C, local sound speed
- $C_p$ , local pressure coefficient
- h, local enthalpy
- S, entropy
- M, local Mach number

Subscript infinity near any property refers to free stream conditions.

The local angle of attack of the flow,  $\alpha_e$ , and the local angle of side-slip of the flow,  $\beta$ , are measured in the coordinate system consisting of the horizontal reference line, the normal line to it in the plane of symmetry of the body, and the coordinate normal to both lines, i.e.,  $x'$ ,  $y'$ ,  $z'$  indicated in figure 9. On this basis  $\alpha_e$  and  $\beta$  are defined as follows:

$$\alpha_e = \tan^{-1} \left( \frac{U_y}{U_z} \right) \quad (E10)$$

$$\beta = \tan^{-1} \left( \frac{U_x}{U_z} \right) \quad (E11)$$

where:

$$U_x = u$$

$$U_y = v \cos \theta + w \sin \theta$$

$$U_z = -v \sin \theta + w \cos \theta$$

$$\theta = \tan^{-1} B'_2(z')$$

$$B'_2(z') = \text{local slope of central axis with respect to horizontal reference line}$$

The pitot pressure,  $P_p$ , corresponds to the stagnation pressure measured by a probe whose axis is placed parallel to the local flow direction. An approximation of the actual pitot pressure can be obtained by causing the local velocity vector to go through a normal shock. The relation is as follows:

$$\frac{P_p}{P_{s\infty}} = \frac{\left[ \frac{(\gamma+1)M^2}{(\gamma-1)M^2+2.0} \right]^{\frac{\gamma}{\gamma-1}} \left( \frac{P_s}{P_{s\infty}} \right)}{\left[ 1 + \frac{2\gamma(M^2-1)}{(\gamma+1)} \right] \frac{1}{\gamma-1}} \quad (E12)$$

## REFERENCES

1. Gallo, W. F.; and Rakich, C. V.: Investigation of Methods for Predicting Flow in the Shock Layer Over Bodies at Small Angles of Attack. NASA TN D-3926, 1967.
2. Van Dyke, M.D.: A Study of Hypersonic Small-Disturbance Theory. NACA Rep. 1194, 1954.
3. Hayes, W.D.: On Hypersonic Similitude. Quarterly Appl. Math., vol. 5, 1947, pp. 105-106.
4. Trulio, J.G.; and Trigger, K.: Numerical Solution of the One-Dimensional Hydrodynamic Equations. UCRL 6267, 1961.
5. Trulio, J.G.; and Trigger, K.: Numerical Solution of the One-Dimensional Hydrodynamic Equations in an Arbitrary Time-Dependent Coordinate System. UCRL 6522, 1961.
6. Trulio, J.G.: The Strip Code and the Jetting of Gas Between Plates, Methods in Computational Physics, Edited by B. Alder, S. Fernbach, M. Rotenberg, vol. 3, Academic Press, New York, p. 69, 1964.
7. Lees, L.; and Reeves, B.L.: Laminar Near Wake of Blunt Bodies in Hypersonic Flow. AIAA J., vol. 3, no. 11, 1965, pp. 2061-2074.
8. von Neumann, J.; and Richtmyer, R.D.: A Method for the Numerical Calculation of Hydrodynamic Shocks. J. Appl. Phys., vol. 21, no. 3, March 1950, p. 232.
9. Richtmyer, R.D.: Difference Methods for Initial Value Problems. Wiley (Interscience), New York, 1957.
10. Trulio, J.G.: Studies of Finite Difference Equations for Continuum Mechanics. WL-TDR-64-72, 1964.
11. Trulio, J.: Theory and Structure of the AFTON Codes. Tech. Rep. AFWL TR-66-19, 1966.
12. Walitt, L.: Numerical Studies of Supersonic Near Wakes. Ph.D. Thesis, Univ. of California, Los Angeles, 1969.
13. Trulio, J.G.; Niles, W.; and Carr, W.: Calculations of Two-Dimensional Turbulent Flow Fields. NASA CR-430, 1966.

#### REFERENCES

14. Jorgensen, L. H.; and Perkins, E.W.: Investigation of Some Wake Vortex Characteristics of an Inclined Ogive-Cylinder Body at Mach 1.98 NACA RM A55E31, 1955.
15. Schlichting, H.: Boundary Layer Theory. McGraw-Hill Book Co., Inc., 1955, p. 19.
16. Liepmann, H. W.; and Roshko, A.: Elements of Gas Dynamics. John Wiley and Sons, Inc., 1962, pp. 239-247.

# FLOW FIELD IN FUSELAGE CROSS SECTION PLANE

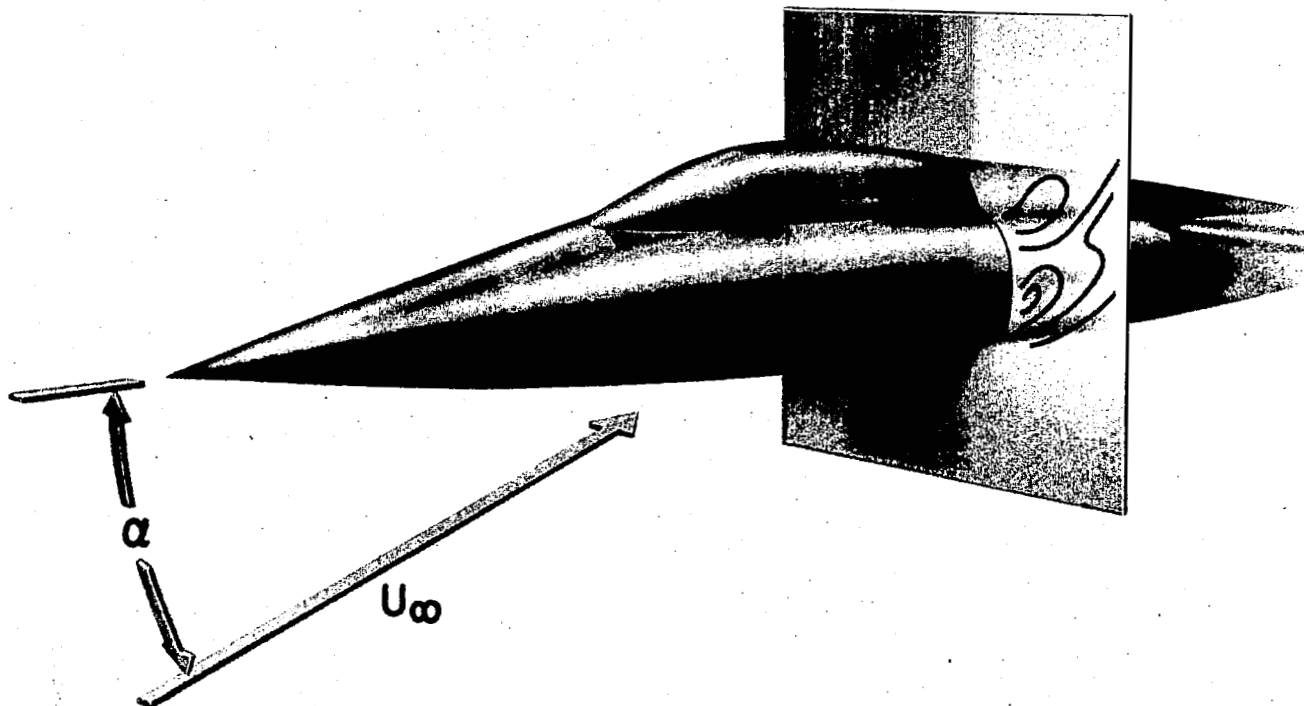


FIGURE 1

# APPLICATION OF THE EQUIVALENCE PRINCIPLE TO AN AXISYMMETRIC BODY

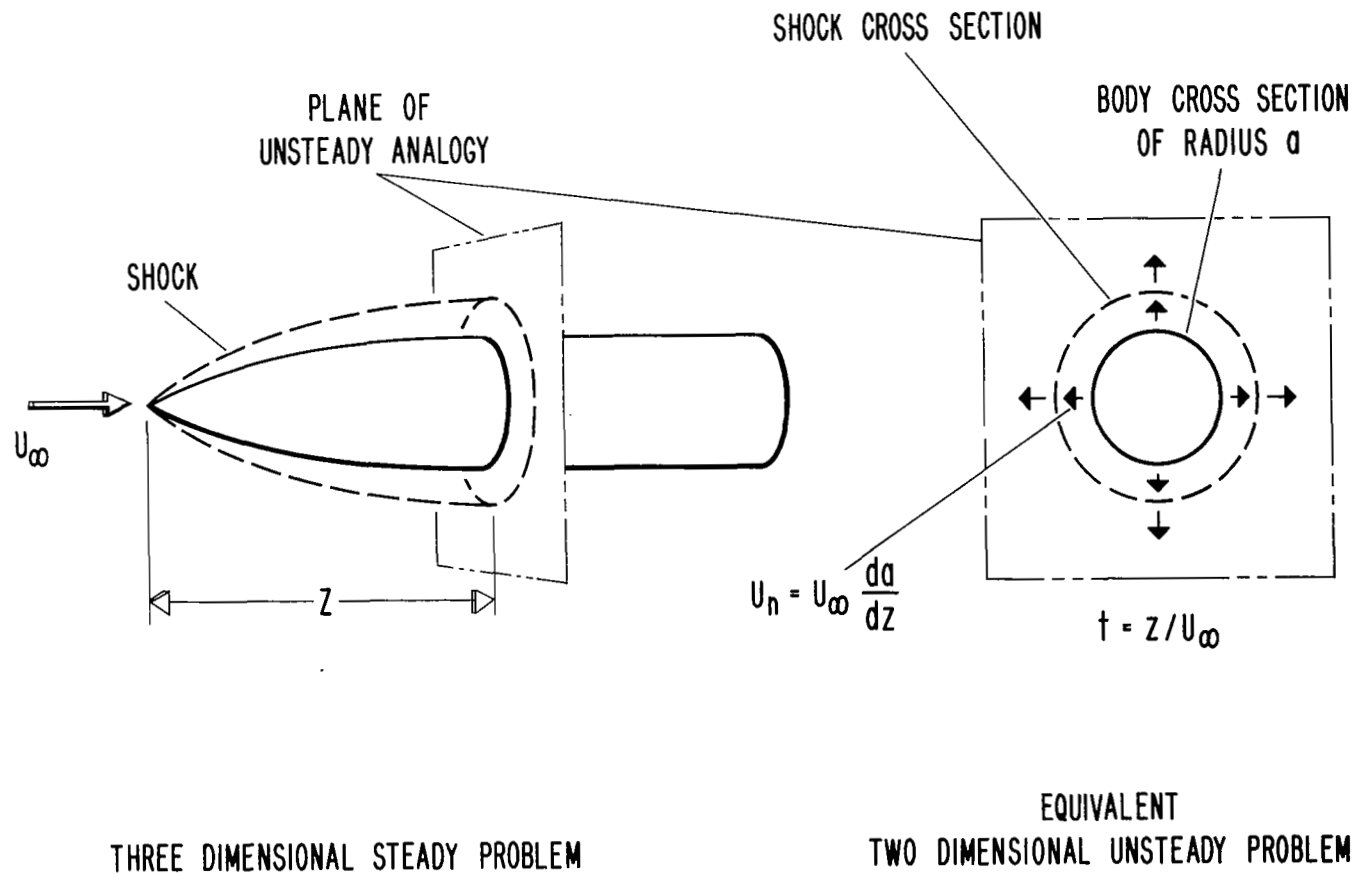


FIGURE 2

# FLOW FIELD ABOUT AN AXISYMMETRIC BODY AT ANGLE OF ATTACK

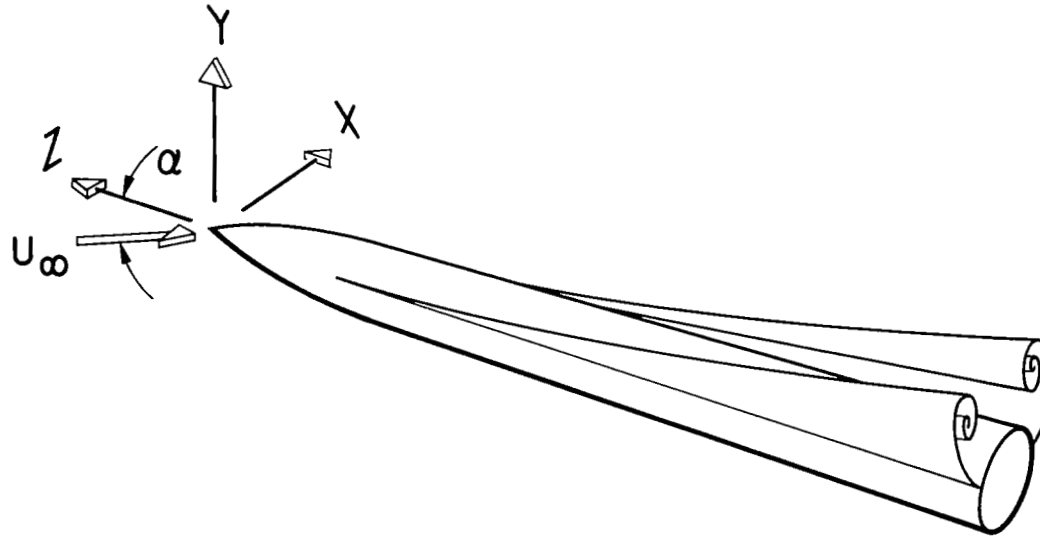


FIGURE 3



# FLOW REGIONS ABOUT A BODY MOVING AT SUPERSONIC VELOCITY

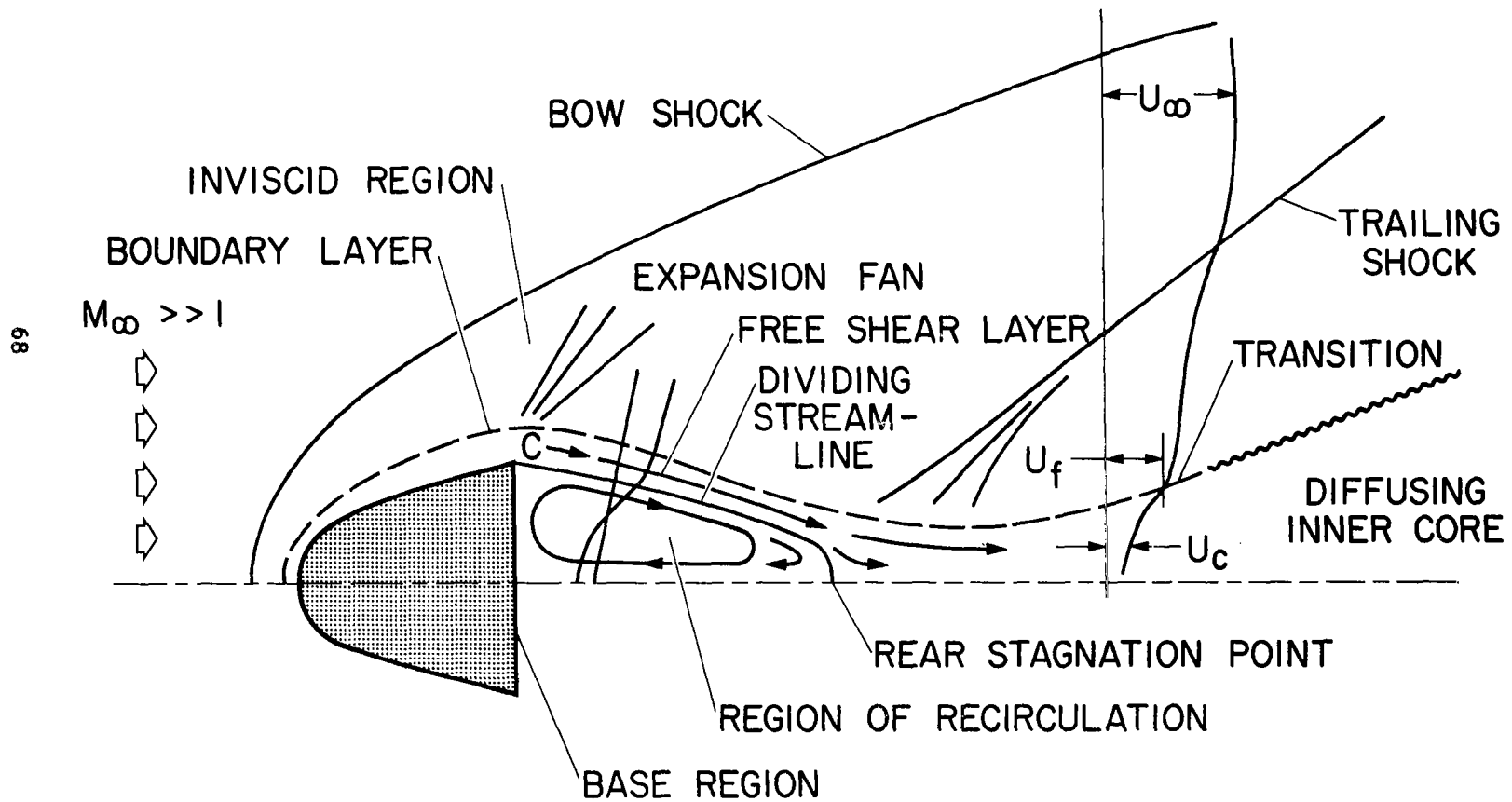
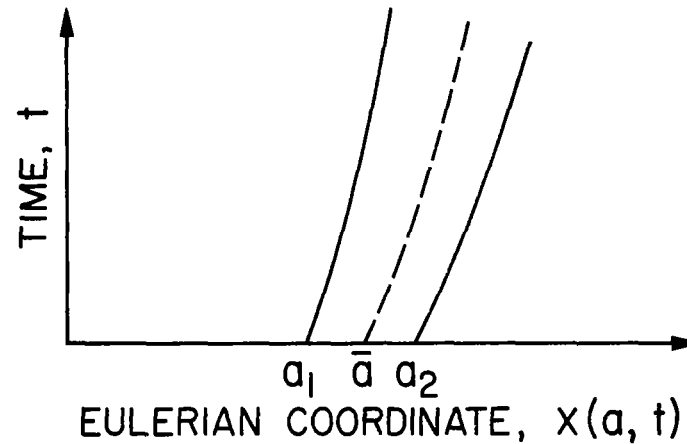


FIGURE 4

# ONE-DIMENSIONAL, TIME-DEPENDENT MOTION IN LAGRANGIAN COORDINATES

## PARTICLE TRAJECTORIES IN A LAGRANGIAN COORDINATE SYSTEM



## THERMODYNAMIC AND MOMENTUM ZONES FOR ONE-DIMENSIONAL TIME-DEPENDENT MOTION

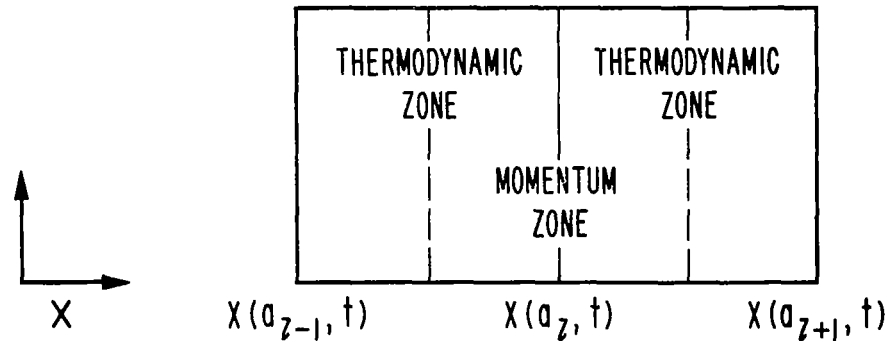


FIGURE 5

# SCHEMATIC DIAGRAM OF A FINITE DIFFERENCE MESH

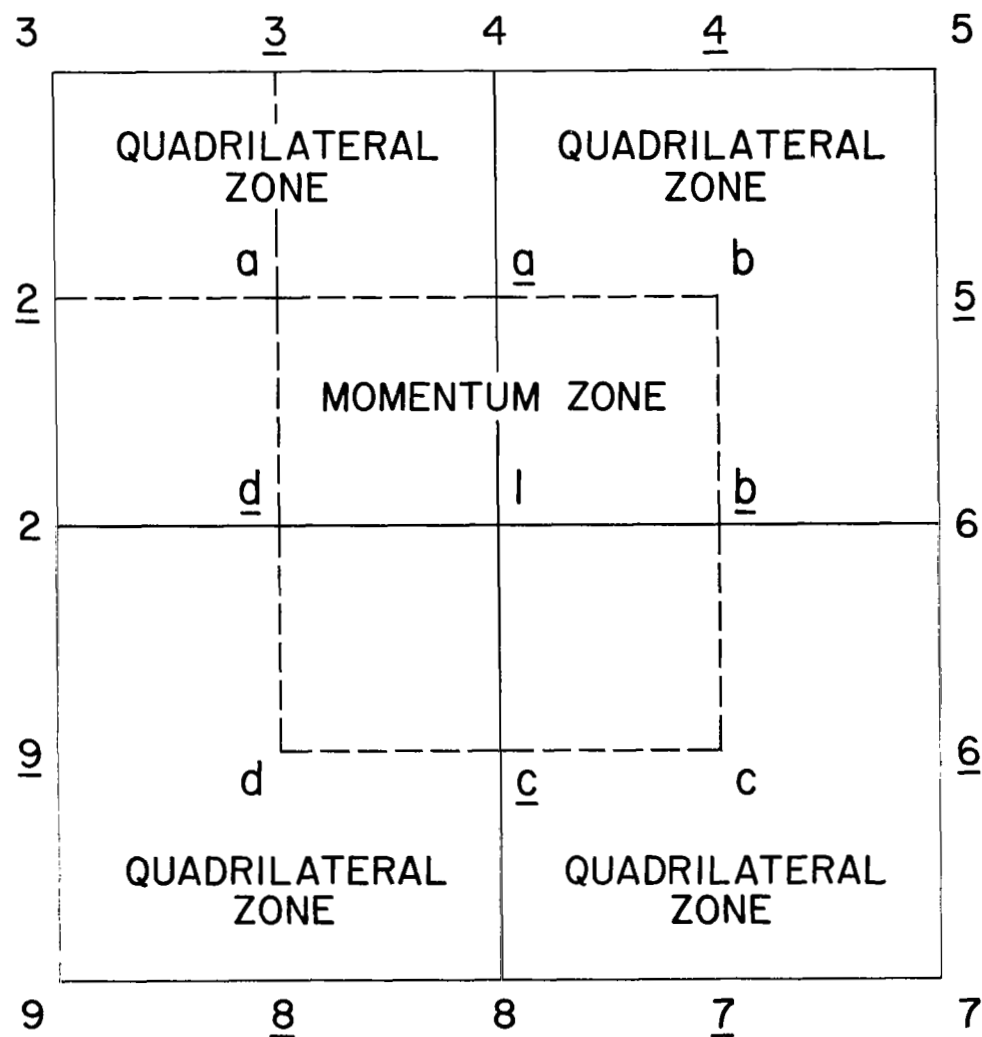


FIGURE 6

# OGIVE-CYLINDER BODY GEOMETRY

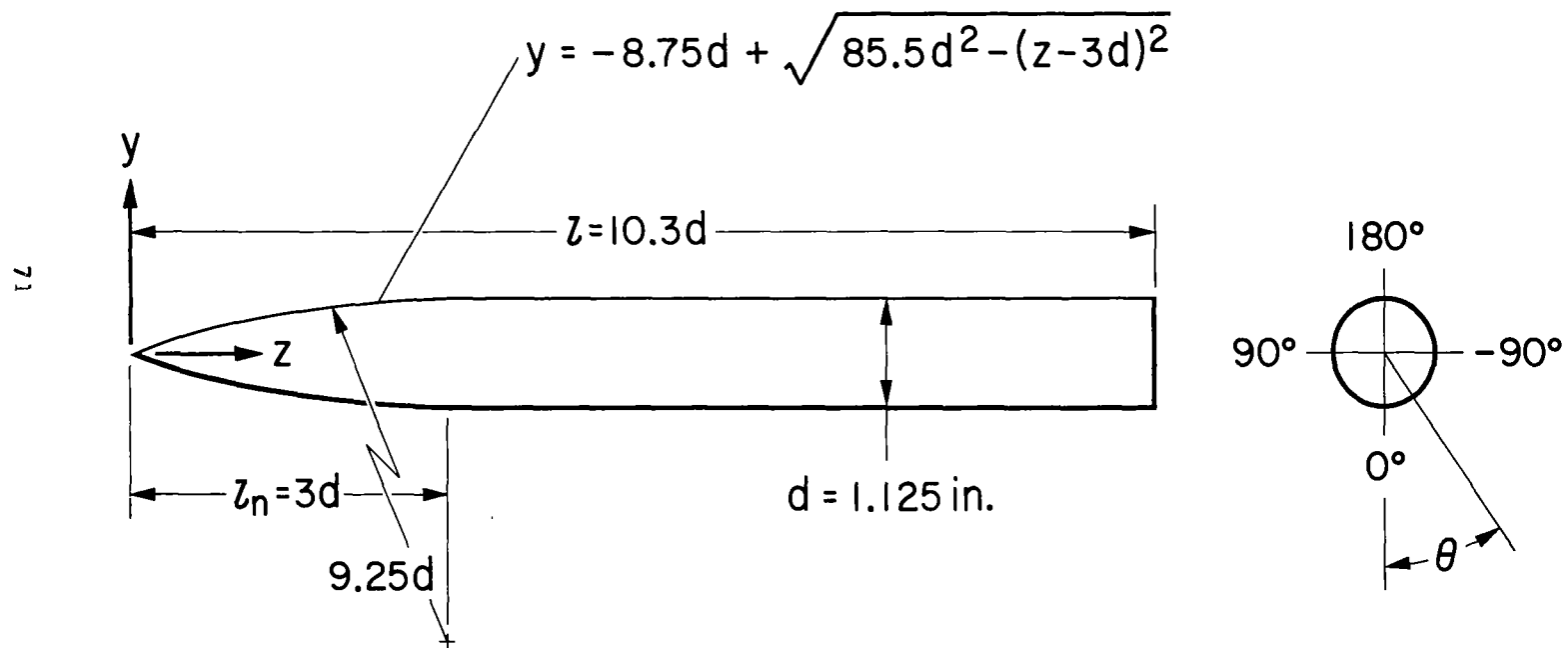


FIGURE 7

# SCHEMATIC OF FUSELAGE CONFIGURATION

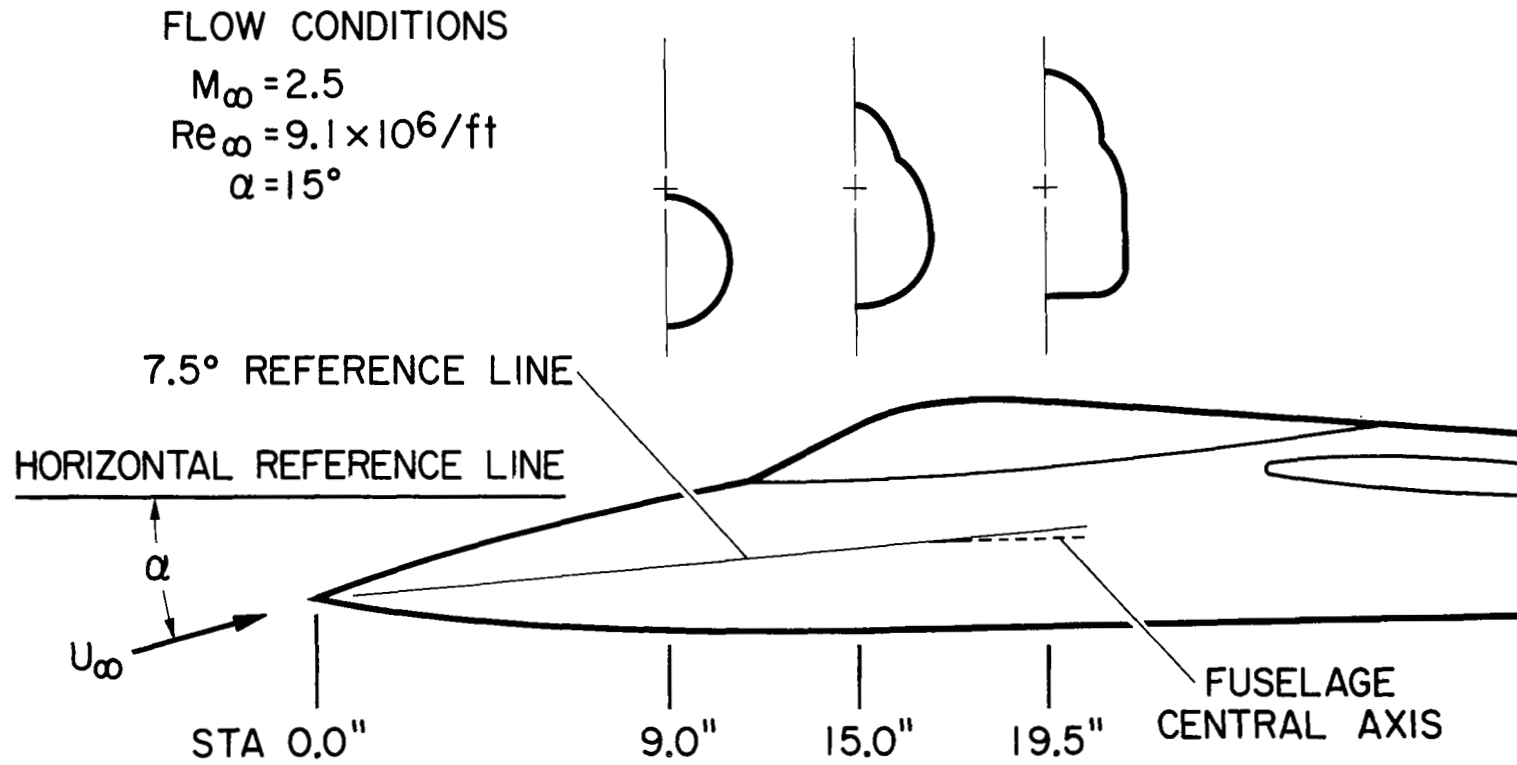


FIGURE 8

# DEFINITION OF FUSELAGE CROSS-SECTIONAL PARAMETERS

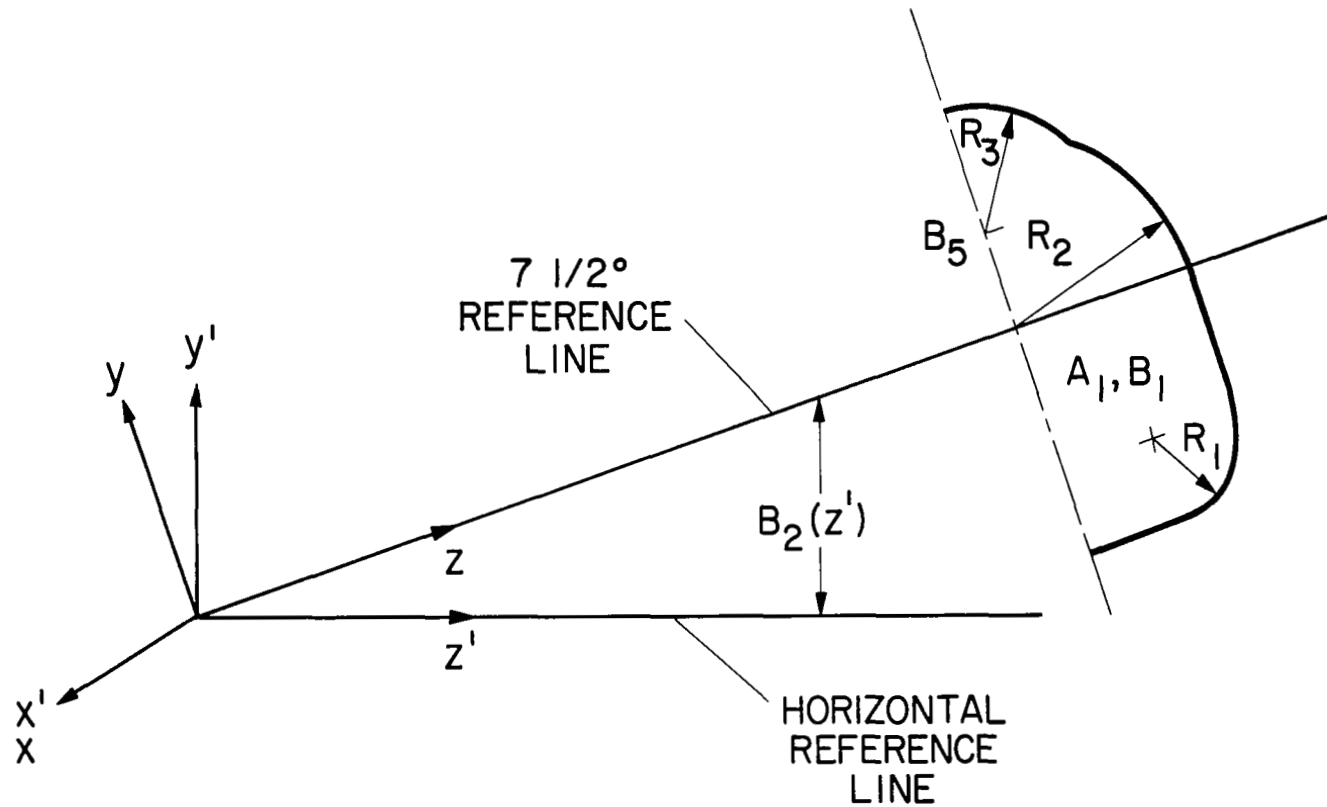


FIGURE 9

FINITE DIFFERENCE MESH FOR OGIVE-CYLINDER  
RADIUS 0.01 ft

CROSS FLOW →

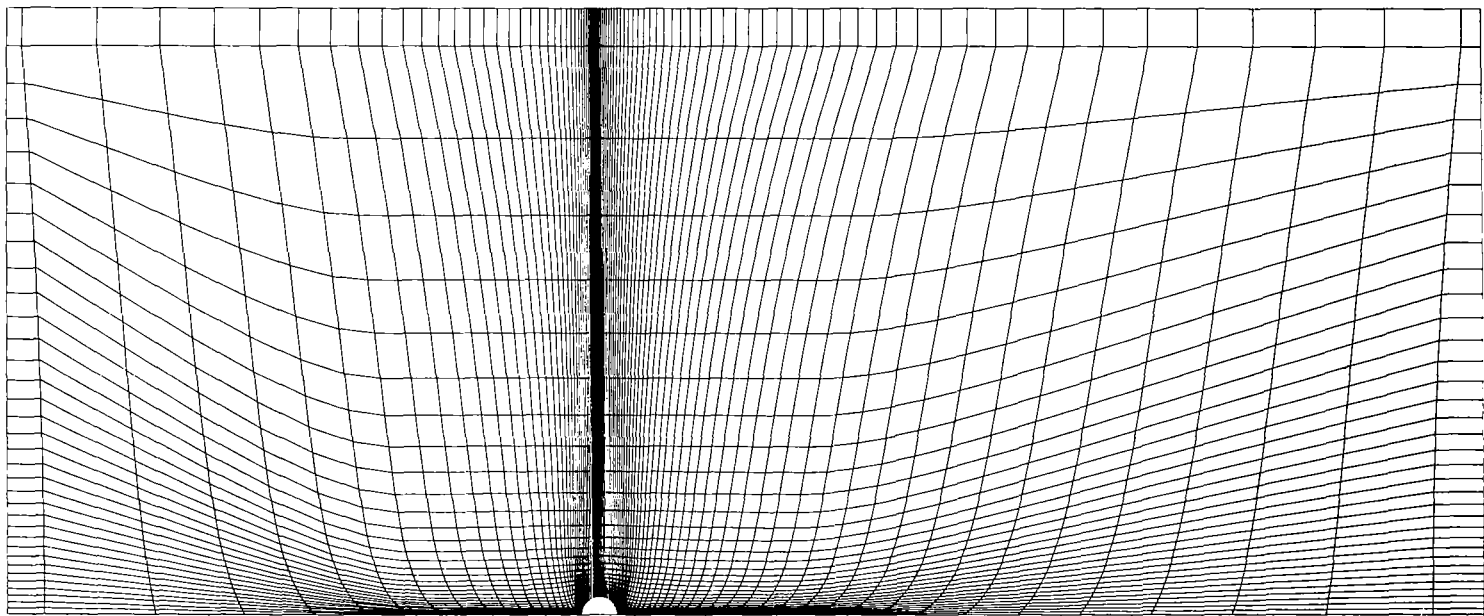


FIGURE 10

FINITE DIFFERENCE MESH FOR OGIVE-CYLINDER  
RADIUS 0.046875 ft

CROSS FLOW →

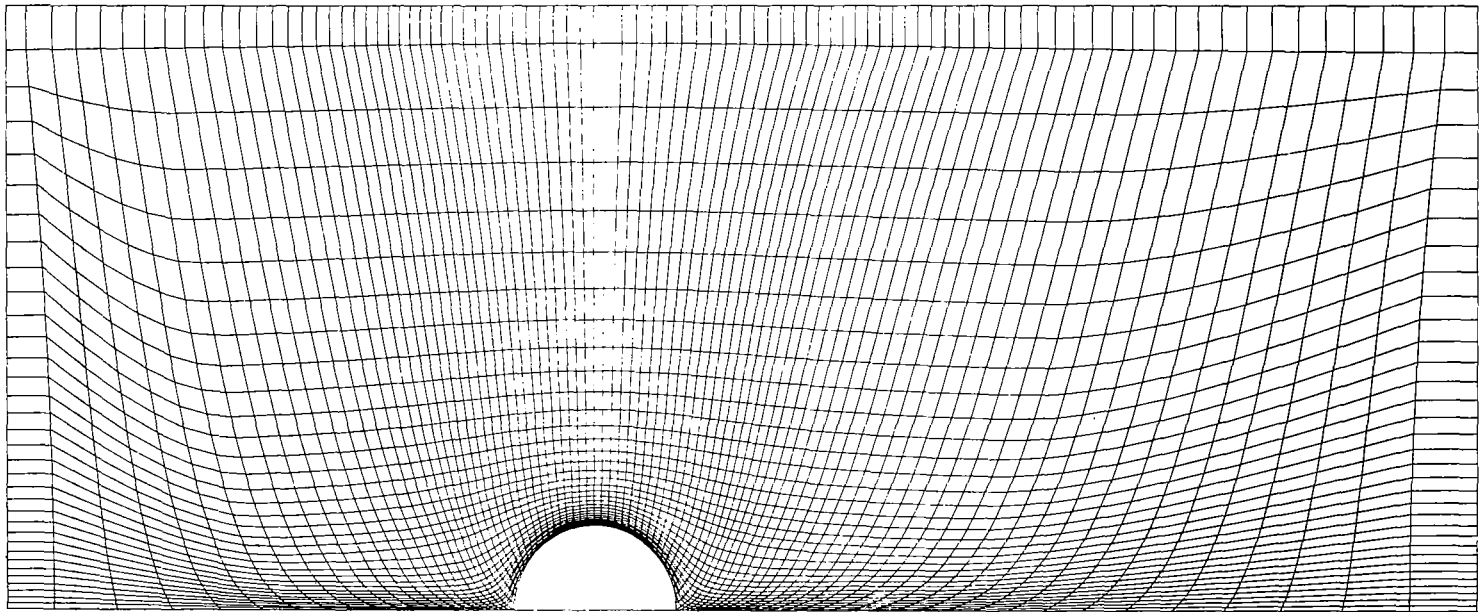


FIGURE 11



# FINITE DIFFERENCE MESH AT STA 7.0

CROSS FLOW →

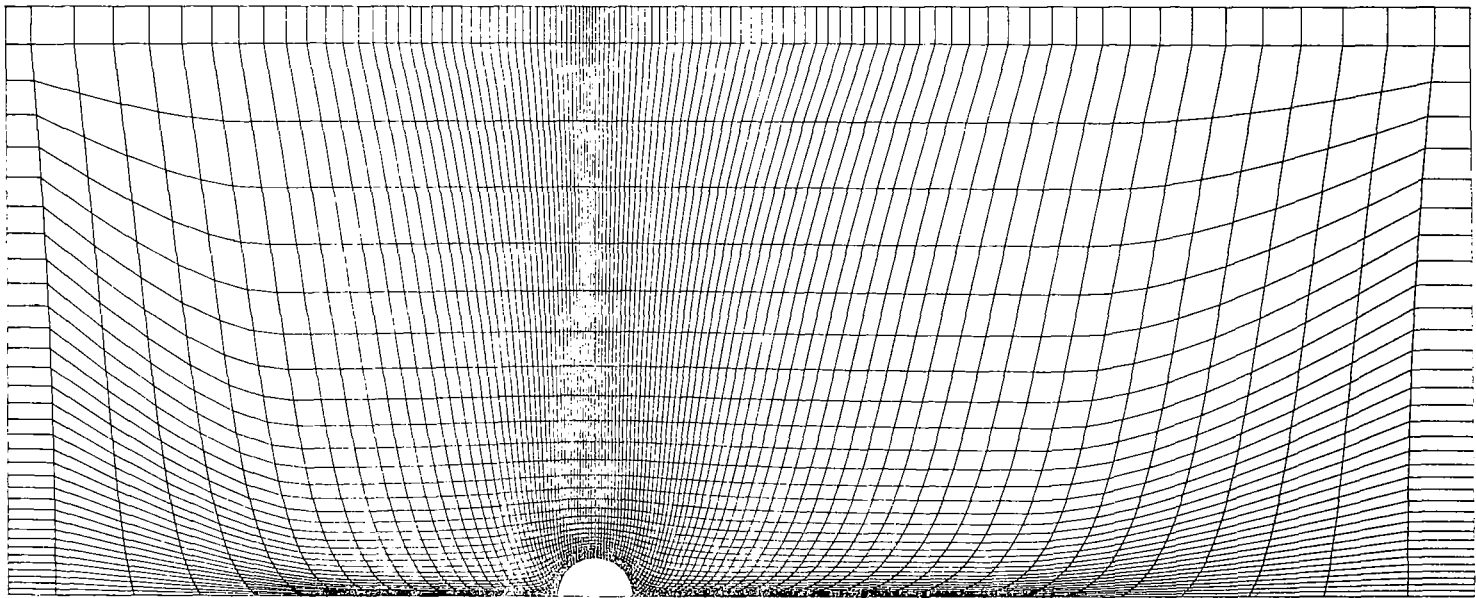


FIGURE 12

# FINITE DIFFERENCE MESH AT STA 25.0

CROSS FLOW →

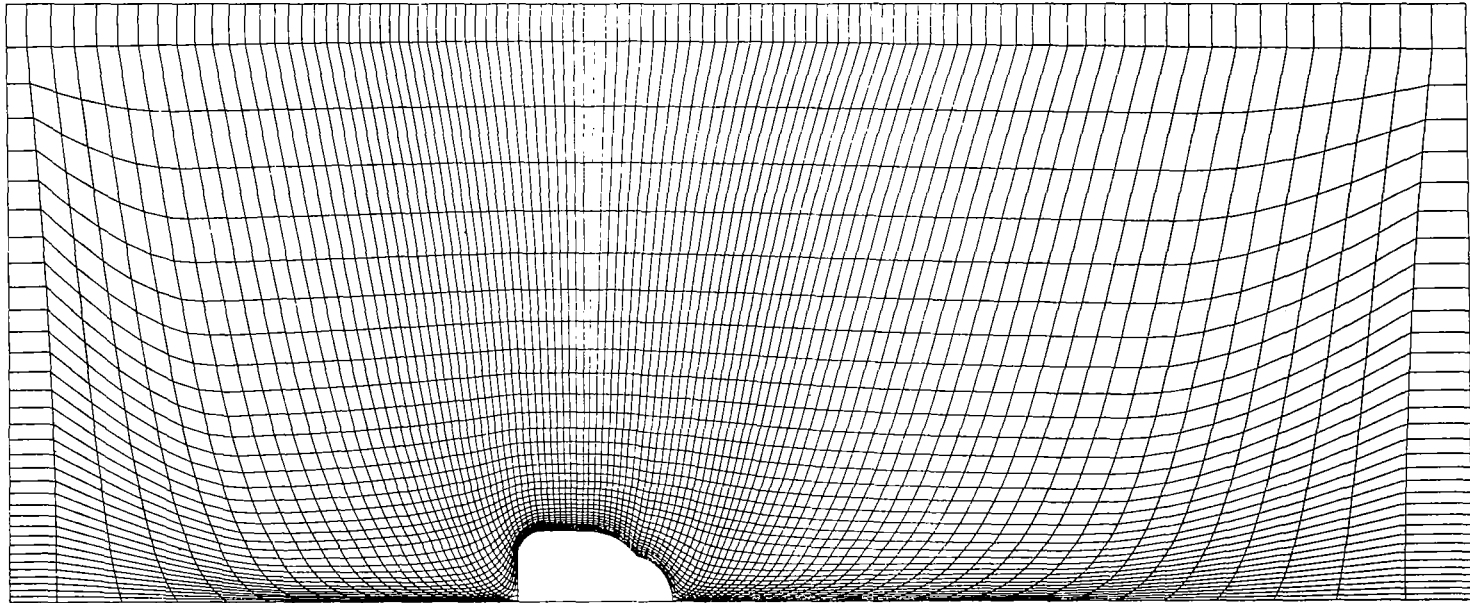


FIGURE 13

# VELOCITY VECTOR PLOT OF FLOW FIELD

0.502 MAX BODY DIAMETERS FROM NOSE

RADIUS 0.0145 ft

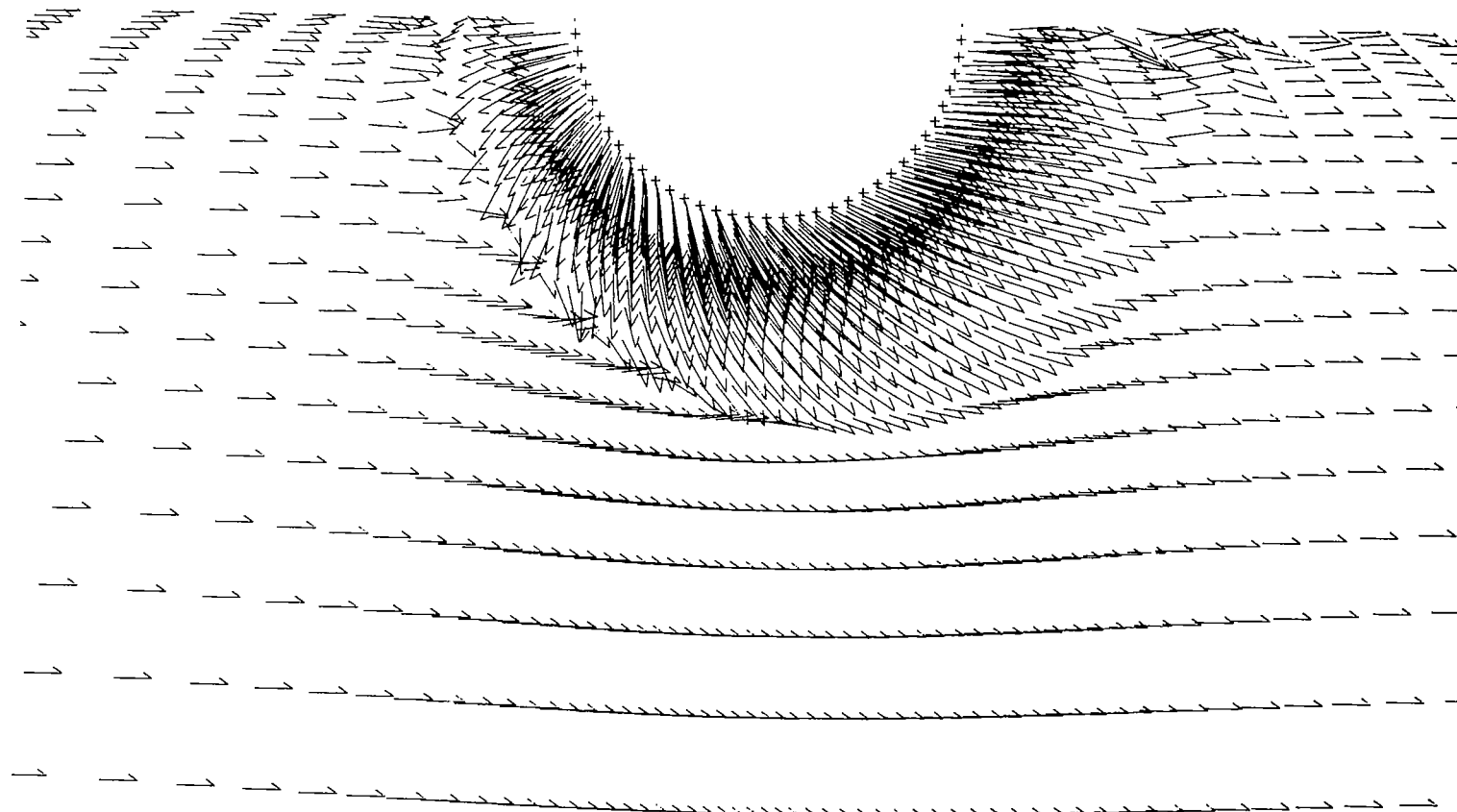


FIGURE 14

# VELOCITY VECTOR PLOT OF FLOW FIELD

2.99 MAX BODY DIAMETERS FROM NOSE

RADIUS 0.046875 ft

79

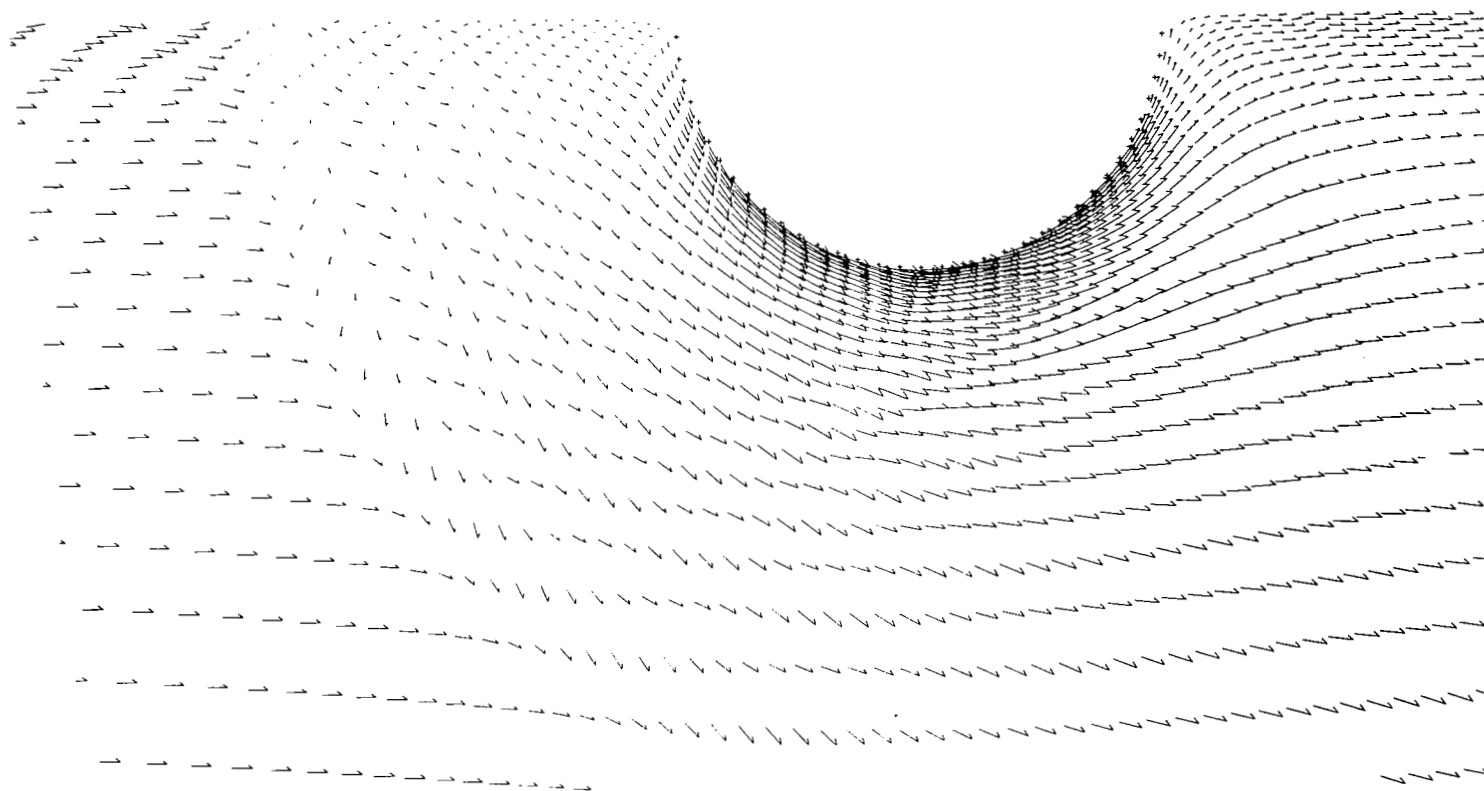


FIGURE 15

# VELOCITY VECTOR PLOT OF FLOW FIELD

4.92 MAX BODY DIAMETERS FROM NOSE

RADIUS 0.046875ft

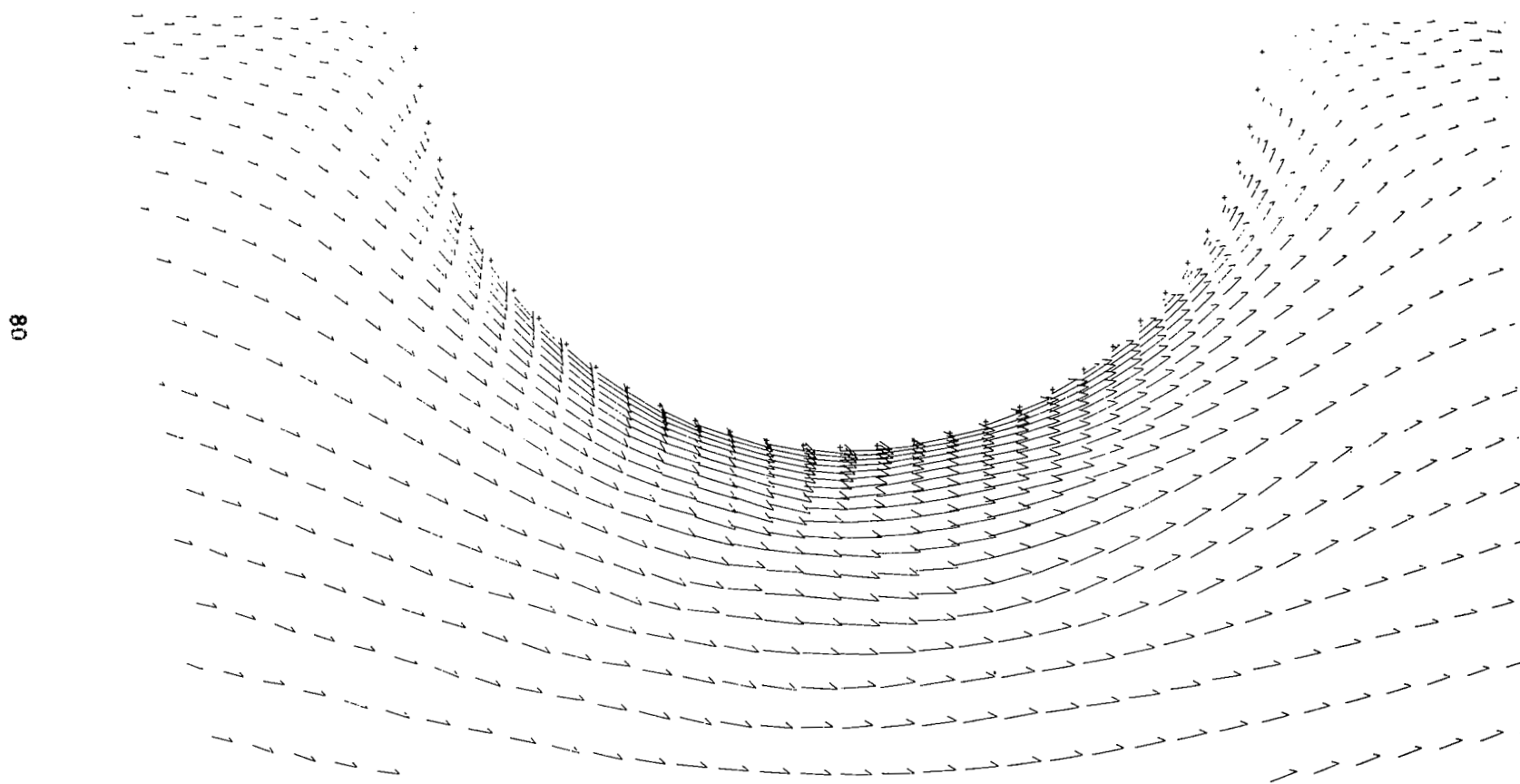


FIGURE 16

VELOCITY VECTOR PLOT OF FLOW FIELD  
8.35 MAX BODY DIAMETERS FROM NOSE

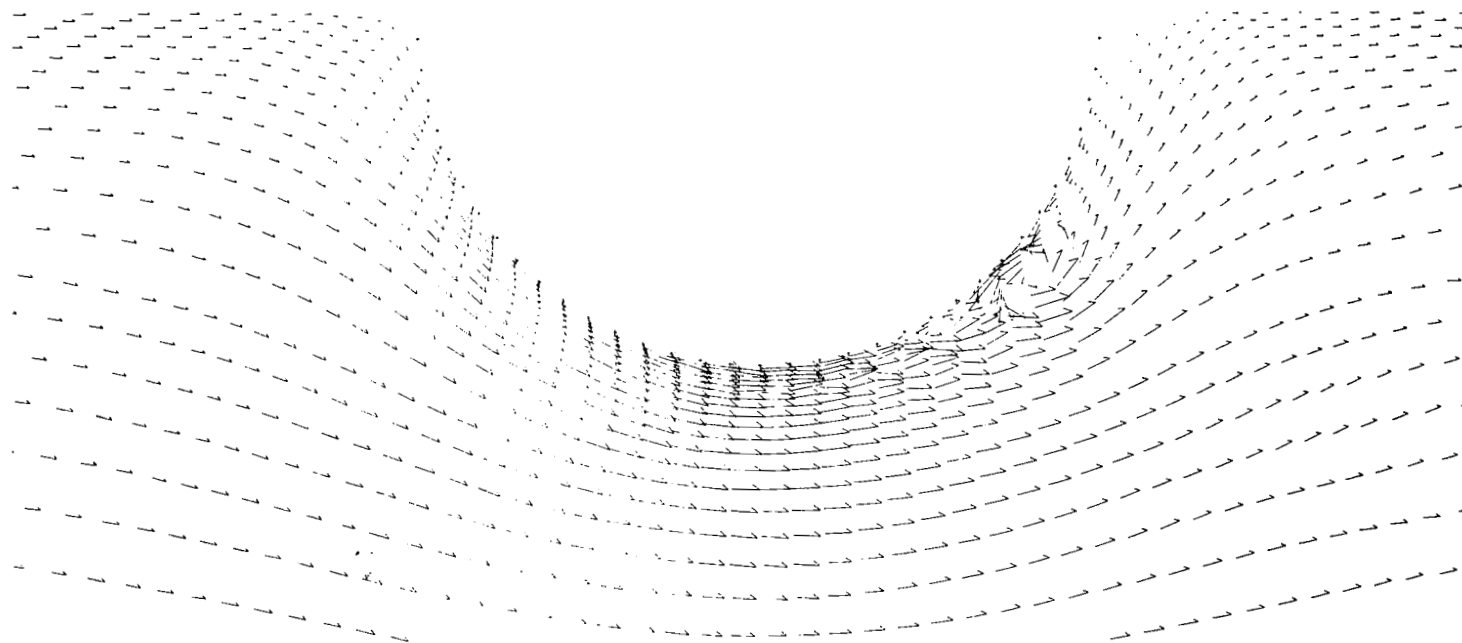


FIGURE 17

# OGIVE-CYLINDER SURFACE PRESSURE DISTRIBUTION

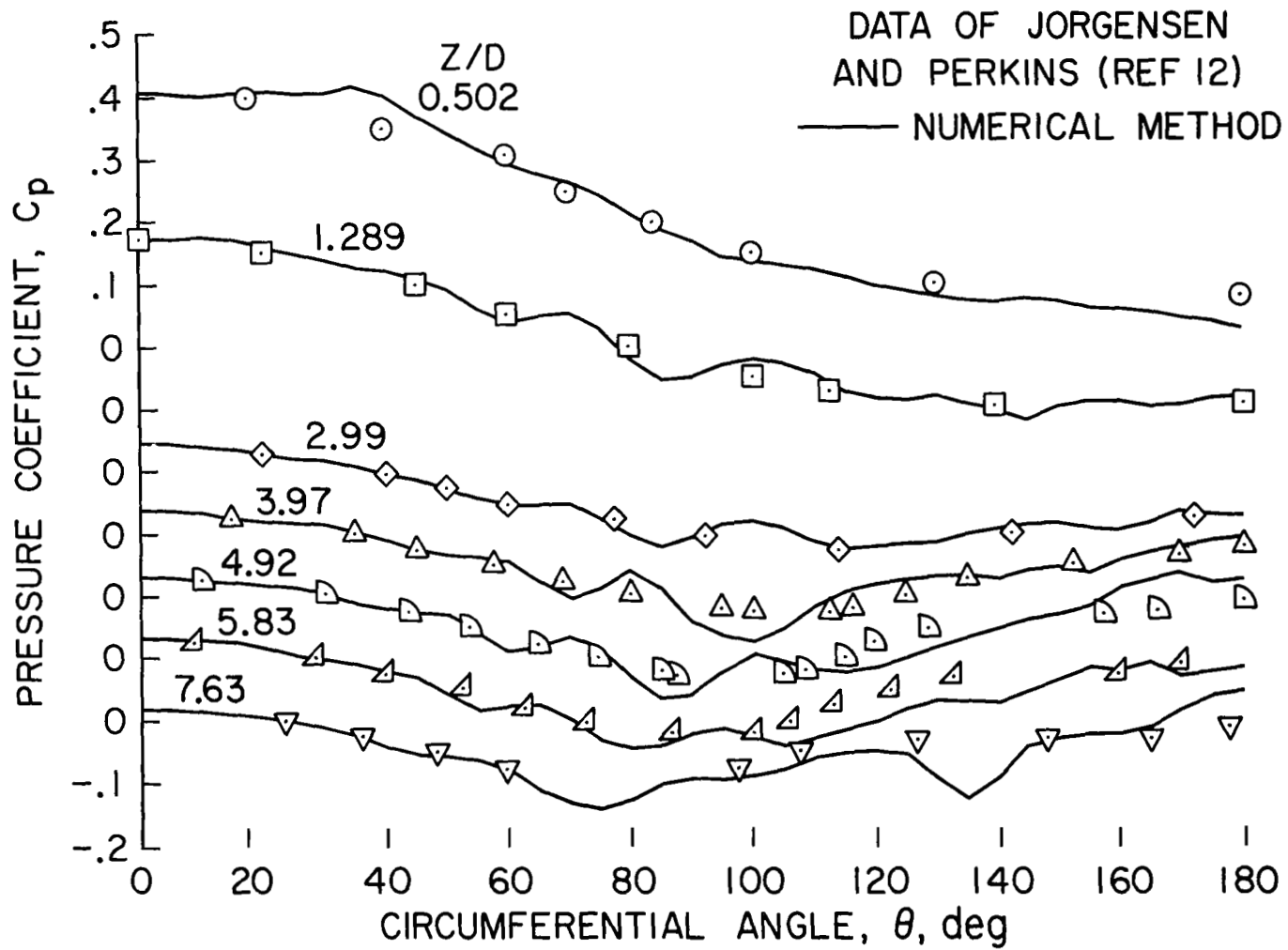


FIGURE 18

# TRAJECTORIES OF SEPARATION AND VORTEX CENTER POINTS

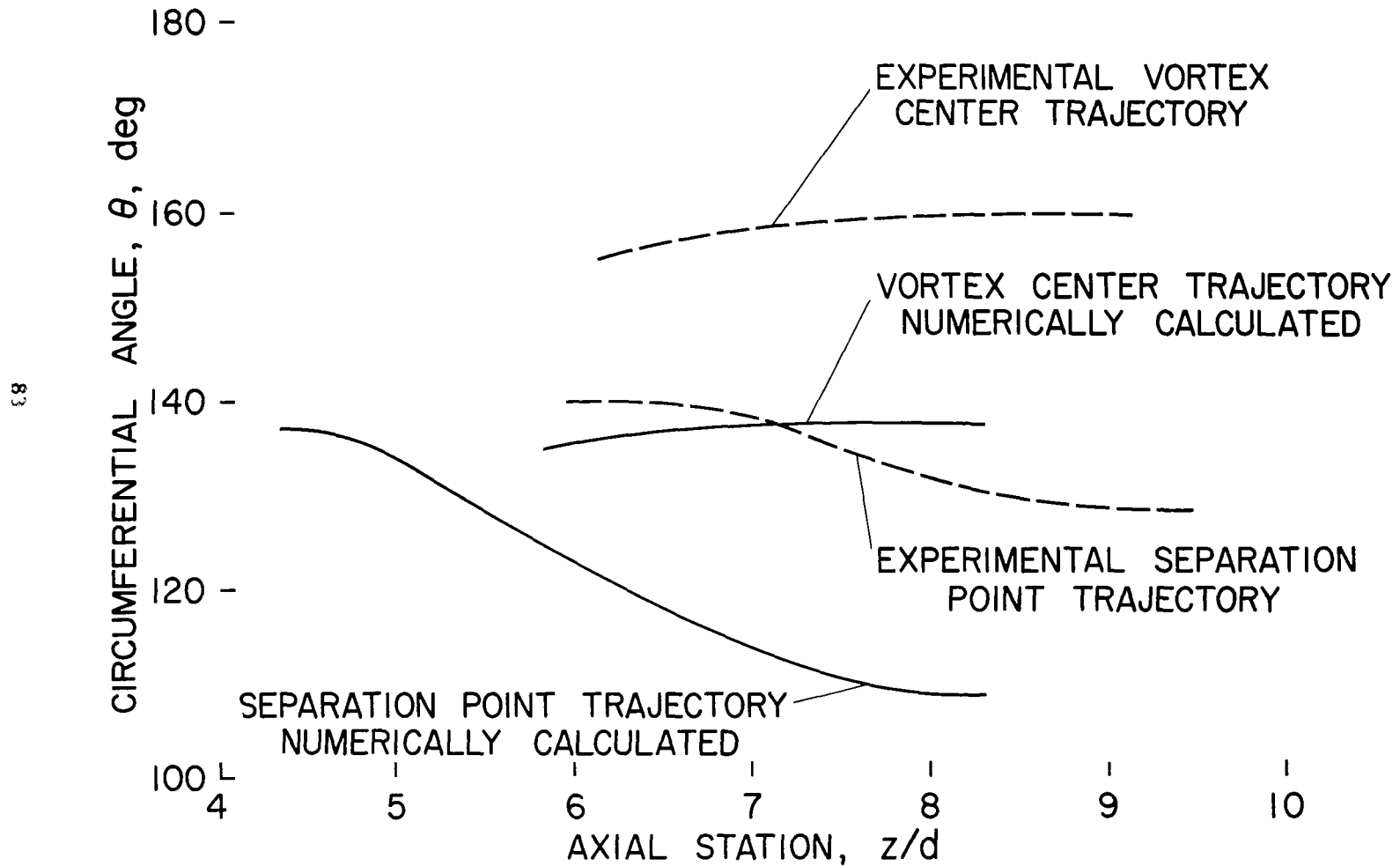


FIGURE 19



COMPARISON OF NUMERICAL AND EXPERIMENTAL LIFT  
AND DRAG COEFFICIENT DISTRIBUTIONS  
OGIVE-CYLINDER BODY

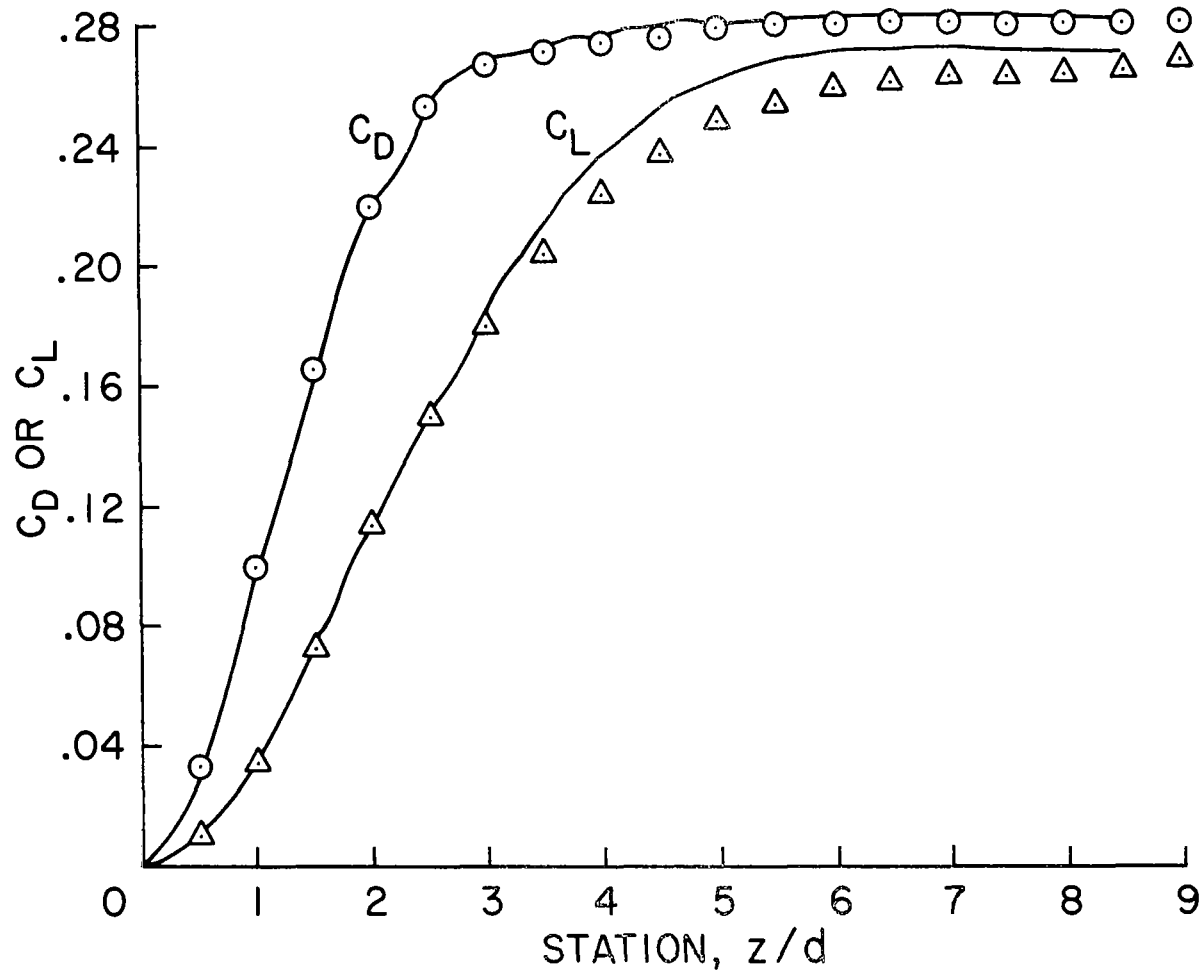


FIGURE 20

# VELOCITY VECTOR PLOT AT STA 1.135

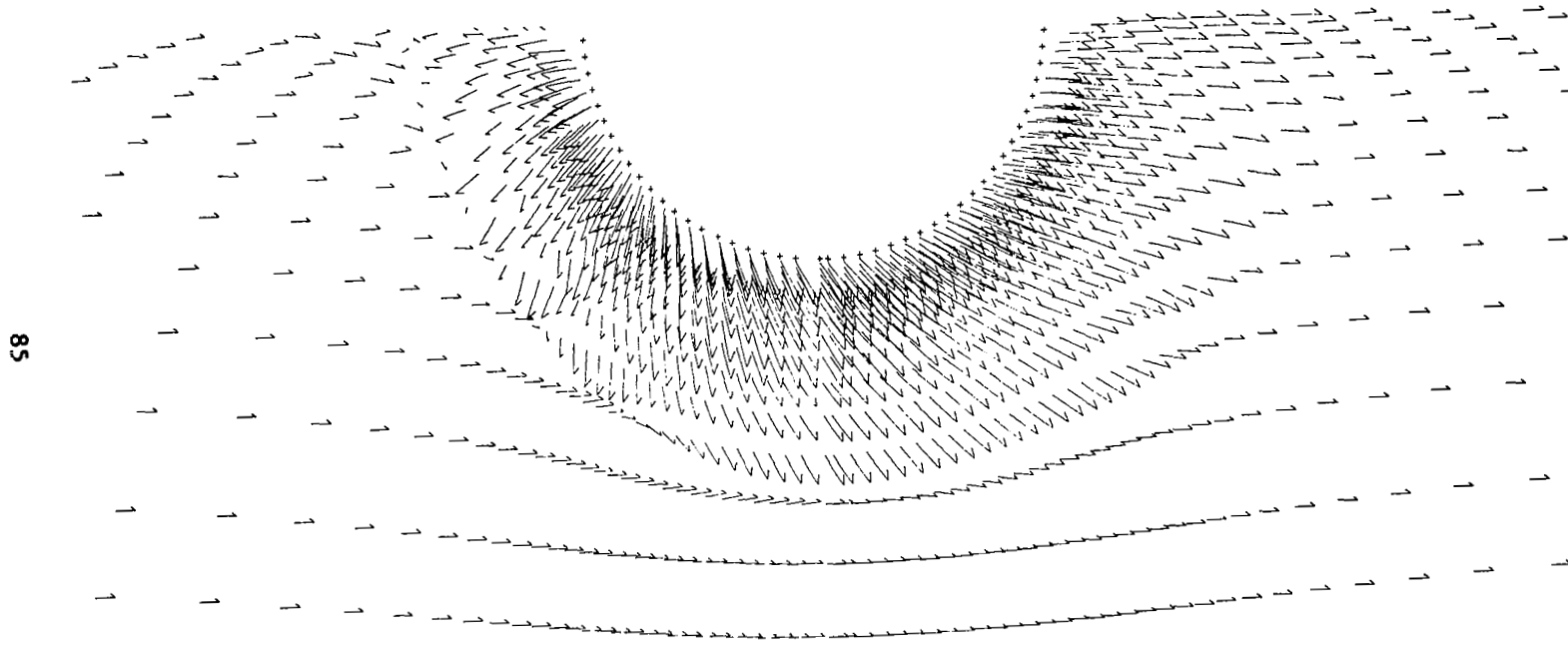


FIGURE 21

# VELOCITY VECTOR PLOT AT STA 10.0

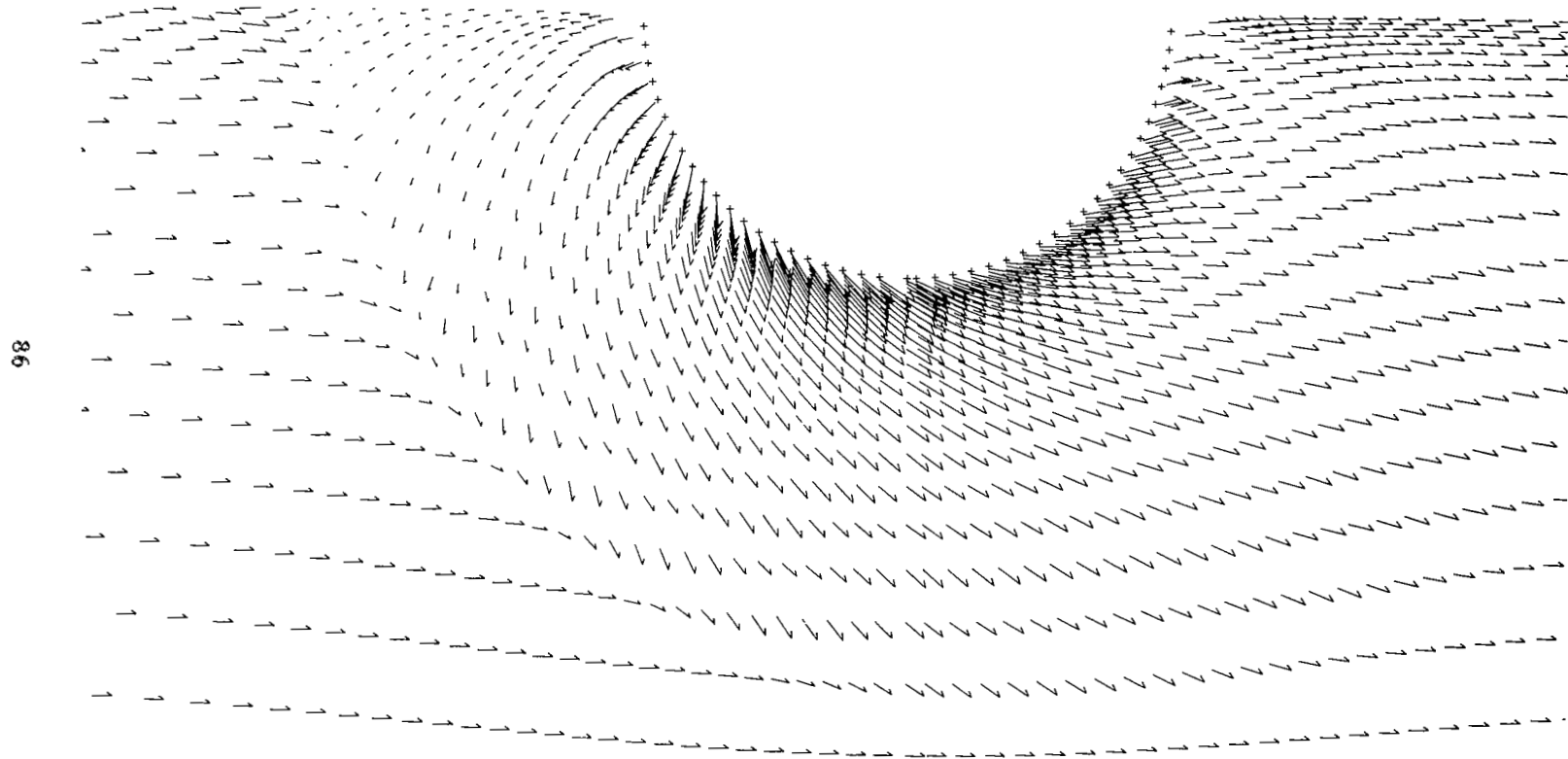


FIGURE 22

# VELOCITY VECTOR PLOT AT STA 12.0

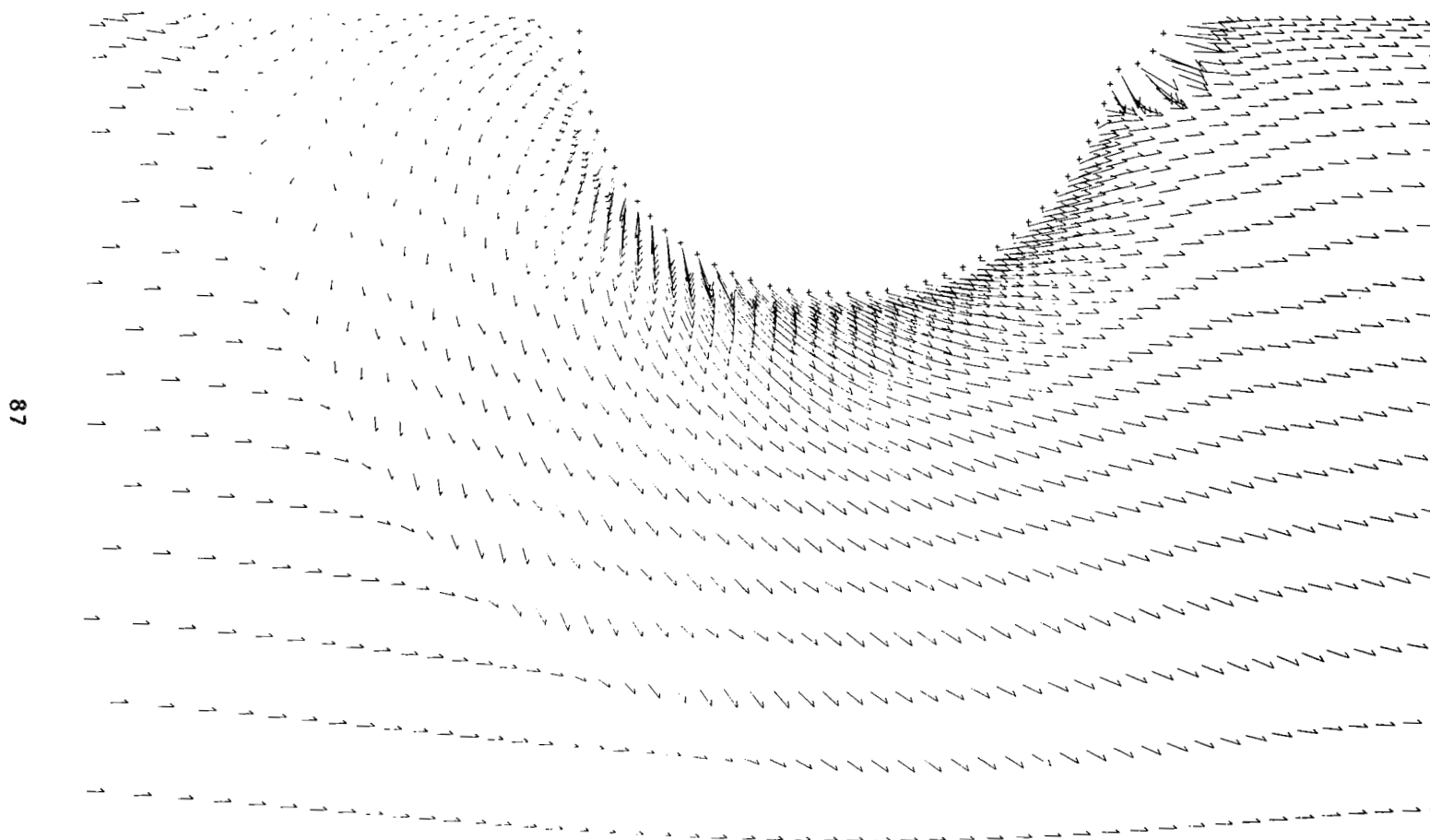


FIGURE 23

# VELOCITY VECTOR PLOT AT STA 17.0

88

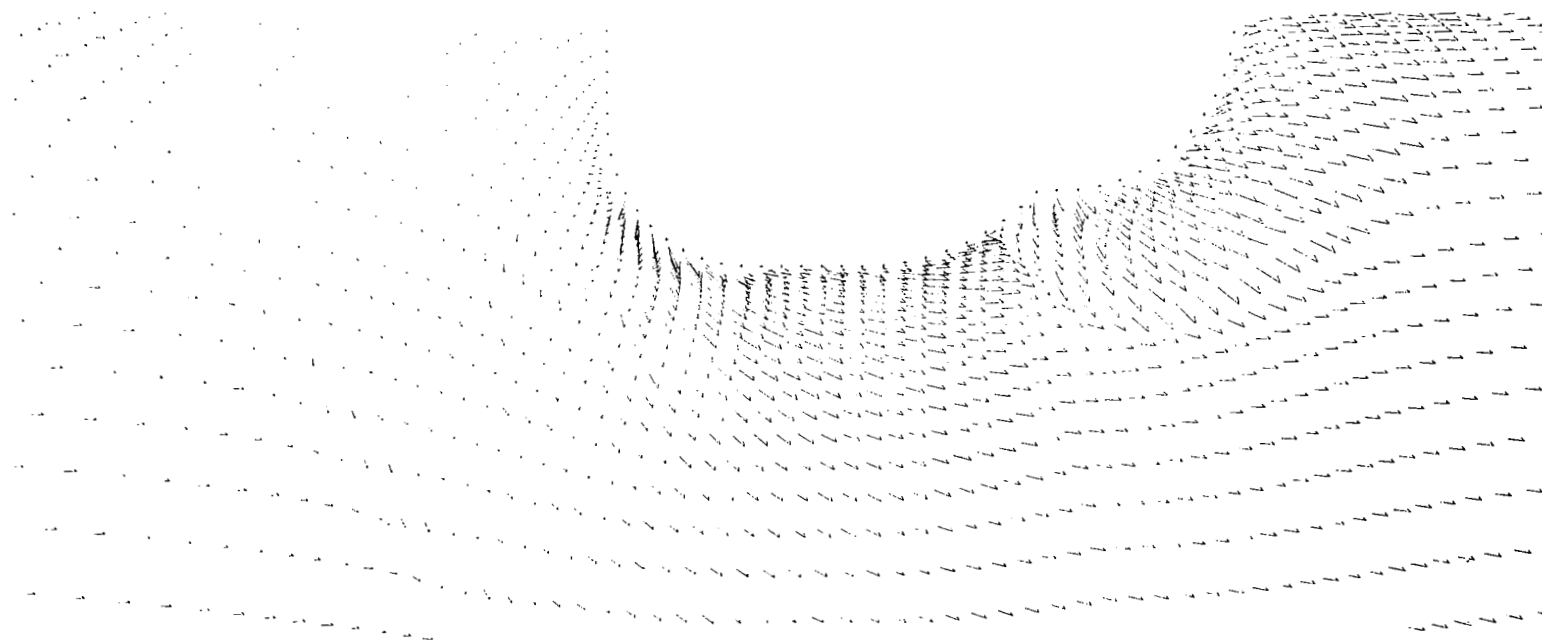


FIGURE 24



## VELOCITY VECTOR PLOT AT STA 19.6

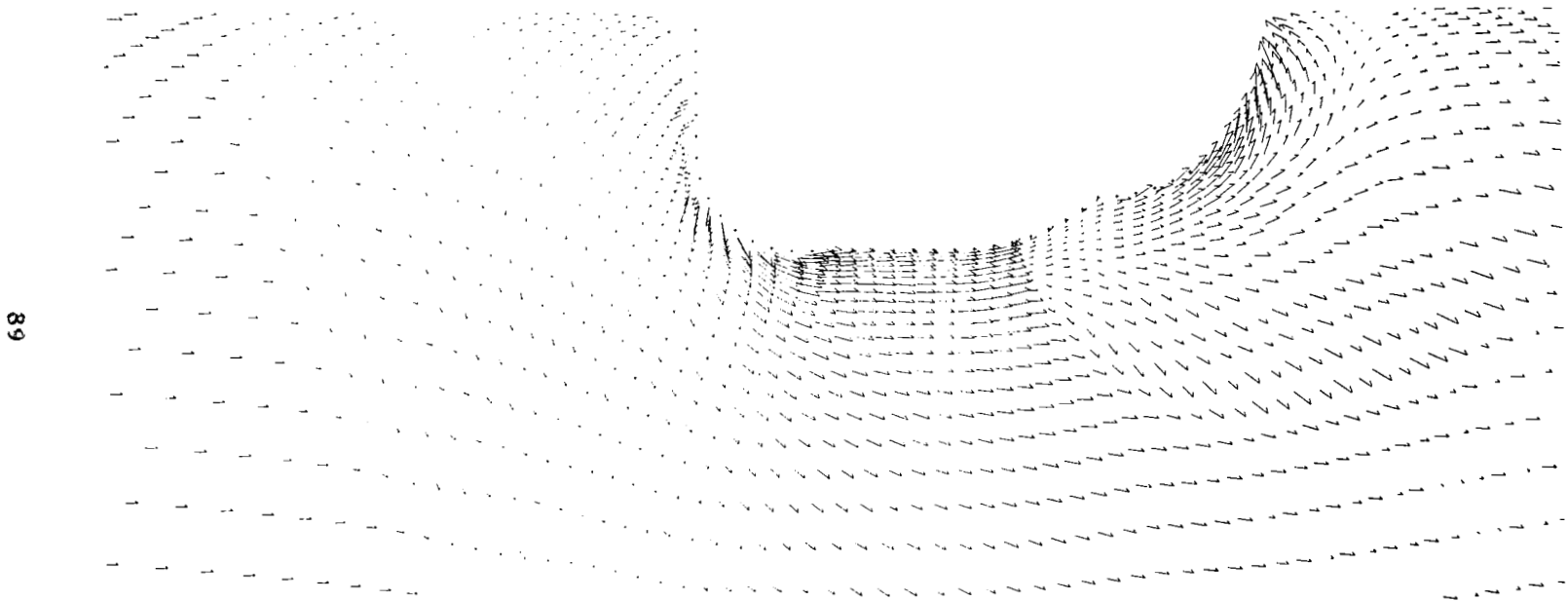


FIGURE 25

# STATIC PRESSURE INSTRUMENTATION ON FUSELAGE FOREBODY

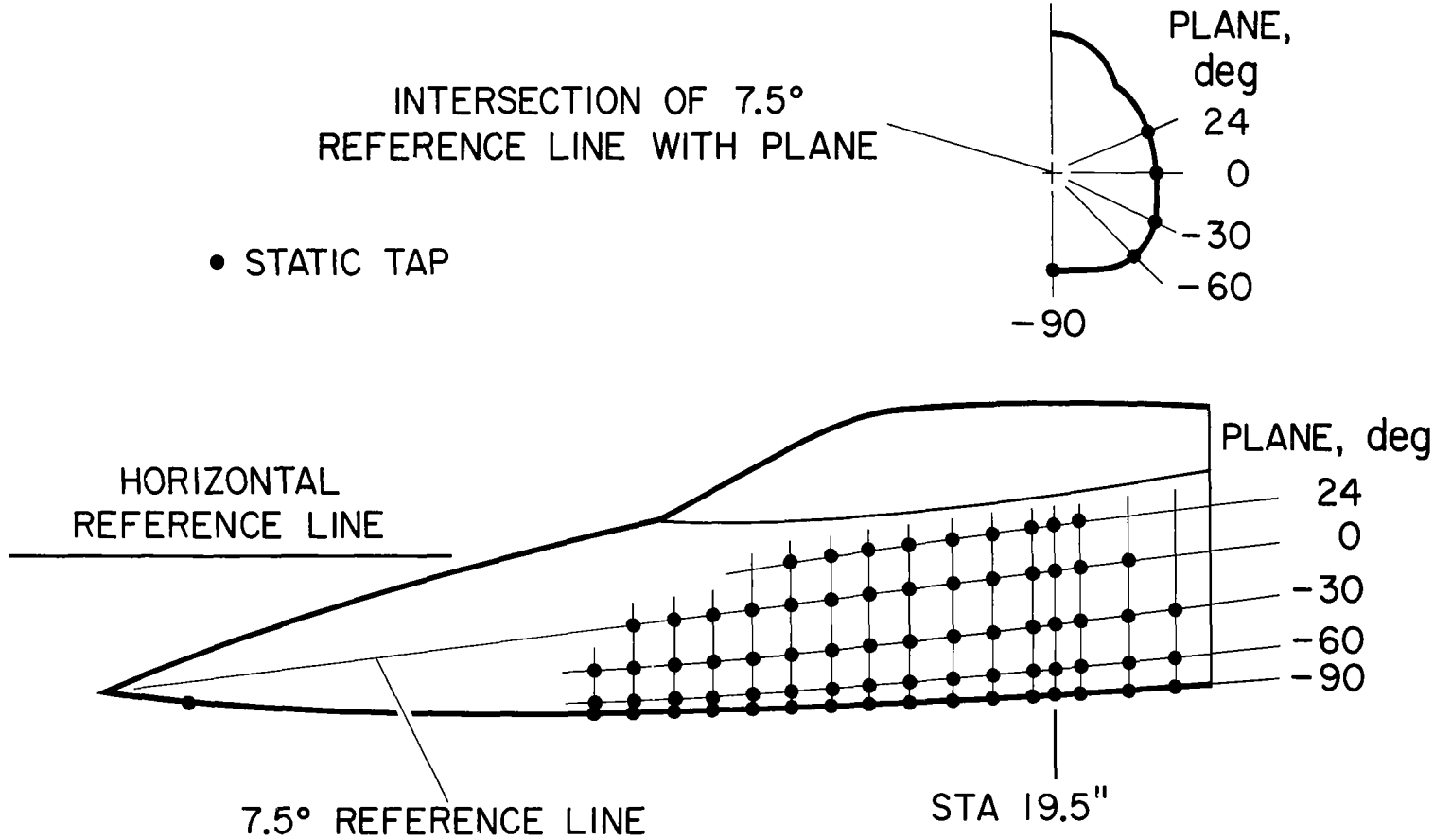


FIGURE 26

# COMPARISON OF NUMERICAL AND EXPERIMENTAL SURFACE PRESSURES

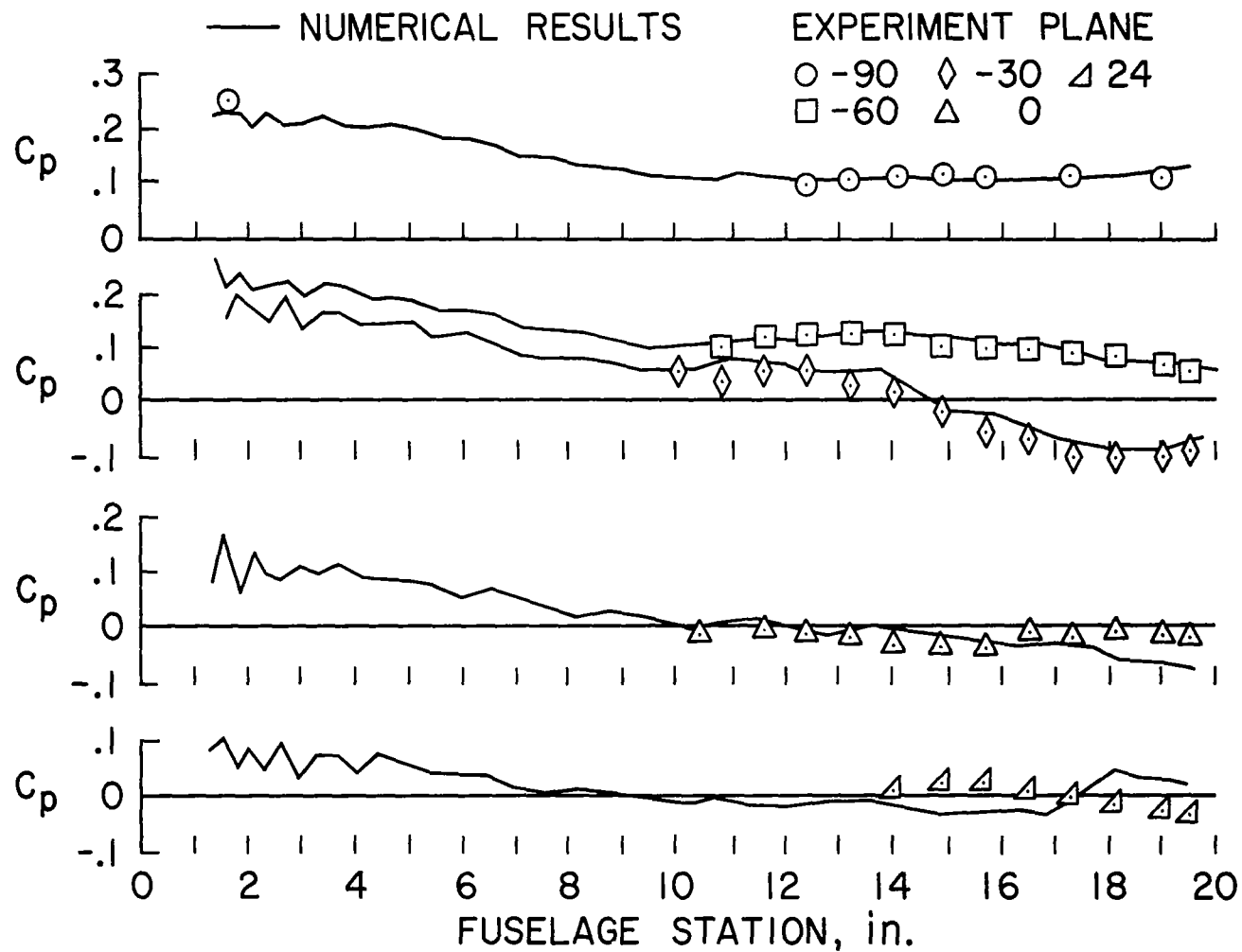


FIGURE 27



# COMPARISON OF NUMERICAL RESULTS WITH EXPERIMENT CONTOURS OF LOCAL PITOT PRESSURE RATIO

$P_{Tp}/P_{T\infty}$  FUS STA 19.5

$M_\infty = 2.50$   
 $Re_\infty = 9.1 \times 10^6/ft$   
 $\alpha = 15^\circ$

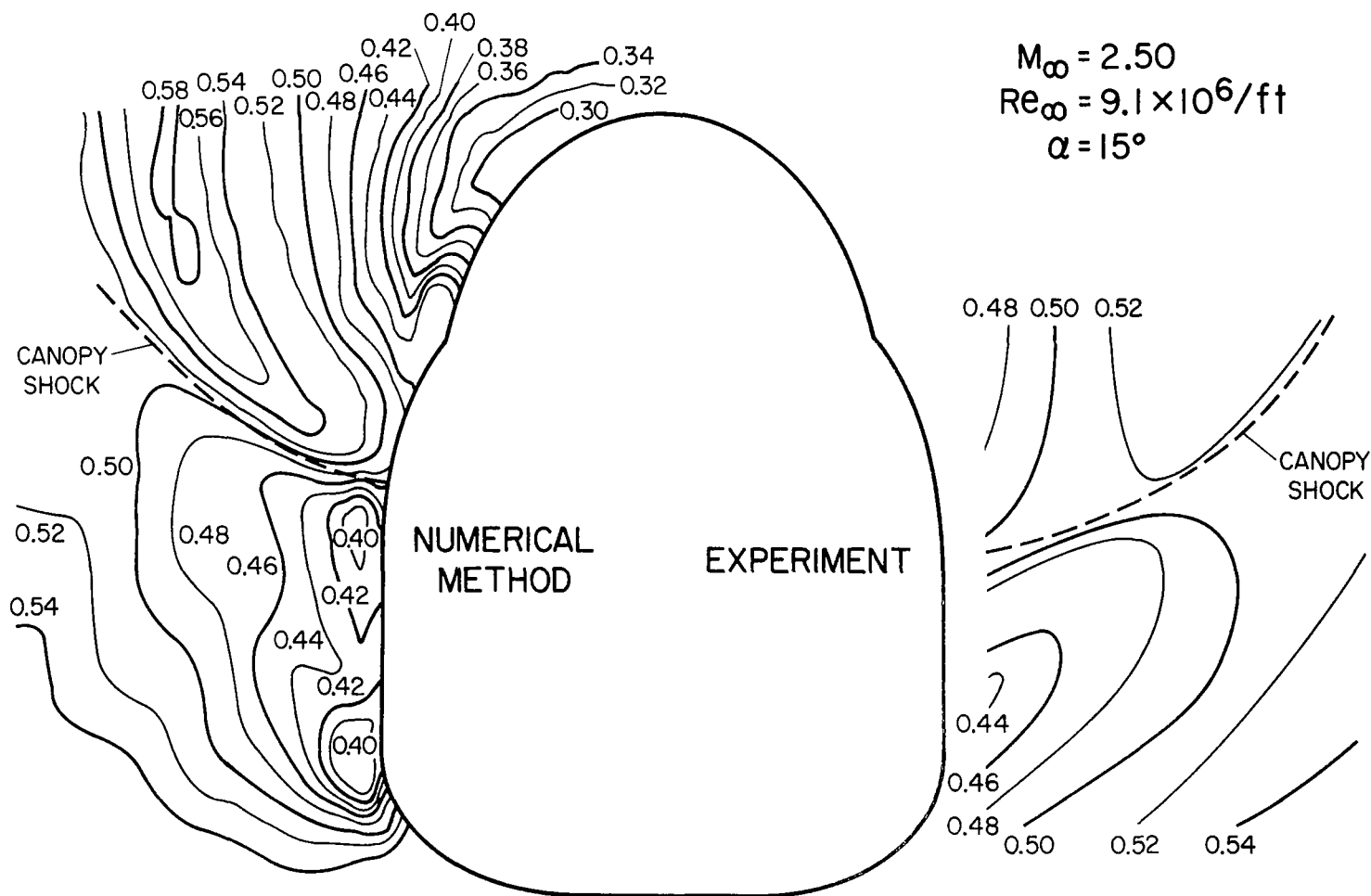


FIGURE 28

# COMPARISON OF NUMERICAL RESULTS WITH EXPERIMENT CONTOURS OF LOCAL SIDESLIP ANGLE, $\beta$ FUS STA 19.50

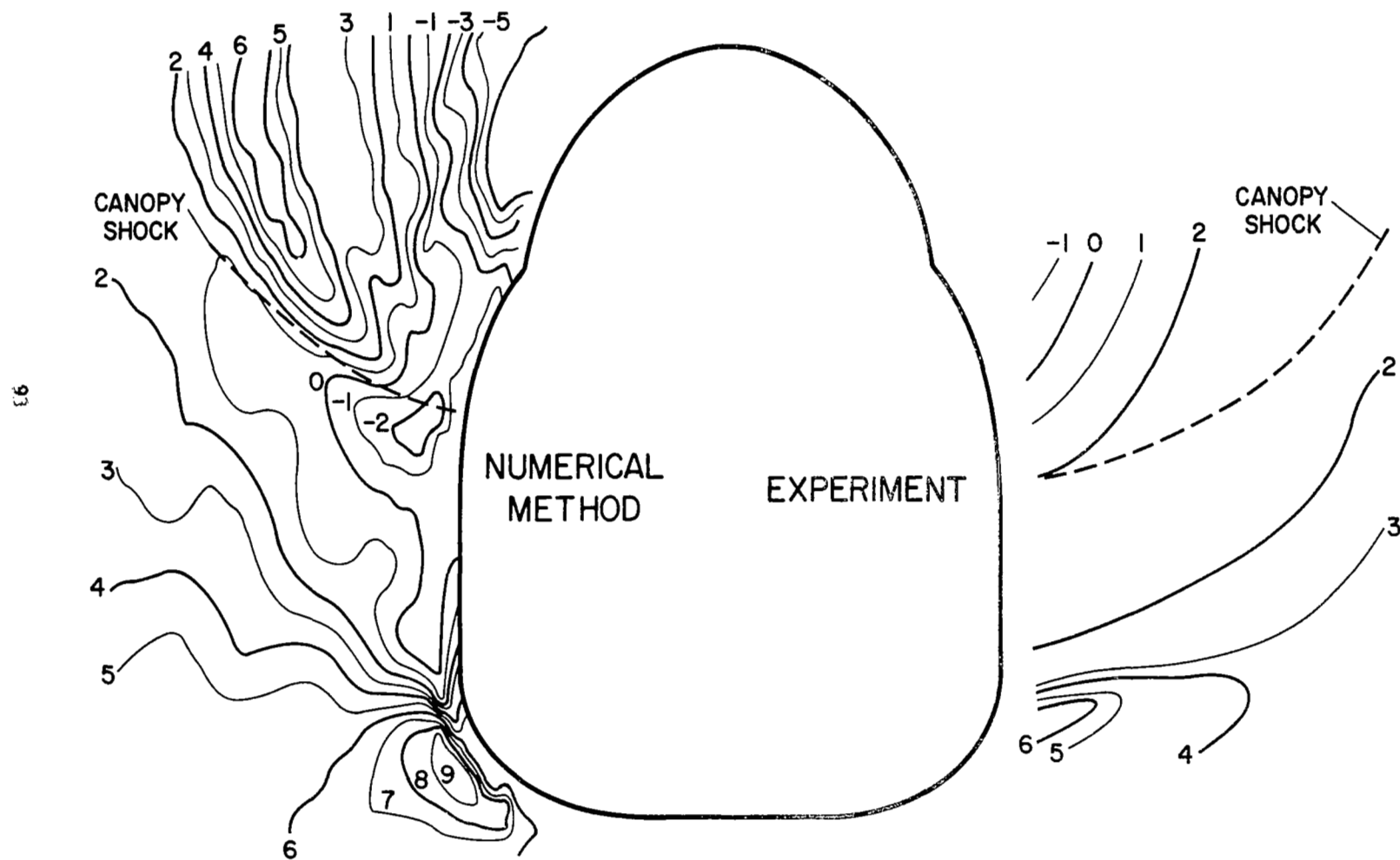


FIGURE 29

# COMPARISON OF NUMERICAL RESULTS WITH EXPERIMENT CONTOURS OF LOCAL MACH NUMBER, M FUS STA 19.50

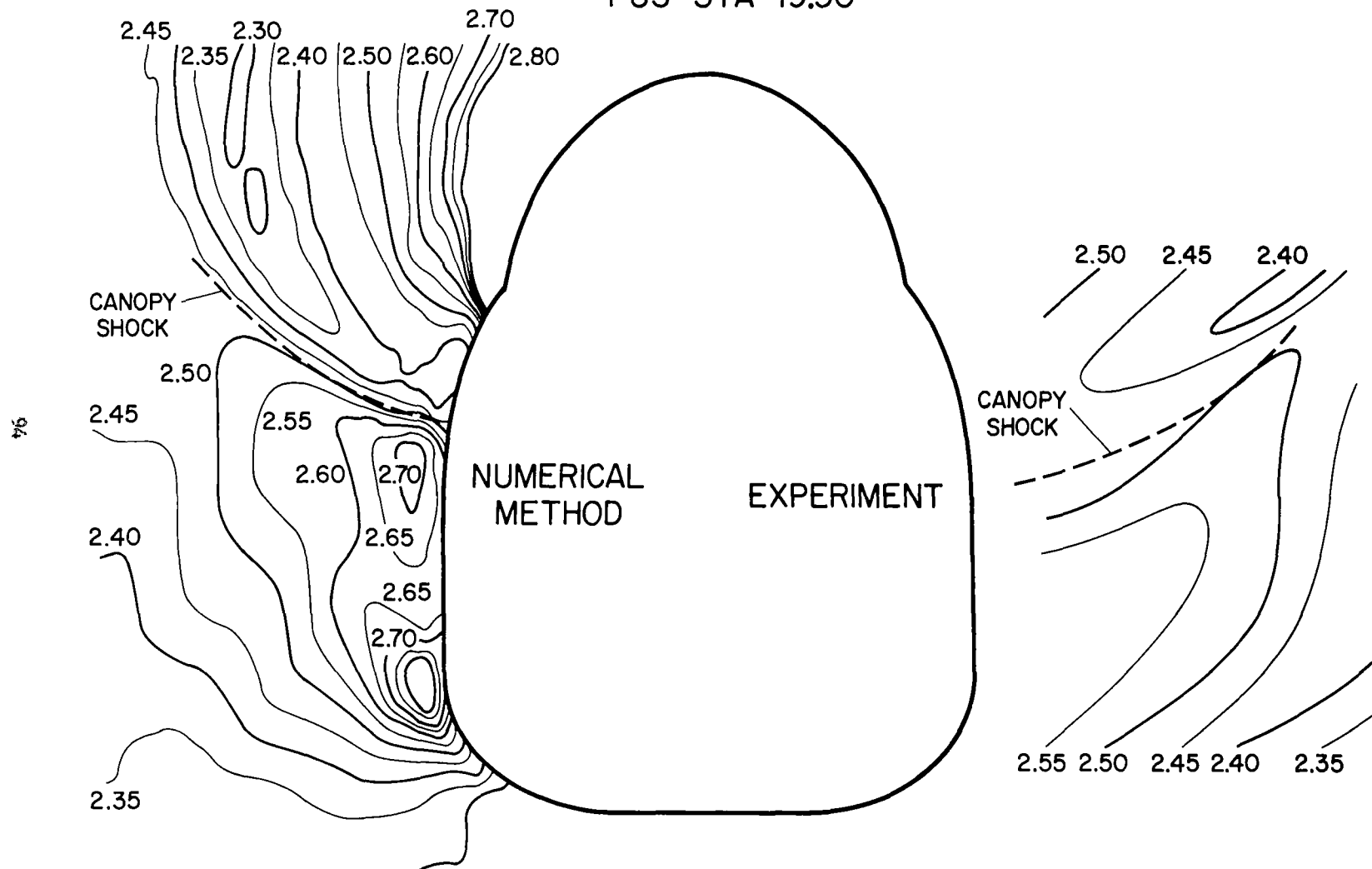


FIGURE 30

# COMPARISON OF NUMERICAL RESULTS WITH EXPERIMENT CONTOURS OF LOCAL ANGLE OF ATTACK, $\alpha_e$ FUS STA 19.50

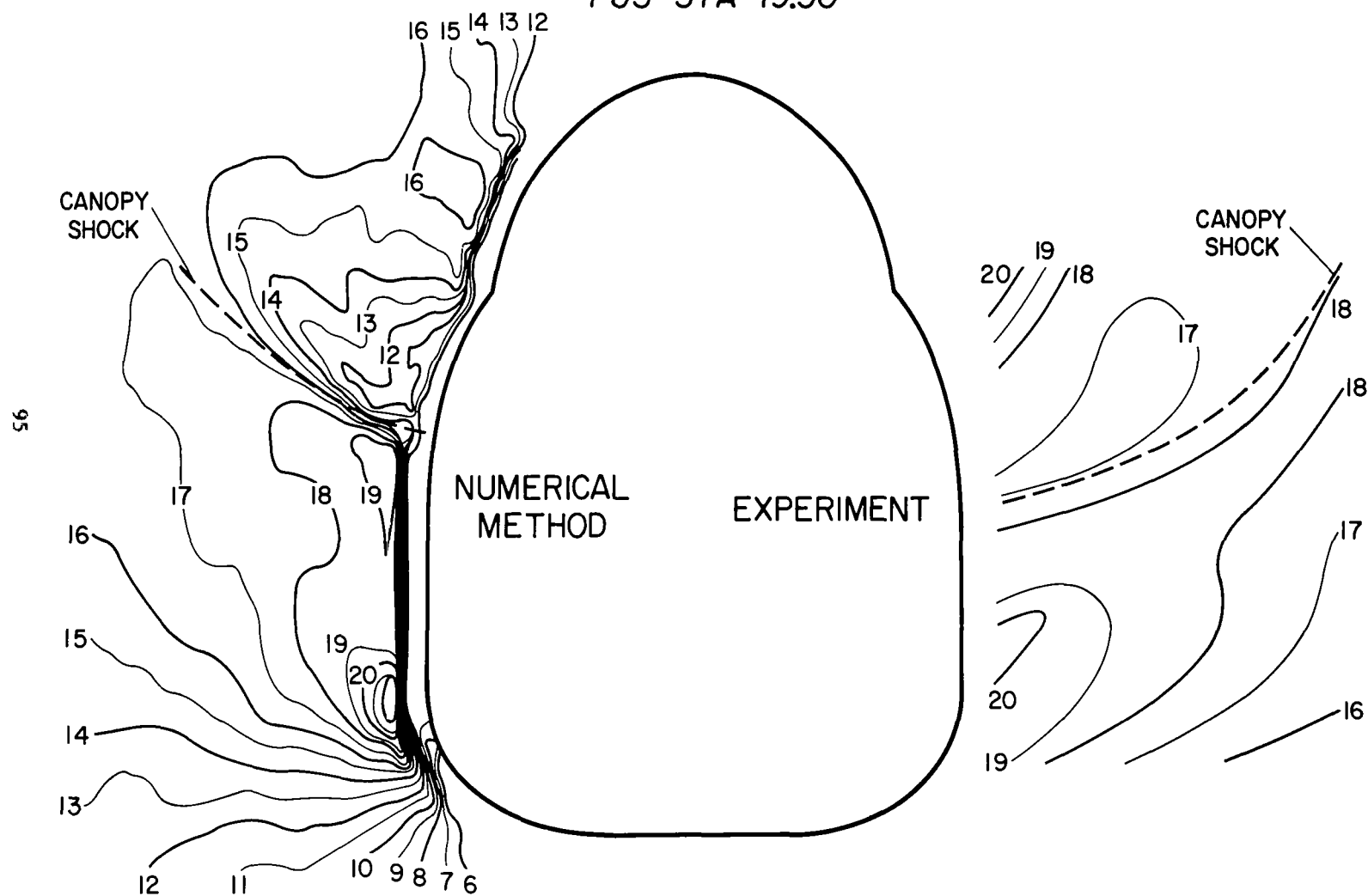


FIGURE 31

CONTOURS OF LOCAL TOTAL PRESSURE RATIO,  $p_s/p_{s\infty}$   
FUS STA 19.50

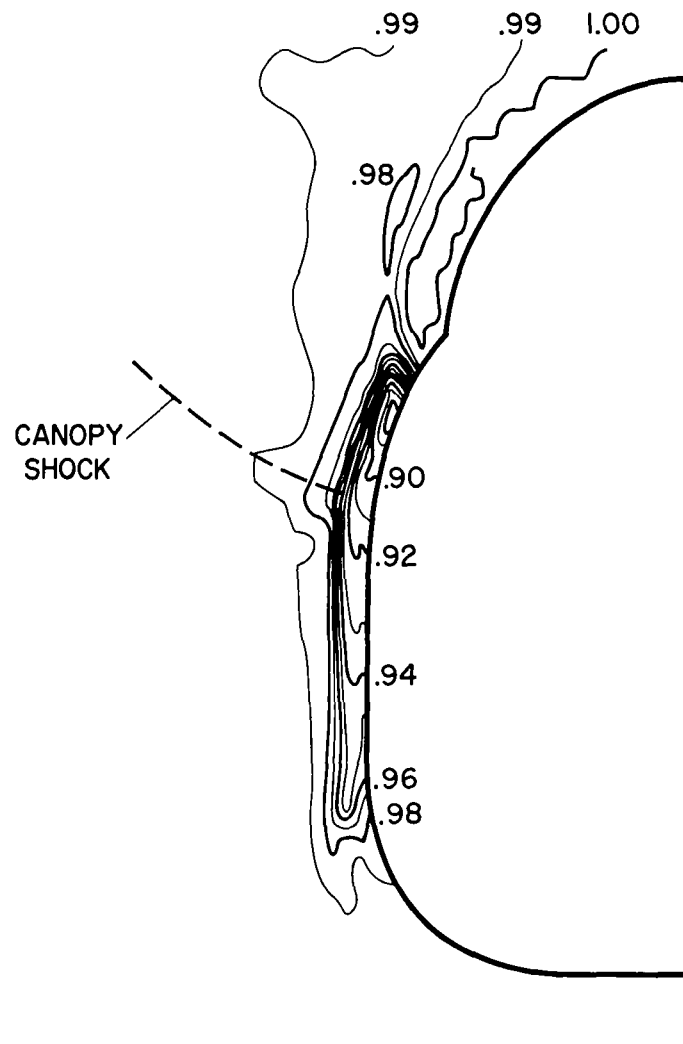


FIGURE 32

# LIFT AND DRAG COEFFICIENT DISTRIBUTIONS FUSELAGE CONFIGURATION

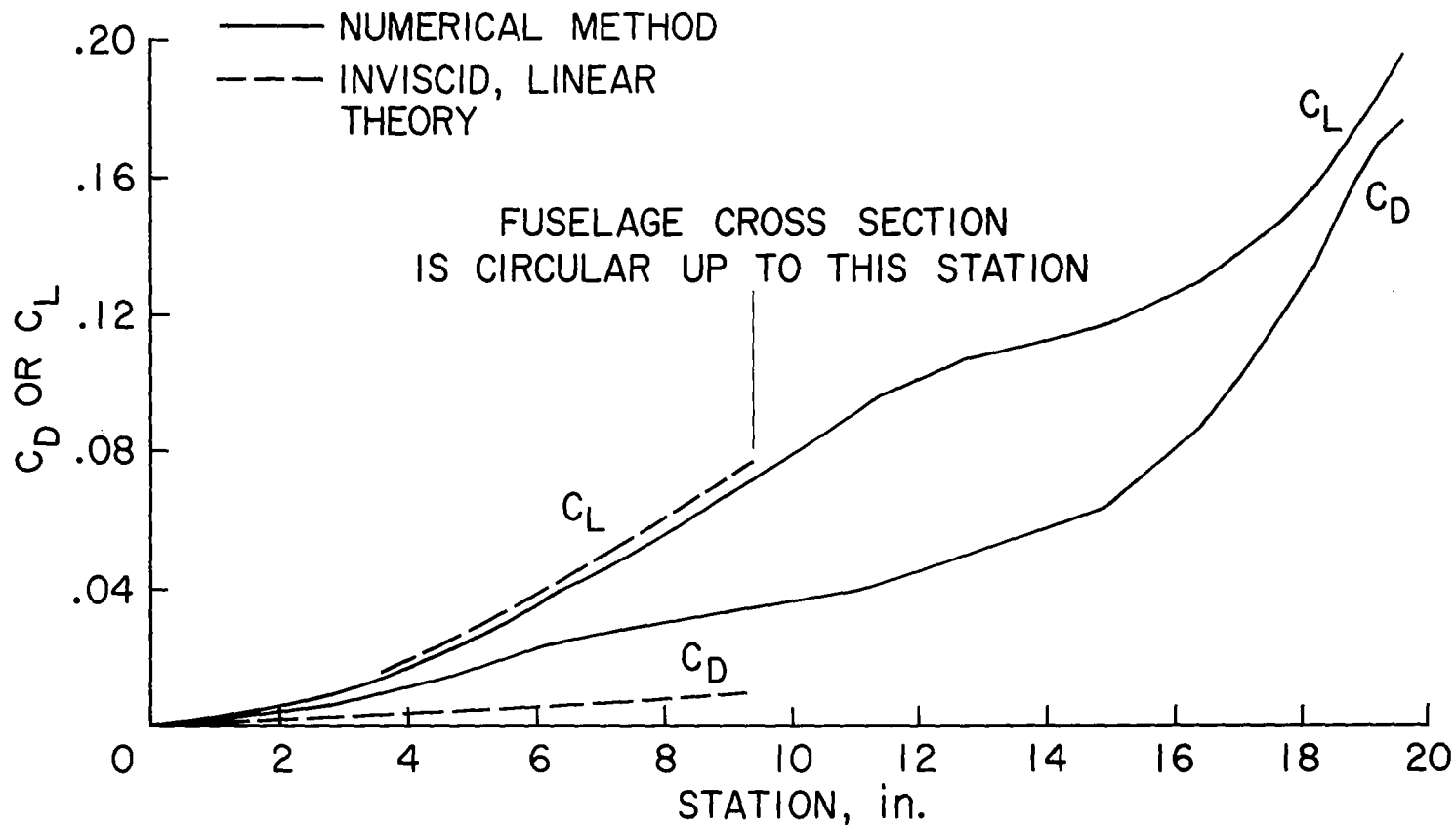


FIGURE 33